

# **EFFECT OF MILLING AND MICROWAVE SINTERING ON DENSIFICATION BEHAVIOR AND MICROSTRUCTURAL EVOLUTION OF TUNGSTEN HEAVY ALLOYS**

*A Thesis Submitted*

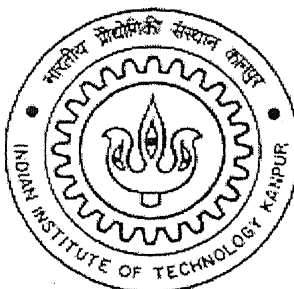
**In Partial Fulfilment of the Requirements**

**for the Degree of**

**Master of Technology**

by

**SANTOSH KUMAR TIWARI**



*to the*

**DEPARTMENT OF MATERIALS & METALLURGICAL ENGINEERING  
INDIAN INSTITUTE OF TECHNOLOGY KANPUR**

**NOVEMBER, 2004**

15 MAR 2005/MME

पुस्तकालय काशीनाथ कलकर पुस्तकालय  
भारतीय प्रौद्योगिकी संस्थान कानपुर  
वर्षादि No A.....150924.....

TH  
MME/2004/M  
T 543 e



# CERTIFICATE

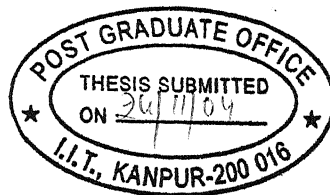
It is certified that the work contained in the thesis entitled *“Effect of Milling and Microwave Sintering on Densification Behavior and Microstructural Evolution of Tungsten Heavy Alloys,”* by Santosh Kumar Tiwari has been carried out under my supervision and that this work has not been submitted elsewhere for a degree.

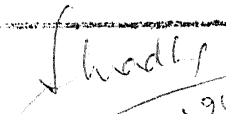
  
Dr. A. Upadhyaya

Department of Materials & Metallurgical Engineering

November, 2004

Indian Institute of Technology, Kanpur, India



  
24/11/04

## ABSTRACT

Powder metallurgy (P/M) has emerged as a promising solution to give tungsten and its alloys the desired shape and render them suitable for various engineering applications. In recent years, P/M processing of such alloys with improved sintered microstructure and properties has received special attention. The present study investigates the effect of milling and microwave sintering on the sintering behaviour and microstructural evolution of tungsten heavy alloys. Two different powder preparation routes, namely, mixing and milling were chosen to examine the effect of initial powder condition on the sintering response of the tungsten based heavy alloy. The compositions selected were 90W-7Ni-3Fe and 92.5W-6.4Ni-1.1Fe. The compacts were sintered at 1400°C and 1500°C corresponding to solid state and liquid phase sintering, respectively. The compacts were consolidated through conventional as well as microwave heating. Quantitative metallographic measurements were performed on all samples and the results were compared. It was observed that the samples consolidated with the milled powders had finer and homogenized microstructure as compared to those prepared by mixing route. Extensive microstructural evaluation reveals finer grain size, higher connectivity, contiguity and dihedral angle in microwave sintered alloy. As a result of less microstructural coarsening, microwave sintered compact has 20 % higher bulkhardness as compared to conventionally sintered counterpart. The W-Ni-Fe alloy coupled with microwave and could be successfully heated to liquid phase sintering temperature (1500°C) in approximately 50 % less time as compared to conventional sintering process.



# Table of Contents

	Page
List of Figures.....	v
List of Tables.....	ix
Acknowledgements .....	x
 <b>Chapter 1. INTRODUCTION .....</b>	 <b>1</b>
 <b>Chapter 2. BACKGROUND .....</b>	 <b>5</b>
2.1. Tungsten: Historical Overview .....	5
2.2. Tungsten Heavy Alloys (WHAs): An Introduction .....	6
2.3. Sintering .....	11
2.4. Liquid Phase Sintering: An Overview .....	12
2.4.1. Particle Rearrangement .....	14
2.4.2. Solution-Reprecipitation .....	18
2.4.3. Microstructural Coarsening and Coalescence .....	19
2.5. Processing of W-Ni-Fe Heavy Alloys .....	21
2.5.1. Conventional Sintering of WHAs .....	21
2.5.2. Microwave Sintering .....	23
2.5.2.1. Basics of Microwave Interaction with Materials .....	25
2.5.2.2. Advantages of Microwave Heating .....	34
2.5.3. Alloying Additions and Its Effect on WHAs .....	40
2.5.4. Heat Treatment Effects on WHAs .....	41
 <b>Chapter 3. EXPERIMENTAL PROCEDURE .....</b>	 <b>42</b>
3.1. Powder characterization .....	42
3.1.1. Particle Size and Distribution .....	42
3.1.2. Particle Morphology .....	44
3.1.3. Apparent Density and Flow Rate .....	44

3.2. Powder Preparation .....	46
3.2.1. Powder Mixing .....	46
3.2.2. Ball Milling .....	47
3.2.3. Attritor Milling .....	48
3.3. Compaction .....	48
3.4. Sintering .....	50
3.4.1. Debinding/Pre-sintering .....	50
3.4.2. Conventional Sintering .....	50
3.4.3. Microwave Sintering .....	52
3.5. Densification Behavior (S. D. and D. P.) .....	57
3.6. Quantitative Metallography .....	57
3.6.1. Sample Preparation .....	57
3.6.2. Microstructural Studies .....	58
3.6.2.1. Volume Fraction of Matrix .....	58
3.6.2.2. Contiguity ( $C_g$ ) and Connectivity ( $C_c$ ) .....	59
3.6.2.3. Dihedral Angle, ( $\phi$ ) .....	59
3.6.2.4. Surface Area per unit Volume ( $S_v$ ) .....	60
3.6.2.5. Mean Grain Size .....	60
3.7. X-Ray Diffraction Analysis .....	63
3.8. Elemental analysis by EPMA .....	63
3.9. Mechanical Properties .....	63
3.9.1. Bulkhardness .....	64
3.9.2. Microhardness .....	64
3.9.3. Compression Test .....	64
<b>Chapter 4. RESULTS AND DISCUSSIONS .....</b>	<b>65</b>
4.1. Particle Size and Size Distribution .....	65
4.2. Effect of Milling on Green Density .....	72
4.3. Density and Densification Parameter .....	72
4.4. Microstructural Evolution .....	77
4.5. Quantitative Metallographic Studies .....	80

4.5.1. Volume Fraction of Matrix .....	80
4.5.2. Contiguity and Connectivity .....	80
4.5.3. Dihedral Angle .....	83
4.5.4. Grain Size .....	85
4.6. Electron Micro-Probe Analysis (EPMA) .....	85
4.7. Mechanical Properties .....	95
4.7.1. Bulkhardness .....	95
4.7.2. Microhardness .....	95
4.7.3. Compression Test Studies at Room Temperature .....	98
4.8. Microwave Sintering .....	102
4.8.1 Heating Profile .....	102
4.8.2 Sintered Density and Densification Parameter .....	102
4.8.3 Stereological Quantification .....	106
4.8.4 Phase Analysis by XRD .....	114
4.8.5 Electron Probe Micro Analysis (EPMA) .....	114
4.8.6 Bulkhardness .....	117
4.8.7 Microhardness .....	117
 <b>Chapter 5. CONCLUSIONS .....</b>	 <b>119</b>
 <b>REFERENCES .....</b>	 <b>121</b>
 <b>Appendix I .....</b>	 <b>128</b>
 <b>Appendix II.....</b>	 <b>131</b>

## List of Figures

Figure	Page
1.1. A typical liquid phase sintered tungsten heavy alloy.	2
2.1. Typical microstructures of (a) solid state sintered (b) liquid phase sintered tungsten heavy alloy. The shown microstructure is of 90W-7Ni-3Fe sintered at 1400°C, 1h and 1500°C, 1h, respectively.	7
2.2. Fe-Ni Equilibrium phase diagram.	9
2.3. Ternary phase diagram of W-Ni-Fe alloys.	10
2.4. Different sintering pathways in terms of the key processing variables.	13
2.5. An ideal binary phase diagram for liquid phase sintering illustrating the solubility variables for additive phase (A) and base metal (B).	15
2.6. Diagram showing the effect of the liquid content on densification.	16
2.7. Schematic Diagram showing the stages in liquid phase sintering.	17
2.8. Conventional Process for fabrication of tungsten heavy alloys.	22
2.9. Comparison of conventional and microwave heating.	24
2.10. Illustration of (a) a low-loss sample: 1, incident radiation; 2 and 3, radiation returned to the sample after reflection from resonator walls and (b) a high-loss sample: 1, incident radiation; 2, radiation reflected from the sample; 3, radiation returned to the sample after reflection from resonator walls.	31
3.1. SEM micrograph of the as-received tungsten powder.	45
3.2. SEM micrograph the as-received of nickel powder.	45
3.3. SEM micrograph of the as-received iron powder	45
3.4. Ball mill used for the present study.	49
3.5. Attritor mill used for the present study.	49
3.6. MoSi <sub>2</sub> heated horizontal tubular furnace with Schematic diagram.	
3.7. Sintering cycles followed for solid-state and liquid phase sintering.	53

3.8.	Microwave furnace with schematic diagram.	55
3.9.	Sintering cycles followed for microwave sintering of WHA. The compacts were sintered at 1500°C for 20 min.	56
3.10.	Superimposing grid on a micrograph for calculation of volume fraction of a particular phase of interest.	61
3.11.	Contiguity measurement by superimposing parallel grid of lines on a micrograph.	61
3.12.	Connectivity and dihedral angle Measurement.	62
4.1a.	XRD patterns of fine tungsten powder.	68
4.1b.	XRD patterns of coarse tungsten powder.	68
4.2.	Scanning electron micrograph of (a) ball milled and (b) attritor milled tungsten powder.	70
4.3.	Micrographs of 90W (coarse)-7Ni-3Fe alloy in (a) mixed (b) ball milled and (c) attritor milled condition.	71
4.4.	Effect of milling on green density of 90W-7Ni-3Fe alloy.	73
4.5.	Comparison of percentage sintered density of solid state sintered mixed and milled powders.	74
4.6.	Comparison of densification parameter of solid state sintered mixed and milled powders.	74
4.7.	Comparison of sintered density of liquid phase sintered mixed and milled powders.	76
4.8.	Comparison of densification parameter of liquid phase sintered mixed and milled powders.	76
4.9.	Microstructures of solid state sintered 90W-7Ni-3Fe alloy prepared by (a) mixed (b) ball milled and (c) attritor milled powders.	78
4.10.	Microstructures of liquid phase sintered 90W-7Ni-3Fe alloy prepared by (a) mixed (b) ball milled and (c) attritor milled powders.	79

4.11. Effect of particle size and milling on volume fraction of matrix.	81
4.12. Effect of particle size and milling on contiguity.	82
4.13. Effect of particle size and milling on connectivity.	82
4.14. Effect of particle size and milling on dihedral angle.	84
4.15. Two-particle configuration in equilibrium state.	84
4.16. Effect of powder size and milling on the average tungsten spheroid size.	86
4.17. X-ray mapping showing the elemental distributions of solid state sintered 90W-7Ni-3Fe alloy consolidated with mixed powders.	89
4.18. X-ray mapping showing the elemental distributions of solid state sintered 90W-7Ni-3Fe alloy consolidated with ball milled powders.	90
4.19. X-ray mapping showing the elemental distributions of solid state sintered 90W-7Ni-3Fe alloy consolidated with attritor milled powders.	91
4.20. X-ray mapping showing the elemental distributions of liquid phase sintered 90W-7Ni-3Fe alloy consolidated with mixed powders.	92
4.21. X-ray mapping showing the elemental distributions of liquid phase sintered 90W-7Ni-3Fe alloy consolidated with ball milled powders.	93
4.22. X-ray mapping showing the elemental distributions of liquid phase sintered 90W-7Ni-3Fe alloy consolidated with attritor milled powders.	94
4.23. Effect of milling and particle size on bulk hardness of solid state sintered 90W-7Ni-3Fe alloy.	96
4.24. Effect of milling and particle size on bulk hardness of liquid phase sintered 90W-7Ni-3Fe alloy.	96
4.25. Effect of milling and particle size on microhardness of matrix phase of liquid phase sintered 90W-7Ni-3Fe alloy.	97
4.26. SEM micrographs of 90W-7Ni-3Fe alloy (a) as solid state sintered (b) as liquid phase sintered (c) solid state sintered sample compressed at 200 kN and (d) liquid phase sintered sample compressed at 200 kN.	99
4.27. SEM micrographs of 90W-7Ni-3Fe alloy (a) as solid state sintered (b) as liquid phase sintered (c) solid state sintered sample compressed at 200 kN and (d) liquid phase sintered sample compressed at 200 kN.	101

4.28. Comparison of heating profile and power consumption of microwave and conventionally sintered 92.5W-6.4Ni-1.1Fe alloy.	103
4.29. Scanning electron micrographs (a) microwave (b) conventionally sintered 92.5W-6.4Ni-1.1Fe alloy. The alloys were sintered at 1500°C.	105
4.30. Comparison of stereological parameters (a) tungsten content (vol. %) (b) connectivity (c) contiguity and (d) $S_v$ of 92.5W-6.4Ni-1.1Fe alloy sintered through conventional as well as microwave heating.	109
4.31. Grain size distribution curve of 92.5W-6.4Ni-1.1Fe alloy sintered through conventional as well as microwave heating.	110
4.32. Comparison of dihedral angle distribution of 92.5W-6.4Ni-1.1Fe alloy sintered through conventional as well as microwave heating.	111
4.33. German's model showing the relationship between contiguity and solid volume fraction keeping dihedral angle constant.	113
4.34. Gurland's model showing the relationship between dihedral angle and contiguity keeping continuity constant.	113
4.35. XRD analysis of microwave and conventionally sintered 92.5W-6.4Ni-1.1Fe alloy.	115
4.36a. Microstructure of microwave sintered 92.5W-6.4Ni-1.1Fe alloy with X-Ray mapping of the elements present in the matrix.	116
4.36b. Microstructure of conventionally sintered 92.5W-6.4Ni-1.1Fe alloy with and X-Ray mapping of the elements present in the matrix.	116
4.37. Hardness values of 92.5W-6.4Ni-1.1Fe alloy (a) bulk-hardness and (b) microhardness of grains as well as matrix phase.	118

## List of Tables

Table	page
3.1. Experimental Details.	43
3.2. Powder characteristics of as-received elemental powders.	43
4.1. Particle size analysis of mixed, ball milled and attritor milled powders.	67
4.2. Element contents in matrix phase of solid state sintered samples.	87
4.3. Element contents in tungsten grain of solid state sintered samples.	87
4.4. Element contents in matrix phase of liquid phase sintered samples.	88
4.5. Element contents in tungsten grain of liquid phase sintered samples.	88
4.6. Properties of 90W-7Ni-3Fe alloy in as sintered condition.	100
4.7. Properties of 90W-7Ni-3Fe alloy after compression test.	100
4.8. Sintered densities of microwave and conventionally sintered 92.5W-6.4Ni- 1.1Fe alloy samples.	104
4.9. Comparison of stereological parameters of microwave and conventionally sintered 92.5W-6.4Ni-1.1Fe alloy samples.	107



## ACKNOWLEDGMENTS

I would like to express my deep sense of gratitude to my advisor Dr. A. Upadhyaya for his expert guidance, support and encouragement throughout the present research. His dynamic personality will be a source of inspiration throughout my career.

I extend my special thanks to Mr. Soni for his necessary help during my experimental work. I also wish to thank all the staff of MME department and ACMS, who helped me at many occasions.

I would like to take the opportunity to thank my all lab mates Pinaki, Kausik, Mayadhar, Amit, Jayant, Shashank, Ravikiran, Puneet, Mitun, Shubhranshu, Pranav, Ashish, Ravi, Balaji, Avni, Vaibhav and Ankur for their encouragement and welcome suggestions at every possible step.

I thank my friends Vijay, Pankaj, Aniruddha, Rohit, Asish, Ajit, Rajesh and Rajiv for their support and companionship who made my stay at IIT Kanpur very pleasant and memorable. I am grateful to my friends for their love and affection and I wish them all success in their life.

Last but not the least; I thank my parents, my sisters and sister-in-laws and brother for providing me their moral support, motivation and encouragement. I dedicate this thesis to them.

## Chapter 1

### INTRODUCTION

Tungsten heavy alloys (WHAs) are two phase composite systems having tungsten content ranges 80-95% (wt. %) and the balance is generally a mixture of relatively low melting transition elements, such as nickel, iron, copper and cobalt [1]. A typical liquid phase sintered microstructure of these alloys contains dispersed tungsten spheroids (b.c.c) in a ductile matrix phase (f.c.c.) as shown in Figure 1.1. Tungsten heavy alloys offer a unique combination of properties such as high strength (1000-1700 MPa), high ductility (10-30%), good corrosion resistance, and easy machinability [2]. These properties make these alloys a potential candidate for counter balance weights, vibration damping devices, microelectronic packaging, radiation shielding and other applications where high density is the key property. Because of their refractoriness and high temperature properties tungsten based heavy alloys have been projected as a viable replacement of depleted uranium (DU: U-0.75Ti) alloys for kinetic energy penetrators.

Because of its high fusion temperature (mp 3420°C), the conventional processing of these alloys by casting is not feasible. Hence, these alloys are processed by powder metallurgical (P/M) route. Liquid phase sintering (LPS) is the most commonly used mechanism for consolidation of these high density alloys [3]. However, during sintering, due to prolonged heating at high temperature, these alloys exhibit considerable microstructural coarsening in the final stage. It is envisaged that restricting the growth of W-grains will further enhance the properties of these alloys.

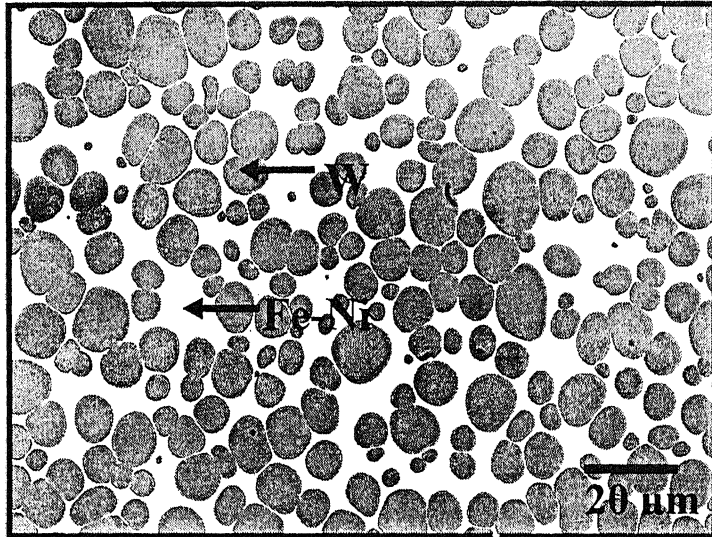


**Figure 1.1.** A typical liquid phase sintered tungsten heavy alloy.

To validate this hypothesis, the present investigation undertakes the comprehensive studies of the densification behavior and microstructural evolution of tungsten heavy alloys in solid state and liquid phase sintering conditions and its effect on mechanical properties of the alloy.

It is conceived that it can be achieved by selecting the smaller initial powder size. Alternatively, comminuting like milling can be utilized to achieve the required fineness of the powder. In past, the work has been focused on modifying the matrix composition and post sintering heat treatment to achieve full densification and optimal mechanical properties. Being a strategic material very little has been reported in the open literature on the effect of initial powder modifications by milling on the densification response. Milling of powders is an effective method for microstructural property improvement of sintered products. Churn and German [4] have reported that mechanical properties generally improve when tungsten spheroid size becomes finer and the W/W interface reduces. Due to refinement in tungsten spheroid size contiguity reduces and percentage of crack path through matrix increases, which results in ductile mode of fracture. Milling effects the sintering behavior and cause microstructural changes, which have a key role in governing properties of these alloys. In the present research, the effect of milling has been studied on the densification behavior and Microstructural evolution of heavy alloys.

Use of finer powder makes compaction more difficult. So, some other alternative must be explored which comes out to be the reduction of the sintering cycle time using faster heating rate. But in conventional furnaces due to difference in the temperatures of surface and core, faster heating rate may generate thermal shock. So using faster heating rate is not practically feasible. Recently, Roy *et al* [5] reported that metals can be processed by microwave heating provided they are in powder form. These microwaves directly

interact with the material and provide volumetric heating. This results in uniform and faster heating and thus gives more uniform phase distribution, finer grain size and improved stereological parameters [6].

This work provide a fundamental basis for understanding the effect of milling and microwave sintering on the densification behavior and microstructural evolution of tungsten heavy alloys. This thesis id divided into five chapters. Chapter 2 presents a comprehensive review of various processing aspects of tungsten heavy alloys (WHAs). This includes the recent advances in the field of tungsten heavy alloys. Chapter 3 describes in detail the experimental procedures applied in present work. In Chapter 4, results and discussion of all the experimental works are given in detail. It compiles all the findings of the present research. Chapter 5 summarizes the findings of the present work. At last the appendix is provided for reference.

## **Chapter 2**

### **BACKGROUND**

To understand the microstructure-mechanical properties correlation, it is essential to have a framework for understanding the phenomenology of liquid phase sintering and its effect on the microstructure and densification response of WHAs. The following section presents an overview of liquid phase sintering along with the effect of milling and microwave sintering on the densification behavior and microstructural evolution of tungsten heavy alloys. This chapter reviews the prior works on tungsten heavy alloys with special emphasis on using milled powders and also microwave sintering as an alternative route for consolidating the tungsten based heavy alloys.

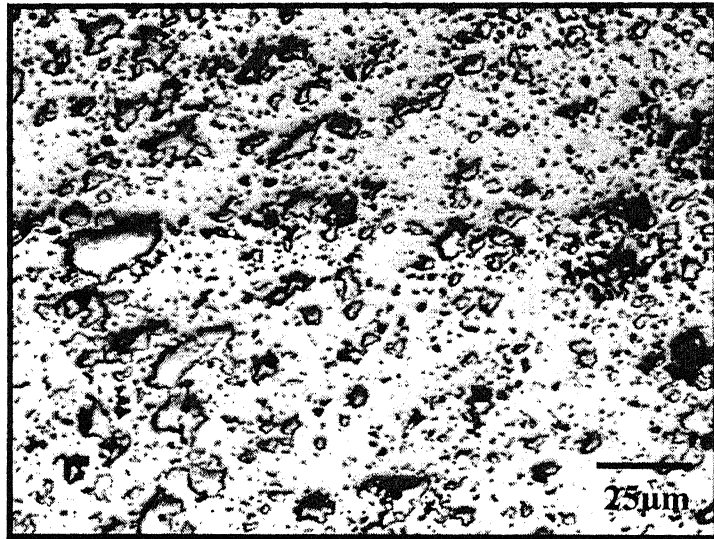
#### **2.1. Tungsten: Historical Overview**

Tungsten heavy alloys have been associated to powder metallurgy processing since 1930's although by the late 18<sup>th</sup> century tungsten was obtained by reducing Wolframite, a mineral oxide of tungsten. The origin of the name tungsten came from the Swedish name meaning "Heavy Stone" [7]. However, industrial application did not emerge until half a century later, when early interest in tungsten by powder metallurgy came about as the need for making incandescent lamps. Till that date, tungsten was used in the arts as pigments and as metal powders for manufacturing of ferrotungsten alloys. In 1910, Coolidge [8] successfully produced ductile tungsten filaments from sintered tungsten powder mechanically worked then drawn at room temperature. Similar work was done by Siemens and Halske [9] by mixing tungsten and nickel powders which were processed by liquid

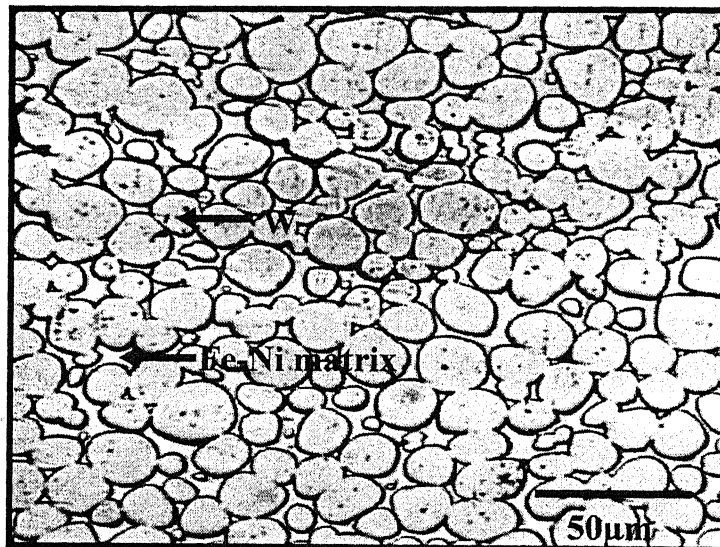
phase sintering. Subsequent work on tungsten was performed by Smithells, Pitkin and Avery [10] who investigated grain growth and its relation to powder particle size, compaction pressure and sintering temperature. Further discussion has been presented by Lenel *et al.* [11] on tungsten alloy systems including physical properties, microstructure and processing parameters and a detailed review on liquid phase sintering has been performed by German [12]. Since the early works, the heavy alloy systems have been found a wide range of both civilian and military applications like radiation shielding, counter balance weights, kinetic energy penetrators, vibration damping devices, microelectronic packaging and heavy duty electrical contacts.

## **2.2. Tungsten Heavy Alloys (WHAs): An Introduction**

Tungsten heavy alloys (WHAs) are two-phase composites, based on primarily W-Ni-Fe and W-Ni-Cu. Although tungsten based sintered heavy alloys with Cu-Ni binder were initially developed, attention was eventually diverted to Fe-Ni binder because of better-attained mechanical properties. Tungsten heavy alloys based on W-Ni-Fe are a class of composites characterized by high density. These are processed by sintering, namely solid state sintering and liquid phase sintering from elemental powder mixes where tungsten ranges from 80 to 98 weight percent. It is quite difficult to achieve full density through solid state sintering, so liquid phase sintering is commonly used to consolidate these alloys. The final liquid phase sintered alloy consists of nearly pure tungsten grains dispersed in a ductile matrix. The typical microstructures of solid state sintered and liquid phase sintered is shown in Figure 2.1. The mean tungsten grain size varies from 15-60  $\mu\text{m}$  depending on initial particle size, volume fraction of tungsten, sintering temperature and time. These alloys have the best combination of optimal mechanical properties and cost effectiveness



(a)



(b)

**Figure 2.1.** Typical microstructures of (a) solid state sintered (b) liquid phase sintered tungsten heavy alloy. The shown microstructure is of 90W-7Ni-3Fe sintered at 1400°C, 1h and 1500°C, 1h, respectively.



among all tungsten based heavy alloys. The combination of density ( $16-18 \text{ g/cm}^3$ ), ductility (10-30%), strength (1000-1800 MPa), conductivity, machinability and corrosion resistance makes WHA composites unique in the spectrum of materials [13].

Other tungsten based heavy alloys are W-Cu-Ni, W-Co- Ni, and W-Cr-Ni. W-Co-Ni alloys are costly due to higher cost of cobalt. Presence of  $\text{W}_6\text{Co}_7$  intermetallic phase in this system deteriorates the mechanical properties; very high amount of cobalt is required (about 20%) to achieve 20 % elongation. Upadhyaya and Srikanth [14] have reported that nickel binder proved to be better as compared to the binary Co-Ni binders as far as the mechanical properties were concerned. The W-Cr-Ni alloy exhibit higher ultimate tensile strength along with poor ductility values. The presence of brittle  $\sigma$  phase makes it suitable for only high hardness applications.

W-Ni-Fe alloy exhibit excellent combination of ductility and strength and can be cold worked to a reduction of 70% without intermediate annealing. Higher addition of iron causes a significant matrix strengthening effect and improves high temperature strength. As shown in Figure 2.2 [15], it is clear that nickel-iron having a ratio of 7:3 have a melting point about  $1445^\circ\text{C}$ . Figure 2.3 [16] shows the ternary phase diagram of W-Ni-Fe alloy. Chances of intermetallic phase formation can be avoided by fast cooling. In W-Ni-Fe heavy alloys matrix consists about 20-30% dissolved tungsten depending upon the process parameters. The equilibrium phase diagram shows that in this composition matrix will exist in  $\gamma$  (f.c.c.) form. For W-Ni-Fe system, it has been observed that at  $1435^\circ\text{C}$  a eutectic melt of Ni-Fe forms. But in practice, due to inhomogeneous mixing of powders the melt formation occurs at  $1465^\circ\text{C}$ . In W-Ni-Fe system tungsten grains are embedded in the ductile Ni-Fe matrix. The solubility of W in the matrix is low. But due to increase in nickel

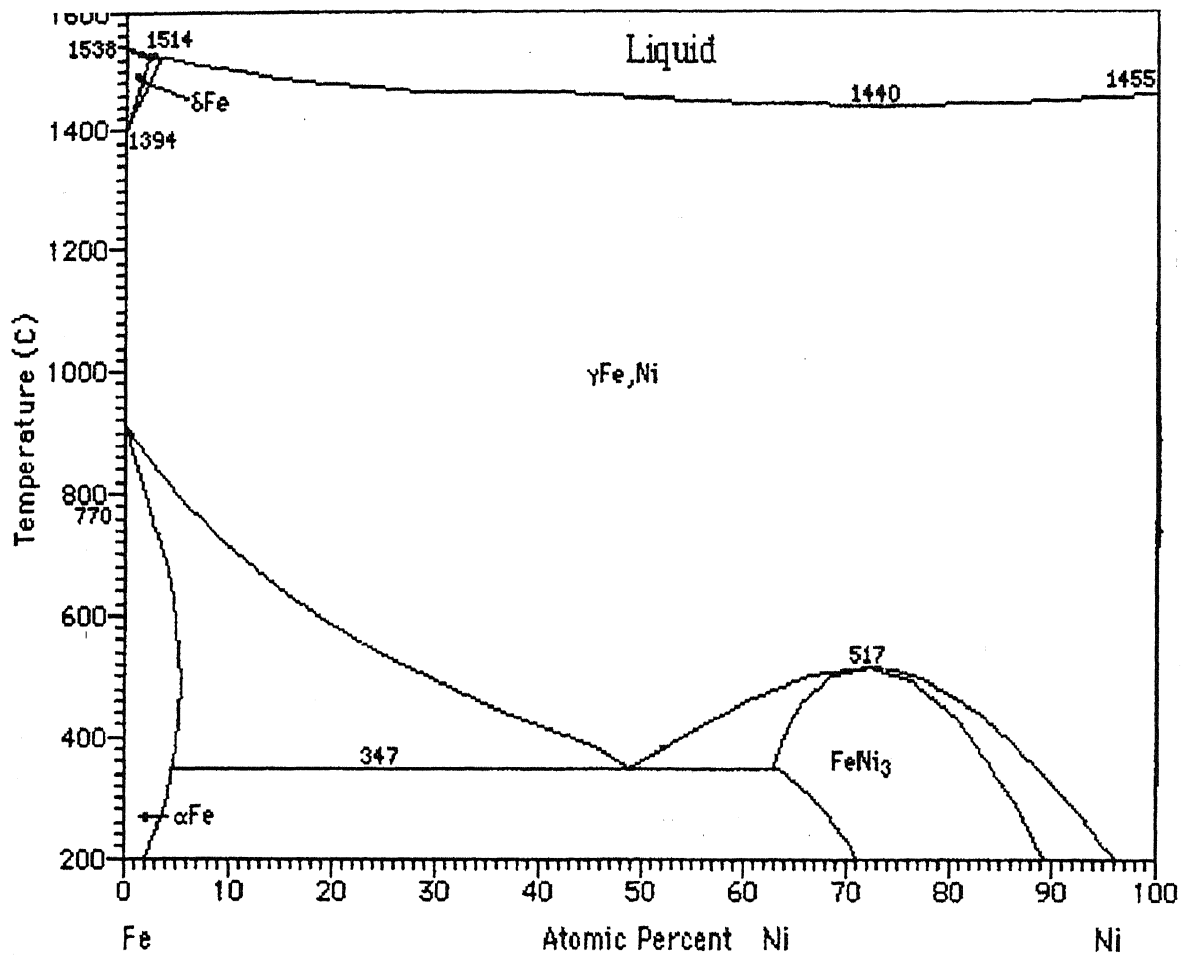


Figure 2.2. Fe-Ni Equilibrium phase diagram [15].

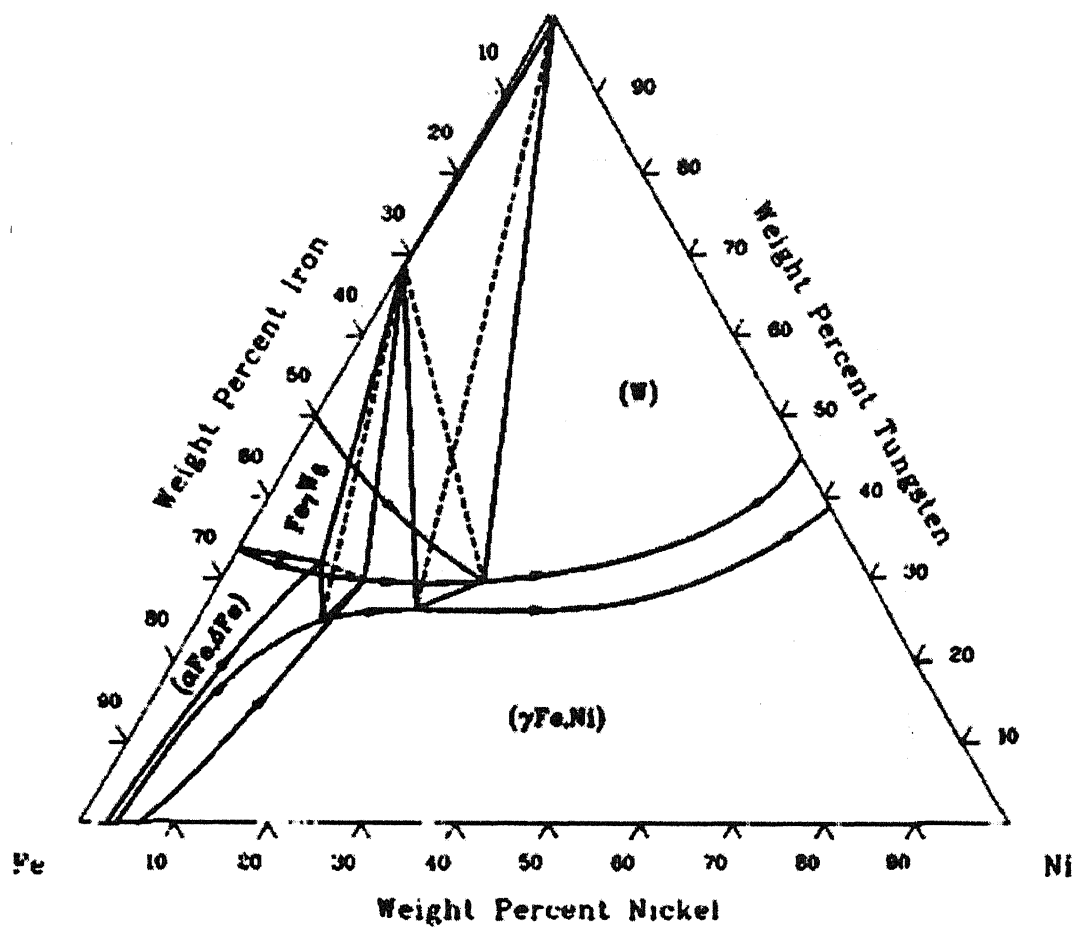


Figure 2.3. Ternary phase diagram of W-Ni-Fe alloys [16].

content in the system the solubility of tungsten increase, which is harmful in respect of mechanical property.

The formation of different intermetallics depends upon Ni to Fe ratio in the system. It is minimum when the nickel to iron ratio is 7:3. Nickel to iron ratio plays an important role in the selection of W-Ni-Fe alloys for specific applications. Typically Ni to Fe ratio ranges between 1:1 and 4:1. Various researches have been carried out in variation of nickel to iron ratio on the mechanical properties of W-Ni-Fe alloys. Mechanical properties of as sintered alloy depend upon the Ni:Fe ratio [17]. The most important factor that should be considered for selecting is to avoid the formation of brittle intermetallic phases at the tungsten /matrix interface.

Among the various Ni to Fe ratios studied, 7:3 and 8:2 are frequently used, with a large number of investigations using 7:3. The selection of Ni to Fe ratio of 7:3 effectively prevents the formation of brittle intermetallic phases. In another report Caldwell [18] has argued that it is possible to use higher or lower Ni to Fe ratio and to achieve high mechanical properties by using proper heat treatment. Ni to Fe ratio higher than either 7:3 or 8:2 can significantly improves mechanical properties if proper heat treatment is performed to control the precipitation of brittle intermetallic phases.

### **2.3. Sintering**

The term sintering is defined as a thermal treatment for bonding particles into a coherent predominantly solid structure *via* mass transport events that usually occur on atomic levels [19]. The driving force for sintering is lowering of total surface energy, which occurs by reduction in surface area with concomitant of inter-particle bonds. Such bonding generally results in the improvement of properties like strength, ductility, conductivity,

magnetic properties and corrosion resistance. The sintering process has many parameters depending upon processing conditions, such as the presence of multiple phases, applied pressure, sintering time and temperature, etc. Figure 2.4 shows various sintering processes and subdivisions in terms of key processing parameters [19]. Several systems like super-alloys, tool steels, tungsten heavy alloys, bronzes, etc. are sintered at a temperature where one of the phases forms a liquid. The consolidation process is therefore termed as liquid phase sintering.

#### **2.4. Liquid Phase Sintering: An Overview**

As compared to conventional foundry techniques, liquid phase sintering offers the advantages of relatively low sintering temperature, near-net shaping, high final density, high material utilization (>95 %) and unique two phase microstructures that provide superior material properties [20]. Because of the cost and productivity advantages, nowadays, nearly three-fourth of sintered products involves a liquid phase at some point or other during processing [12].

Usually, the mass transport rate through liquids is higher than through the solids. Thus, the presence of the liquid phase generally enhances the densification kinetics relative to solid state sintering. Furthermore, the liquid layer is frequently lubricating in nature, which results in a better packing of the solid grains and a high compact density. The liquid phase sintered microstructure consists of one or more phases interspersed with a phase that is liquid at sintering temperature. A typical liquid phase sintered heavy alloy microstructure is shown in Figure 2.1. The solid content and the solubility of solid in the liquid dictate whether or not the liquid phase is persistent or transient at sintering temperature. Mixed

## SINTERING PROCESSES

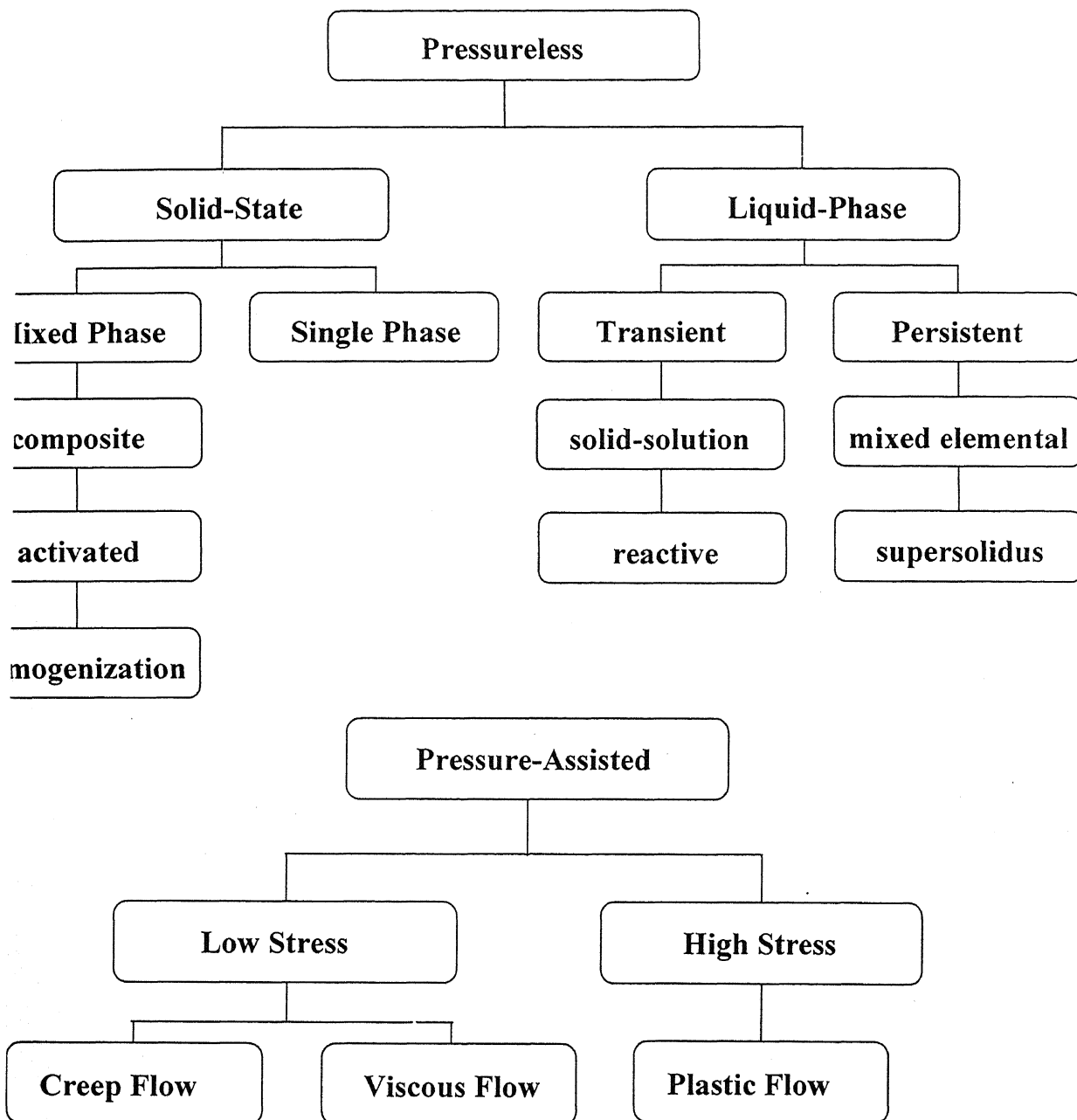


**Figure 2.4.** Different sintering pathways in terms of the key processing variables.

powders form a liquid due to melting of one of the components (e.g. W-Cu) or the formation of a eutectic liquid (e.g. WC-Co). Figure 2.5 shows an ideal phase diagram for liquid phase sintering [21]. Figure 2.6 schematically shows the effect of the liquid content on densification [21]. This figure indicates the contribution of the solid-state densification prior to melt formation, which is not considered in the classical conceptualization of liquid phase sintering. The relative importance of each process depends on the quantity of the liquid and solubility.

Kingery and Narasimhan [22] conducted a series of experiments on iron-copper and cemented carbide systems and found that the densification in those alloys occur in three distinct stages, as discussed by Cannon and Lenel [23]. These three stages of densification are: rearrangement, solution-reprecipitation, and final-stage sintering. These three stages of classic (persistent) liquid phase sintering are illustrated in Figure 2.7. The following sections describe the various stages of liquid phase sintering briefly.

#### **2.4.1. Particle Rearrangement**

In liquid phase sintering, once the liquid forms, it will flow to wet the particles. With the condition of good wetting (wetting angle  $\theta < 90^\circ$ ), the liquid phase is pulled by capillary forces into particle necks and small pores [24]. The liquid phase acts as the lubricant and prevents interlocking of particles. Rearrangement is often composed of two phases. Primary rearrangement involves the individual particles. The liquid forms at the additive particles sites. They form liquid which spreads and wets the particles to form cluster. The cluster then continues to compress as the liquid spreads.

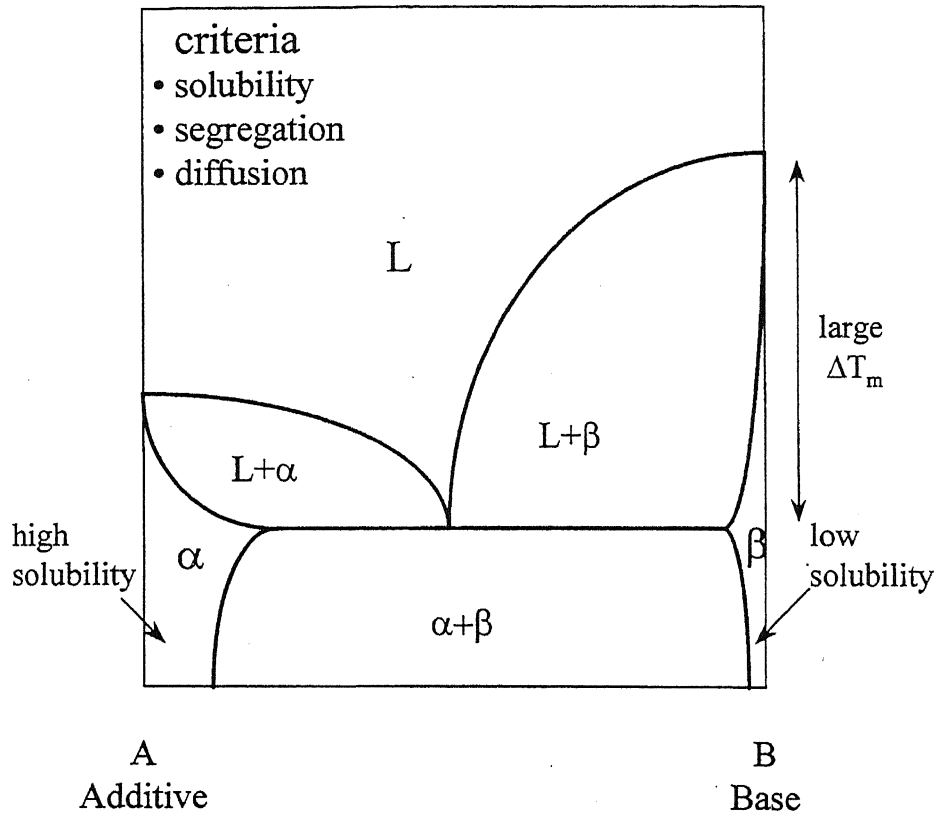


**Figure 2.5.** An ideal binary phase diagram for liquid phase sintering illustrating the solubility variables for additive phase (A) and base metal (B) [21].



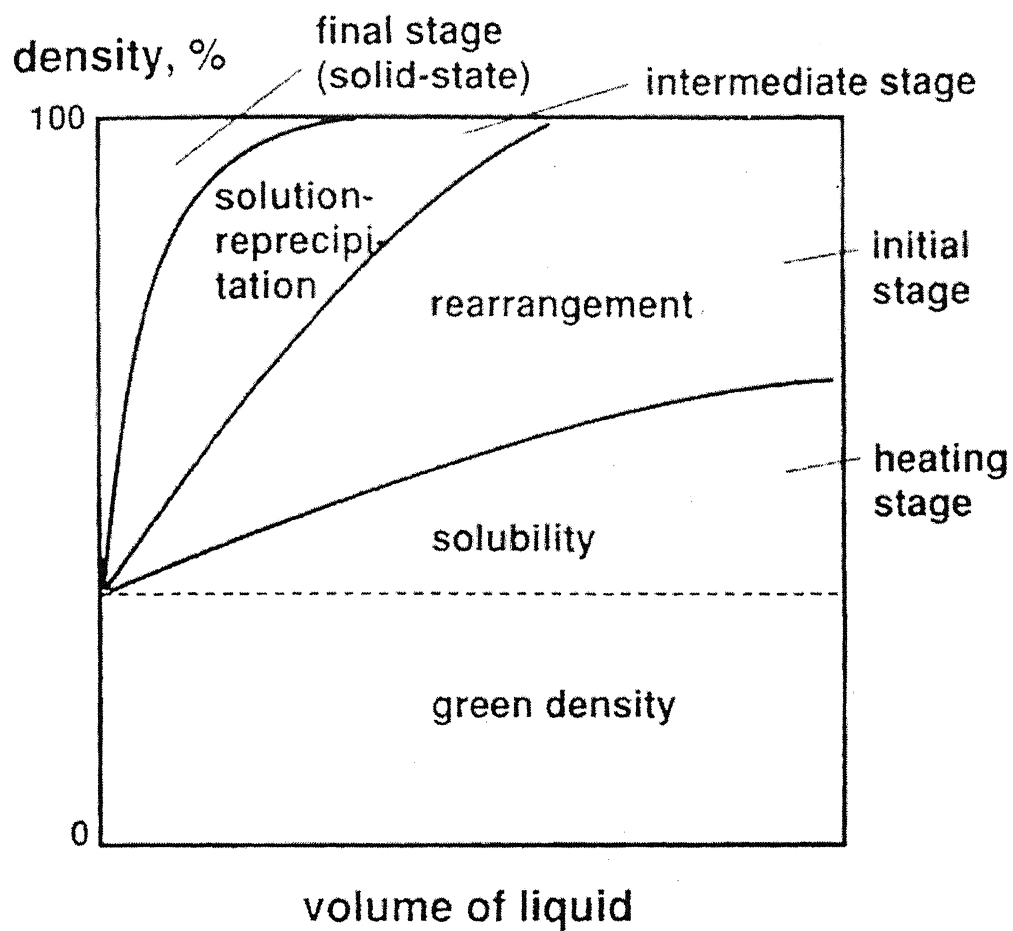
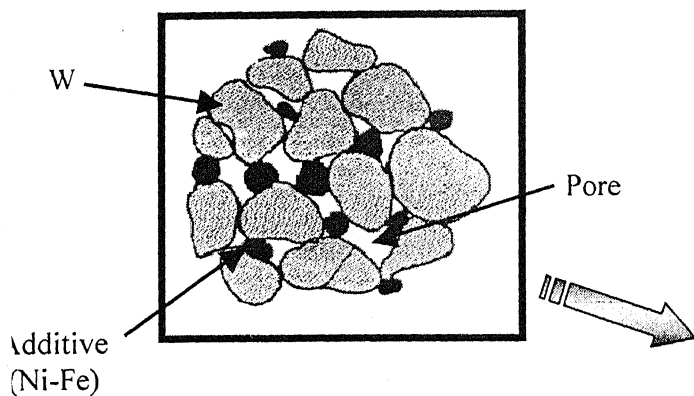
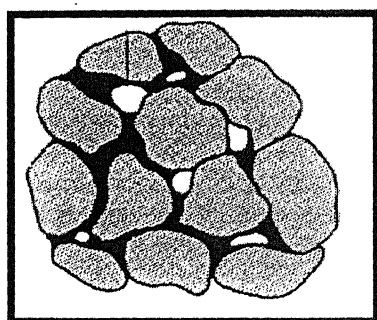
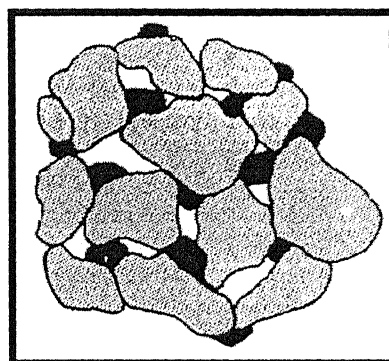


**Figure 2.6.** Diagram showing the effect of the liquid content on densification [21].

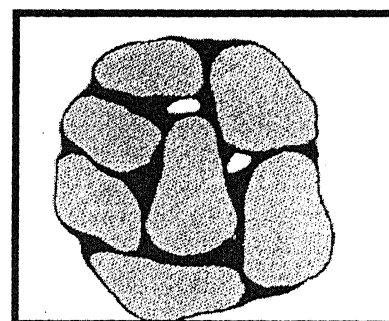
Initial state mixed  
powders



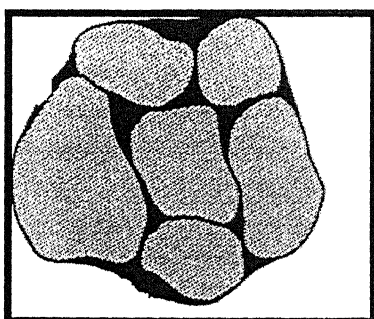
Solid state



Rearrangement



Solution Reprecipitation



Final Densification  
& grain Coarsening

Figure 2.7. Schematic Diagram showing the stages in liquid phase sintering [12].

Secondary rearrangement involves particle disintegration into fragments and subsequent repacking of those fragments. The low melting liquid forms and penetrates into the grain boundaries thereby causing particle fragmentation.

Huppmann *et al.* [25] experimentally confirmed that a low wetting angle and uniform powder homogeneity enhance the contribution of rearrangement of densification. It was shown that a very large contact angle promotes swelling rather than shrinkage. The other important variables to control the process are, particle size, shape and volume fraction of the liquid. Smaller particles have got more surface area, so the surface energy will be higher. This results into the higher densification compared to the coarse particles. Lower green densities also improve the densification rate. In general, the densification rate is reduced by a high green density; because as the green density increases, there is more mechanical interlocking and less vapour phase. As a result capillary force responsible for rearrangement is reduced. However, the final density improves because of the lower initial porosity. At a high volume fraction of liquid, complete densification is possible by rearrangement and pore filling on liquid formation. As the volume fraction of liquid decreases, other processes like solution-precipitation must be active for full densification. It is estimated that 35 volume percent liquid is needed to obtain full density by rearrangement processes [26]. In actual case, rearrangement occurs over few seconds.

#### **2.4.2. Solution-Reprecipitation**

In most liquid phase sintering systems, the quantity of liquid is insufficient to fill all the pores space on melt formation. Hence, there will be some remaining porosities after the first stage. Thus, the grain must change their shape and size distribution to achieve a higher packing density for further densification. Thus, further densification occurs from solution

reprecipitation wherein the smaller particles preferentially dissolves in the melt and reprecipitated from the saturated melt on to a larger grain. As a result the large grains become larger and small grains become smaller. This phenomenon is also known as Ostwald ripening. This stage involves particle fragmentation, contact flattening, and grain shape accommodation [25-27].

Two different sets of theories have been proposed to describe the densification mechanism during this stage. Smithells *et al.* [7] proposed that the difference in the chemical potential results in the dissolution of the smaller grains into the liquid phase and their subsequent precipitation on to the larger grains. But according to Kingery [22] the densification occurs from the hydrostatic pressure applied at the interparticle contact because of the capillary action of the pores present at the particle junctions.

A general attribute of solution-reprecipitation processes is microstructural coarsening [26]. The coarsening is due to a distribution of grain sizes. The solubility of a grain inversely varies of its size. The difference in the solubilities establishes concentration gradient in the liquid. Material transportation occurs from the small grains to large grains as stated earlier. It should be remembered that this stage not only gives rise to the grain coarsening, but contributes to densification also.

#### **2.4.3. Microstructural Coarsening and Coalescence**

As the grain contacts, neck growth occurs by solid-state diffusion along the grain boundary that focus at the contact to give densification [28]. This is the third and last stage of liquid phase sintering. In this stage is controlled by densification of the solid structure. Rigid skeleton of contacting solid grains, decreases the densification rate in this step. The residual pores will enlarge if they contain entrapped gas. During the pore growth, pressure

in the pores decreases, giving compact swelling. Prolong sintering time will lead to the increase in the grain size and as a result the properties of the sintered material will degrade. Hence the stage is avoided by use of short sintering time. This stage is not so important in liquid phase sintering. However, in the systems like W-Cu, W-Ag, WC-Cu etc., which have got limited solid solubility in the liquid, this process plays an important role. There the densification generally occurs by rearrangement and solid-state sintering.

It has also been reported that compact shape and changes in microstructure during liquid phase sintering are affected by the initial pore structure and alloy composition [22]. Pores affect densification and distortion in liquid phase sintering. If pores are not saturated by liquid during rearrangement, residual capillary forces help to resist distortion. However once the pores are filled and the capillary forces are lost, only solid bonds can provide strength. If the solid bonds have not formed due to grain rearrangement, the component strength falls to a level that cannot resist distortion. Upadhyaya and Srikanth [29] studied the effect of particle size and binder composition on sintering properties of heavy alloys. They found that finer tungsten particle size gives better-sintered properties. They also studied the effect of binder composition and sintering temperature on sintered properties. In liquid phase sintering larger grains grow at the expense of the smaller grains. Yoon *et al.* have done work on grain coarsening of W-Ni-Fe heavy alloys. They have reported that with limited amount of liquid phase present, under the influence of the densification force arising from the pores, grain growth occurs preferentially away from the areas where the grains are in close contact. Thus grain shape accommodation occurs during growth and this enables complete densification.

## 2.5. Processing of W-Ni-Fe Heavy Alloys

As tungsten is the highest melting point (3420°C) refractory metal known, Powder Metallurgy processing is the only method for fabrication of these alloys. Figure 2.8 shows the schematic view of processing method of W-Ni-Fe heavy alloys [30]. It is clear from the Figure 2.1 that in solid-state sintered alloy enough porosity remains; however liquid phase sintered alloy has rounded tungsten spheroids in nickel/iron matrix without any porosity. As it is a well known fact that the properties of heavy alloys vary with process parameters such as sintering temperature, time and atmosphere. Eroglu and Baykara [31] have reported that for finer grade tungsten powder alloys prepared by attritor milled powder gives higher strength and ductility as compared to those prepared by mixed powders. However, compared to finer grade, the coarser tungsten powder generally resulted in alloys with higher ductility when mixer was used. Asthana and Upadhyaya [32] have studied the effect of different type of ball millings on size distribution of powders. They found that planetary milling is more effective than centrifugal milling for reduction in particle size. Suryanarayana [33] has reported that narrower particle size distribution in case of attritor milled powder as compared to ball milled powder.

In the compaction of tungsten heavy alloy systems for powder metallurgy, most common techniques are used such as conventional die compaction and hot and cold isostatic pressing, powder rolling for making sheets, extrusion for rods and more recently, powder injection molding [30].

### 2.5.1. Conventional Sintering of WHAs

Tungsten heavy alloys are consolidated *via* solid state sintering or liquid phase sintering. It is possible to achieve full densification in WHA powder compacts by sintering

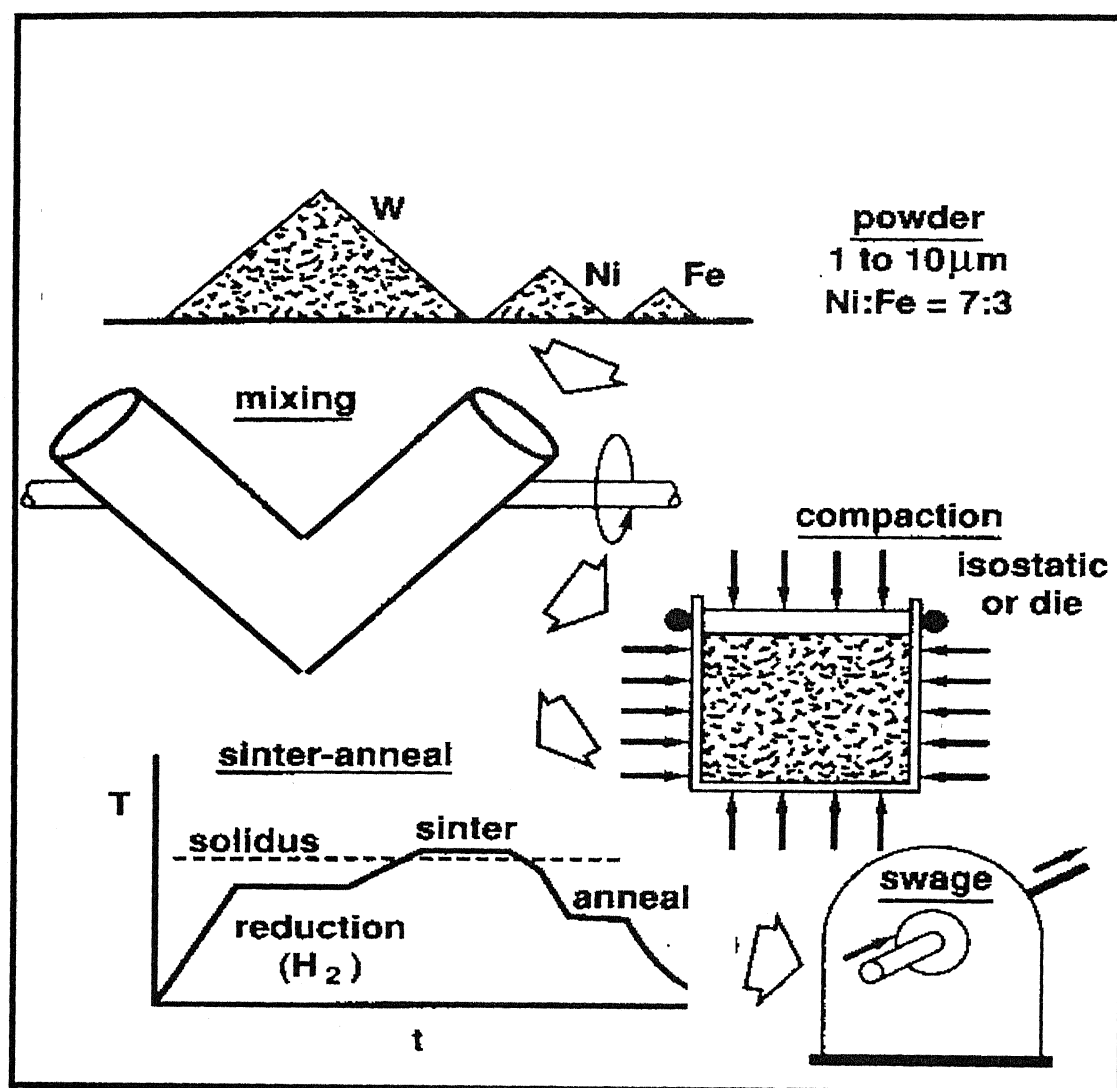


Figure 2.8. Conventional Process for fabrication of tungsten heavy alloys [30].

by choosing either smaller starting tungsten powder ( $< 3\mu\text{m}$ ) or by milling the powder in order to reduce its size. Ryu *et al.* [34] reported that mechanically alloyed W-Ni-Fe compacts can be densified to 99% of its theoretical density through solid-state sintering at  $1300^\circ\text{C}$ . While these solid-state sintered alloys exhibited high yield strength (up to 1100 MPa) and hardness (about 300 HV), however, they suffered from poor ductility and impact energy due to a large fraction of brittle tungsten-tungsten interface. Caldwell investigated the effect of variables such as powder mixing, sintering temperature on the sinterability of WHAs and showed that compositions prepared using 1 tungsten powder can be fully densified at temperatures near the matrix solidus. One way to enhance the ductility is by increasing the binder content. However, the disadvantage for the high binder content alloy is its lower density ( $14\text{ g/cm}^3$ ) as compared to conventional tungsten heavy alloys, which typically contain more than 90% tungsten. Lenel *et al.* [36] also investigated the role of post-sintering heat-treatment on the mechanical properties of 70W-21Ni-9Fe alloy (wt. %) and reported that solid-state sintering followed by vacuum annealing resulted in high ductility. To ensure high ductility and toughness, tungsten heavy alloys are usually consolidated to full density through liquid phase sintering. As compared to solid-state sintered alloys, the grains in liquid phase sintered alloy are coarser, more rounded, and less contiguous.

### 2.5.2. Microwave Sintering

Microwave heating is fundamentally different from conventional heating. Figure 2.5.1 shows the comparison of conventional and microwave heating. The microwave provides volumetric heating and an enhanced densification. Sintering temperatures and processing times are significantly reduced compared to conventional sintering.



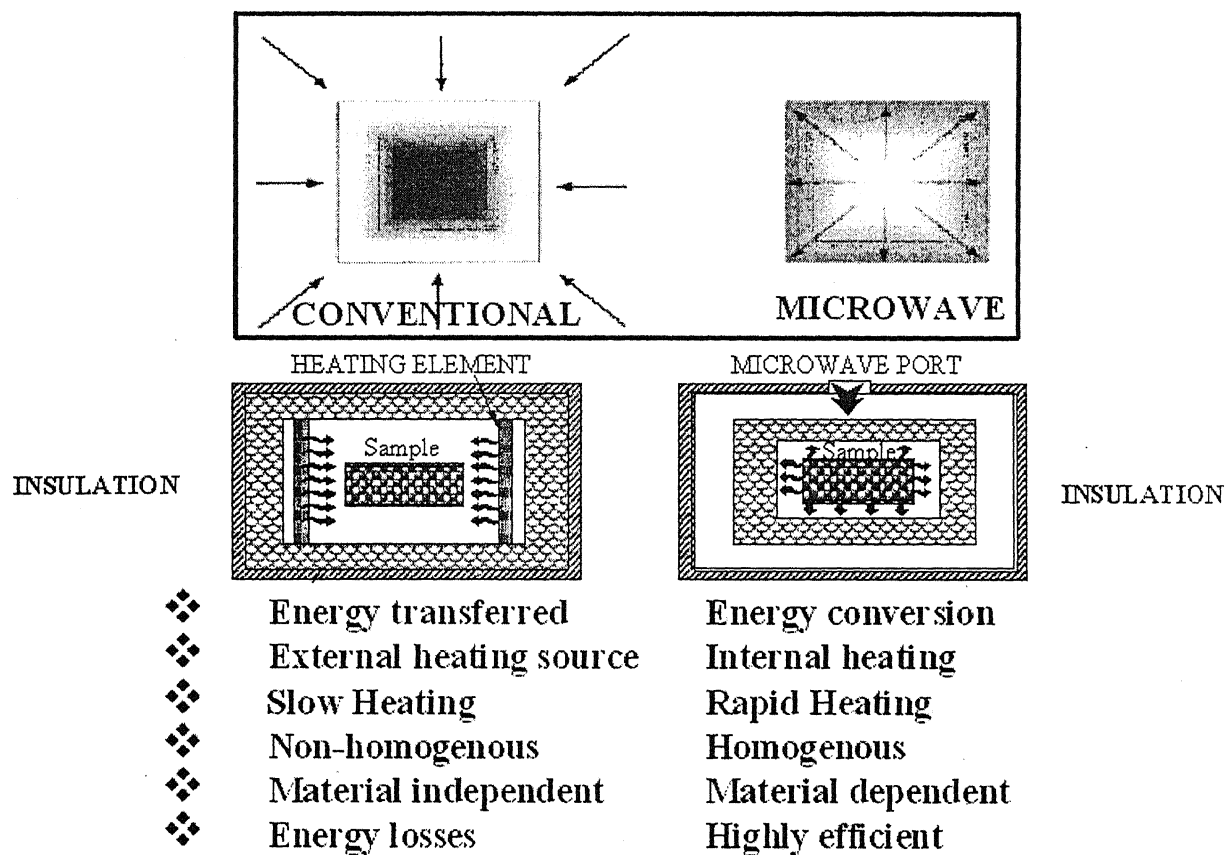


Figure 2.9. Comparison of conventional and microwave heating [46].

time can be considerably reduced in comparison with conventional techniques. Thus, grain growth can be limited by this microwave sintering technique. Conventional heat processing is accomplished by heating the outside of the process material, and then the heat travels inwards by conduction (and convection in liquids and gasses). The speed of conductive (and convective) heating is controlled by many things, most notably by differences between the surface temperature and internal temperature of the material and the ability of the material to conduct heat. The usual way to speed up the rate of conventional heating is to increase surface temperature. Problems with damage caused by surface overheating and temperature variations within the material can be avoided through the use of EM heating. Because energy is delivered instantaneously throughout the mass of the material, achieving controlled heating rates and accurate process temperatures becomes easier.

#### **2.5.2.1. Basics of Microwave Interaction with Materials**

Microwaves are nothing but electromagnetic waves that have a frequency range from around 0.3 GHz to 300 GHz with corresponding wavelengths ranging from 1m to 1mm. When electromagnetic (EM) energy is applied to a material some of it is reflected by the surface of the material, some is transmitted through the material and some is absorbed within the material.

Microwave heating is based upon the capacity of a material to absorb the electromagnetic energy. It is known that in dielectric materials the external electric field causes a redistribution of internal bound charges, which results in the polarization of the material. A measure of such a response of a material to an external electric field is the dielectric permittivity,  $\epsilon$ . If the external electric field is alternating (ac), the dielectric

response of the material follows it, generally with some lag behind the field changes. To describe this phenomenon quantitatively a complex dielectric permittivity that depends on the field frequency,  $\omega$ , is formally introduced:  $\varepsilon(\omega) = \varepsilon'(\omega) + j\varepsilon''(\omega)$ . The imaginary part of the dielectric permittivity is greater the larger the lag. The change of polarization, i.e. the redistribution of internal charges, is accompanied by the motion of electric charge, i.e. by the electric ac current, which generates heat inside the material. The effective high-frequency conductivity,  $\sigma$ , can be introduced in order to characterize the power of heating, similar to the case of a dc current. The power of heating per unit volume, which equals the absorbed microwave power, is

$$w = \sigma E^2 \dots\dots\dots (2.1)$$

where,  $E$  is electric field strength inside the material. The effective high-frequency conductivity is unambiguously linked to the imaginary part of the dielectric permittivity,  $\sigma = \omega\varepsilon_0\varepsilon''$ , where  $\varepsilon_0$  is a constant called the permittivity of free space [37].

Because of absorption, the electromagnetic fields decrease as the wave passes through the material. The dissipation of electromagnetic energy is commonly characterized by the so-called loss factor,  $\tan \delta = \varepsilon''/\varepsilon'$ . The attenuation of the electromagnetic wave can also be characterized by a penetration depth (or skin depth), on which the field strength is reduced by a factor of  $e = 2.71\dots$ :

$$l = \frac{c}{\omega} \sqrt{\frac{2[1 + \sqrt{1 + \tan^2 \delta}]}{\varepsilon'(\tan \delta)^2}} \dots\dots\dots (2.2)$$

where,  $c$  is the velocity of light.

When the electromagnetic wave is incident (from air or vacuum) onto a plane surface of material, it is partly reflected from the surface and partly penetrates into the material.

For a normal incidence of the electromagnetic wave on a plane boundary between material and vacuum, the fraction of reflected power (reflection coefficient) is [37],

$$R = \frac{1 - \sqrt{2\varepsilon'[1 + \sqrt{1 + (1 + \tan \delta)^2}] + \varepsilon'\sqrt{(1 + \tan \delta)^2}}}{1 + \sqrt{2\varepsilon'[1 + \sqrt{1 + (1 + \tan \delta)^2}] + \varepsilon'\sqrt{(1 + \tan \delta)^2}}} \dots\dots\dots (2.3)$$

Any of the heating processes that use the electromagnetic energy can be characterized by the two parameters,  $I$  and  $R$ . The frequency dependence of the dielectric permittivity determines the particular features of heating by electromagnetic radiation of different frequency ranges. In conventional furnace heating, energy is transferred to the materials by thermal electromagnetic radiation, with its maximum intensity being in the infrared range. The penetration depth of infrared radiation ( $\omega \geq 10^{13} \text{ s}^{-1}$ ) is very small ( $I < 10^{-4} \text{ m}$ ) in majority of solids. Therefore, energy deposition is localized within a thin layer near the surface of material. As a result, conventional heating essentially depends on heat transfer from the hotter near-surface region to the colder bulk of the material.

In the microwave frequency range, the absorption properties of non-metallic materials vary greatly. The loss factor,  $\tan \delta$ , varies at room temperature from  $10^{-4}$  -  $10^{-3}$  (e. g. in pure alumina and silicon nitride) up to 1 and higher (in carbides, borides, some oxides, and intermetallic compounds). Correspondingly, the penetration depth varies from meters to fractions of a millimeter. Thus, knowledge of the dielectric properties of materials, as well as their dependence on frequency, temperature, chemical composition, and microstructure is of paramount importance for the intelligent use of microwave energy for high-temperature processing.

The physical mechanisms of microwave absorption have long been studied and an exhaustive account of them can be found in practically any monograph on electromagnetic

waves in dielectrics [38]. However, the theory of interaction between microwave electromagnetic fields and materials is capable of giving only qualitative information on the dielectric properties of materials and their frequency dependence. The reason is that the mechanisms of interaction and their effectiveness are strongly dependent on the structure of materials, type and strength of chemical bonds between atoms. At most, the theoretical considerations are able to predict the character of the dependence  $\epsilon(\omega)$  but fail to calculate the magnitude of the dielectric permittivity at a given frequency. Therefore, the direct measurement of the dielectric properties appears the only method to obtain quantitative information on them. Various experimental techniques exist for measuring dielectric properties in a wide frequency range up to several hundred GHz. With increase in frequency, the experimental methods vary from the coaxial line and waveguide techniques commonly used for decimeter wavelengths to open quasioptical resonators and interferometers exploited in the microwave range [39].

The materials commonly subjected to microwave processing can be categorized according to their microwave absorption properties (expressed by either the imaginary part of dielectric permittivity,  $\epsilon''$ , loss tangent,  $\tan \delta$  or effective conductivity,  $\sigma$ ). Materials may be divided into four categories depending upon their interaction with electromagnetic radiations:

1. **Conductors:** Materials with free electrons, such as metals, reflect electromagnetic waves just as the light is reflected by a mirror. These materials are used to contain and direct electromagnetic waves in the form of electrodes, applicators and wave guides.

2. **Insulators:** Electrically non-conductive materials, such as glass, ceramics, and air are insulators, which reflect and absorb electromagnetic waves to a negligible extent and primarily transmit them (i.e. they are transparent to the waves). They are, therefore, useful to support or contain materials to be heated by electromagnetic field and may take the form of conveyor belts, support trays, dishes or others. The polymers and some inorganics fit this category, but under certain conditions, may become dielectrics. Heating a polymer past its heating distortion temperature is an example. Some materials also may heat poorly at one frequency but heat well at another. Also, use of specially designed applicators may cause materials to heat well whereas they are virtually transparent in home microwave ovens.
3. **Dielectrics:** These are the materials whose properties range from conductors to insulators. This is the group that absorbs electromagnetic energy and converts it to heat. Examples of dielectrics are water, oils, wood, food, and materials containing moisture.
4. **Magnetic compounds:** These are materials, such as ferrites, that interact with the magnetic component of the electromagnetic wave and as such will heat. They are often used as shielding or choking devices that prevent leakage of electromagnetic energy. They may also be used for heating in special devices.

The problems encountered in the microwave heating of materials exhibiting low ( $\tan \delta \leq 10^{-3}$ ) and high ( $\tan \delta \geq 10^{-1}$ ) absorption are quite different, as are the methods for their solution. It is therefore instinctive to consider the cases of low-loss and high-loss materials separately.

At room temperature, dielectric losses of low-absorption materials are caused by the displacement of bound charge carriers in such processes as atomic lattice vibrations and dipole reorientation. Among these materials are pure oxides ( $\text{Al}_2\text{O}_3$ ,  $\text{BeO}$ ,  $\text{SiO}_2$ ) and nitrides ( $\text{BN}$ ,  $\text{Si}_3\text{N}_4$ ,  $\text{AlN}$ ). Low microwave absorption makes it generally inefficient to heat these materials by the radiation of the decimeter-wave range ( $\leq 2.45$  GHz), traditionally used for microwave applications. However, even at these low frequencies the heating of these materials is possible if the sample undergoing processing is placed into a resonant cavity which concentrates the electromagnetic field within the sample as shown in Figure 2.10a. In this case heating is achieved owing to multiple passes of the electromagnetic wave through a sample, even if its size is much less than the penetration depth of radiation, *I*. Another approach employs the so-called hybrid heating schemes where ionic conduction and dipole rotation both are effective. In essence, they involve introduction of additional heat sources into the system. In particular, the role of these sources can be played by microwave-absorbing objects (susceptors), from which the microwave-generated heat is transferred to the low-loss material undergoing processing [40].

At elevated temperatures, microwave absorption in most materials grows sharply, primarily due to an onset of another absorption mechanism. This is characteristic for both solids with ionic ( $\text{Al}_2\text{O}_3$ ,  $\text{ZrO}_2$ ) and covalent ( $\text{Si}_3\text{N}_4$ ,  $\text{AlN}$ ) bonding. A sharp increase in the microwave loss starts at temperatures of about  $0.4 - 0.5 T_m$  (where  $T_m$  is the melting temperature of the material). In this temperature range the bonds between ions in ionic crystals start to break, and the electrons in covalent materials begin to populate the conduction bands. Due to the sharp increase in the losses, there is no need for hybrid heating at elevated temperatures. A correctly designed susceptor system would provide

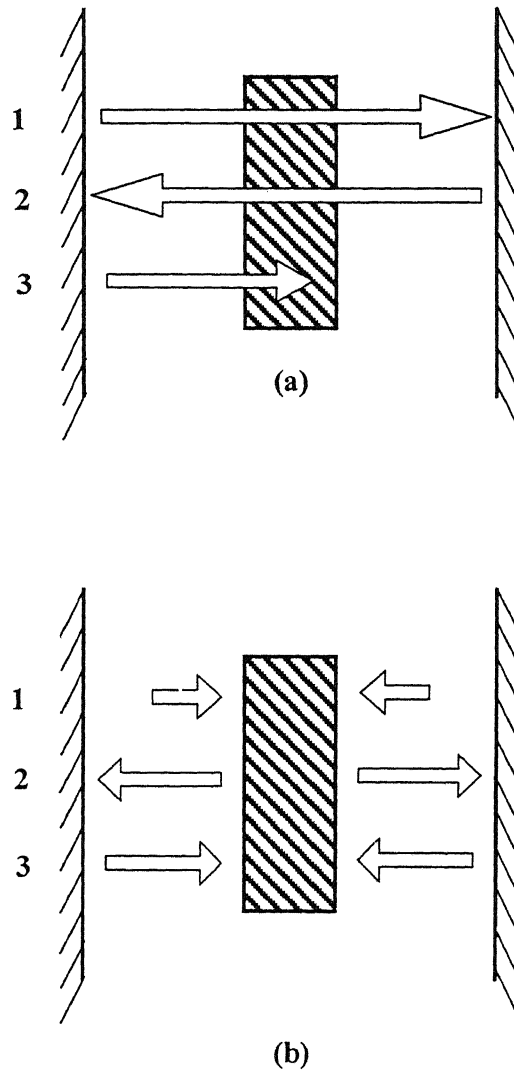


**Figure 2.10.** Illustration of (a) a low-loss sample: 1, incident radiation; 2 and 3, radiation returned to the sample after reflection from resonator walls and (b) a high-loss sample: 1, incident radiation; 2, radiation reflected from the sample; 3, radiation returned to the sample after reflection from resonator walls



heating at the initial stage, and reflect most of the power at high temperatures when microwaves are absorbed directly by the material undergoing processing.

The sharp increase in microwave absorption with temperature can cause a thermal instability, which is commonly known as a temperature runaway. The problem of a temperature runaway is widely discussed in the literature on the microwave processing of materials [41]. It is pertinent not only to high-temperature processes. The nature of this instability is easy to understand. An increase in the local temperature is accompanied by an enhancement of microwave energy absorption, which results in the local acceleration of heating and further growth of temperature. The instability develops provided that the microwave power exceeds some threshold value, which corresponds to an S-type dynamic curve of the temperature versus power [42].

Heating of low-loss materials becomes much easier at higher frequencies of microwave radiation, i.e. in the microwave range. This is due to the fact that the dielectric losses of these materials increase with frequency. For example, the sintering of high-purity  $\text{Al}_2\text{O}_3$  ceramics, one of the least-absorbing materials, at a frequency of 30 GHz has demonstrated that the heating rates of about several tens of degrees centigrade per minute can be easily achieved by direct absorption of the microwave energy by the material [43-45]. There is also evidence [46-47] that in many materials the temperature dependence of dielectric losses in the microwave range is not so sharp. Therefore, the problem of a temperature runaway becomes less severe with an increase in the frequency of the radiation used for heating. If this phenomenon is of a general nature, it can be a major argument in favor of using microwave power for the high-temperature processing of materials.

In principle, the dependence of the microwave absorption of materials on frequency opens a way to controllably shape the temperature distribution by simultaneously using

adiation of two different frequencies. The simultaneous application of microwaves of frequencies 2.45 GHz and 30 GHz was discussed in [48]; however, no experimental results of an attempt to accomplish double-frequency heating have been reported to date.

In the case of highly absorptive materials (with  $\tan \delta \geq 10^{-1}$ ) the effective conductivity is typically so large that a strong reflection of radiation from the surface inhibits microwave heating as shown in Figure 2.10b. The absorbed fraction of the incident microwave power can be estimated approximately as,

$$1 - R \approx 2\sqrt{\frac{2}{\varepsilon' \tan \delta}} \dots\dots\dots (2.4)$$

In microwave processing practice most of the materials are heterogeneous. For example, ceramic materials at all stages of densification remain a two-component mixture of solid material in the grains and voids between the grains. The heterogeneous composition of many other materials is dictated by their applications. For example, metal-ceramic composites are commonly used for producing hardmetal machine tools [18]. Composites formed as a dielectric matrix with metal particle inclusions are known as good absorbers of microwave and infrared radiation [49]. Functionally graded materials with specially tailored composition are promising for the development of high-temperature thermal barrier coatings [50]. In fact, applications of heterogeneous materials are much more diverse compared to materials of homogeneous composition.

When a composite material contains conductive (metal) particles embedded in a low-loss host material, it may absorb microwaves due to the magnetic polarization of particles [51]. The oscillating magnetic component of the microwave electromagnetic field induces electric currents within the particles. Depending on the particle size, these currents may be much stronger than those driven directly by the electric component of the field. The

process of heating by the current induced by an oscillating magnetic field is usually termed induction heating.

#### 2.5.2.2. Advantages of Microwave Heating

- **Reduced energy consumption and process time**

The main advantages of microwave heating stem from direct energy deposition in the volume of a material. This eliminates the need for spending energy on heating the walls of the furnace or reactor, its massive components, and heat carriers. As a result, the use of microwave methods significantly reduces energy consumption, especially in high-temperature processes, since heat losses grow drastically with an increase in the process temperature. The volumetric nature of energy deposition accelerates heating, which reduces the time needed to complete a process. An idea of the energy saving potential of microwave processing can be inferred from the results of a number of comparative studies in sintering. Birman *et al.* [48] has shown that the specific energy consumption in the process of sintering alumina-based ceramics at a temperature of 1600°C is about 4 kWh kg<sup>-1</sup> for microwave heating versus 59 kWh kg<sup>-1</sup> for fast conventional heating in a resistive furnace. For the sintering of silicon nitride based ceramics, the specific energy consumption is 3 kWh kg<sup>-1</sup> over a 2 h process of microwave sintering versus 20 kWh kg<sup>-1</sup> over a 12 h conventional process.

The reduction in process time under microwave heating is especially significant when the process involves endothermic chemical reactions and/or phase transformations and the temperature is limited from above (either by the capabilities of the system or by product quality). In this case a sufficient energy supply is a prerequisite for a high process rate, which is determined at each point by the local temperature. Conventionally, the energy

supply rate is always limited by slow heat transfer processes. Due to volumetric energy deposition, microwave heating is, in principle, capable of providing any desired rate of an endothermic process, limited only by the power of the microwave source.

However, it should be emphasized that the advantages of using microwave energy in high-temperature processes are by no means reduced only to energy saving. In many cases microwave processing is capable of improving the product quality or leads to results that cannot be achieved conventionally.

- **Rapid and controllable heating**

High rates of heating lead not only to reductions in process time and energy consumption but, many high-temperature processes include a sequence of various steps which replace each other with the rise of temperature. Such sequences occur in multistage thermally activated processes, in which separate stages are characterized by different values of the activation energy. Some of these stages may have a negative influence on the properties of the final product. In such cases rapid heating may be vital for reducing the role of undesired intermediate stages of the process.

An example of such a multistage process is the sintering of ceramics. At different steps of sintering the diffusion processes of various natures, viz surface, grain boundary, and bulk diffusion, determine the mass transport. It is well-known [22] that inhibition of surface diffusion at the initial stage of densification is favorable for sintering. An increase in the rate of heating at the onset of densification can reduce the formation of a rigid neck structure between grains, which occurs primarily by surface diffusion, and retain high enough driving forces for densification.

An advantageous method for ceramics sintering based on the idea of inhibiting surface diffusion is rate-controlled processing [52]. In this approach the heating rate is

varied during the process to keep the prescribed densification rate. The implementation of rate-controlled sintering by conventional methods is often complicated by thermal inertia. The direct deposition of microwave energy is highly relevant to the task of inertialess control over heating. The temperature of the sample undergoing sintering is controlled, in this case, by means of a feedback loop that uses data from in situ density and temperature measurements and that varies the microwave power according to the prescribed schedule of densification versus temperature. In fact, many experiments on the microwave sintering of ceramics, although not pursuing rate-controlled processing, use variable heating rates to decrease the detrimental effect of surface diffusion during the initial densification [44].

At the intermediate and final stages of sintering high rates of microwave heating help overcome grain growth, resulting in ceramic materials with fine microstructure, which in turn enhances their mechanical properties. It appears that the capability of accomplishing fast microwave heating is a factor of paramount importance in the sintering of nanostructured ceramic and composite materials. The growing interest in the nanostructured materials is associated with the recognition of their great potential for various applications, such as near net shape forming, diffusion bonding, and layered composite structures. All these applications are based on the enhanced plasticity of nanostructured materials.

The main obstacle for the fabrication of nanostructured ceramic materials via high-temperature sintering is the problem of grain growth by recrystallization. Since the first attempt to use fast microwave heating for the sintering of nanostructured materials, when 90% dense  $\text{TiO}_2$  ceramics with average grain size of less than 20 nm were obtained, substantial research in this field has been accomplished [38]. The microhardness of samples sintered with micro waves was systematically higher than that of the conventionally

intered samples. In samples of high density the microhardness of sintered sample exceeded the microhardness of single-crystalline titania (rutile) by about 10%. Such enhancement of the microhardness in the microwave sintered samples can be explained by the presence of a significant portion of material in the form of nanosized grains. The deformation of material under indentation mostly occurs via generation of dislocations in grains, and it is accepted that dislocations can be generated only in the crystals whose size exceeds a certain value (on the order of tens of nanometres) [43]. In a recent compressive deformation study [44] an appreciable strain rate was observed in the samples of microwave sintered  $\text{TiO}_2$  at a temperature of  $850^\circ\text{C}$ , whereas no strain was detected in the samples sintered conventionally. This is evidence for the enhanced plasticity of the microwave sintered nanostructured ceramic samples.

- **Inverse temperature profile**

As was mentioned above, microwave heating results in a specific temperature distribution with a maximum within the body. For many processes this temperature non-uniformity is an unambiguous disadvantage since it may result in the non-uniformity of product properties. In particular, in ceramics sintering, which has probably attracted the greatest amount of interest in microwave processing research, temperature non-uniformity is especially undesirable since the internal stresses caused by non-uniform densification [47] may lead to destruction of the product. Therefore various measures are taken in order to overcome temperature non-uniformities, including thermal insulation and the use of additional heat sources. There is no universal solution to this problem; it should be sought specifically for any particular application. A straightforward approach is to surround the body with additional electric heaters, the power in which is controlled to make up for the surface heat losses [48]. However, this approach encounters great difficulties in

plementation. A number of issues such as microwave and environmental compatibility, temperature control, product shape etc make this method feasible only at the expense of loss of universality. Another approach, most commonly used in the high-temperature microwave processing, is based on thermally insulating the material undergoing processing. In some cases the material is surrounded by microwave susceptors, i.e. by objects possessing strong microwave absorption which provide additional heat flow to the surface of the sample. Since these techniques use only one source of energy, viz microwaves, it is difficult to adjust the properties of the thermal insulation arrangement or microwave susceptors so that they would compensate accurately enough the heat losses in the entire temperature range of the process.

Experimentation on microwave ceramics sintering and joining consists largely of a search for the optimal process conditions, which include the temperature-time schedule of microwave heating, the frequency of microwave radiation, thermal insulation properties, possible use of susceptors or additional heat sources, etc. One example of a study where this problem was successfully solved is in the microwave sintering of alumina and silicon nitride ceramic buckets 200 mm in diameter and 200 mm high [49].

It should not be assumed that the microwave-specific temperature distribution has only a detrimental effect on the process of ceramics sintering. In fact, due to the outward temperature decrease from the core of a ceramic body its porous structure remains open to a higher average value of density [12]. This effect contributes both to the acceleration of densification under microwave heating and achieving a higher final density (which is in fact often observed in comparative studies of microwave and conventional sintering). Unfortunately, no attempt has been made to find a quantitative correlation between the major parameters that characterize the evolution of the porous structure in a

inhomogeneous temperature field and the effect of sintering enhancement under microwave sintering.

- **Possibility of surface processing**

If, for a given material and frequency, the microwave penetration depth is small enough, then the deposition of the microwave energy takes place only in the near-surface layer of the material. This regime of microwave heating can be viewed as one more method for the surface treatment of materials by intense energy flows, which can be an alternative or additional to those widely used in practice, such as electron and ion beams, plasma processing, and laser irradiation. Here we will restrict our consideration to the surface processing solely with microwaves, as opposed to microwave-assisted plasma processing of materials [49] and other combinatory techniques. As a rule, a relatively high intensity of radiation is required to make high-temperature surface processing possible. As intensity is determined by the power of the radiation source divided by the area on which this radiation falls, in order to maximize the intensity one should increase the power and focus the radiation onto a spot of minimum possible size. Due to diffraction, the latter cannot be less than the wavelength of radiation. Therefore, microwave surface processing is most feasible in the microwave range, where sources of power on the order of 10-30 kW are available for the frequency range 24-83 GHz [52]. Sharply focused wave beams can be formed using quasi-optical methods for transforming the structure of the electromagnetic field of the operational mode into simpler configurations.

The most serious limitation of microwave surface processing is electric discharge on the surface. The threshold electric field strength for breakdown in air is



much lower in this frequency range than in the infrared and visible parts of the spectrum. The presence of vapors of various substances at the hot surface of material makes the occurrence of a discharge even more likely.

Some of the common uses of microwaves include satellite communications, radar, car phones, air and navigational aids. Other applications include use in industry for melting and drying materials and in medicine in diathermy treatment as well as household use for the preparation of food [42].

### **2.5.3. Alloying Additions and Its Effect on WHAs**

The mechanical properties of WHAs can be improved by addition of fourth elements like Mo or Re. Any body centered cubic material that has high solubility in the matrix material reduces the tungsten solubility. The change in chemical equilibrium due to alloying addition induces the morphological changes [53, 54], which can ultimately affect the mechanical properties of these alloys. Bose and German [55] studied the effect of Mo and Ta additions in W-Ni-Fe heavy alloys. For the tungsten heavy alloys containing molybdenum, the matrix has essentially a constant solubility of 8-11 at.% for the tungsten. Since grain growth constant is directly proportional to the solubility limit of tungsten/combined body centered cubic materials (in case of alloying addition), it reduces due to reduction in solubility limit, which ultimately cause finer tungsten grains resulting higher ultimate tensile strength with considerable ductility. Addition of Mn results in the morphological change of tungsten grains from spherical to angular shape. Addition of cobalt also reduces the grain growth rate [56]. Addition of scavengers such as Ca and La reduces the embrittling effect of phosphorus by forming a stable compound with phosphorus of possibly the form  $\text{LaPO}_4$  [57].

#### 2.3.4. Heat Treatment Effects on WHAs

Sintering of heavy alloys is carried out in  $H_2$  atmosphere to prevent oxidation, swelling and to reduce oxides. The elongation of as liquid phase sintered 96 wt% tungsten (balance Ni and Fe) remains less than 10% [58]. Heat treatment of this, in vacuum at 800°C or at 1150°C in Ar for few minutes can induce ductility up to 20 % [59]. Dissolved hydrogen induces brittleness. Hydrogen weakens mainly the interface between tungsten grain and matrix. Due to low partial pressure of  $H_2$  in Ar Atmosphere, solubility of  $H_2$  reduces and it comes out.

When liquid phase sintered W-Ni-Fe alloys are cyclically heat treated at 1100°C and re-sintered at 1485°C, undulation of W/matrix interface resulted. Due to cyclic heat treatment residual thermal stresses resulted. Local yielding of tungsten grain is believed to occur during the cyclic heat treatment. Undulation appears therefore to result from preferential dissolution of material at regions with higher strain energy and precipitation of materials at regions with lower strain energy [54]. Matrix penetration of grain boundary also occurs due to cyclic heat treatment [60]. It improves ductility due to reduction in W/W brittle interface area. Ageing treatment of tungsten heavy alloys is also done to improve the mechanical properties. Strengthening also occurs by ageing of heavy alloys caused by precipitation hardening of tungsten grains [61]. Thermo-mechanical treatment of tungsten heavy alloys improves the tensile strength, fracture elongation and impact energy [62].

## **Chapter 3**

### **EXPERIMENTAL PROCEDURE**

The present chapter deals with various experimental techniques used for both processing and characterization of the alloy. These are powder characterization, composition preparation, compaction, presintering, sintering, densification behavior, Microstructural studies, quantitative microstructural analysis and mechanical properties. Experiments were designed to study the effect of particle size, milling and microwave heating on densification behavior and Microstructural evolution. Experimental details of the present study are summarized in Table 3.1

#### **3.1. Powder characterization**

The characteristics of starting powders greatly affect the densification behavior during sintering. Establishing the relationship between the sintering behavior and the powder characteristics requires quantitative information regarding the particle size, particle size distribution, apparent density, particle morphology, flow rate and chemical composition. The W, Ni and Fe powders were subjected to the series of characterization tests. The characteristics of all of these powders are presented in Table 3.2. Descriptions of the standard techniques used to characterize the powders are described in the subsequent sections.

##### **3.1.1. Particle Size and Distribution**

A Laser Scattering Analyzer (model: Economy, Laser Klasse I; supplier Fritsch, Germany) was used for analyzing the particle size of the powders. Low angle Fraunhofer

**Table 3.1.** Experimental Details.

Compositions (wt%)	(i) 92.5W-6.3Ni-1.1Fe and (ii) 90W-7Ni-3Fe
Average tungsten Particle size	(i) 4 $\mu\text{m}$ and (ii) 9.5 $\mu\text{m}$
Preparation route: • Mixing  • Milling, 3 h.	30 min.  (i) Ball milling (ii) Attritor milling
Compaction pressure	200 MPa
Debiding/Pre-sintering ( $\text{H}_2$ atmosphere)	(i) 450°C (for cylindrical samples) (ii) 1000°C (for tensile samples)
Sintering temperature, time	(i) 1400°C, 1 h (ii) 1500°C, 1 h
Sintering atmosphere	Reducing ( $\text{H}_2$ )
Post sintering treatment	1000°C, 15 min., Argon atmosphere (only for tensile samples)

**Table 3.2.** Powder characteristics of as-received elemental powders.

Characteristics		W (fine)	W (coarse)	Ni	Fe
Apparent Density, $\text{g/cm}^3$ (% theoretical)		5.2 (27)	5.3 (28)	2.7 (30.3)	3.8 (48.9)
Flow Rate (s/50g)		3.25	3	Non flowing	5.5
Particle size, $\mu\text{m}$	$D_{10}$	2.0	4.5	3.8	1.4
	$D_{50}$	4.2	9.5	11.0	7.0
	$D_{90}$	6.2	29.4	31.8	19.0

light scattering using monochromatic (laser) light and dispersed particles were used in this case. The particles were suspended in a suspension made using 2 to 3 g of powder dissolved in approximately 60 ml of distilled water with 10% sodium meta-phosphate. The particles were passed through a laser beam in a circulating water stream. The light scattered after interaction with the particles were measured by detectors, which are placed strategically. The size of the particles affects both the intensity and angular extent of scattering. With the coherent light scattering angle varies inversely with the particle diameter. The scattering depends on the refractive index of the particle in the suspension medium, wavelength of light and particle size and shape. Table 3.2 shows the size distribution of tungsten (fine and coarse), nickel and iron powders.

### **3.1.2. Particle Morphology**

The tungsten powder was produced by the reduction of ammonium paratungstate. This process produces irregular hexagonal or octagonal powders. The nickel powder prepared by carbonyl process was supplied by INCO and had spherical but spiky appearance. Whereas, the iron powder was of rounded shape. Micrographs of the powders showing the particle morphology were taken by JEOL, JSM-830A, scanning electron microscopy (SEM) in secondary electron (SE) mode. Figures 3.1 to 3.3 show the morphology of elemental powders used for present work.

### **3.1.3. Apparent Density and Flow Rate**

The apparent density of the powder gives a measure of the degree of packing of the powder in loose form. It is generally expressed as a fraction of the theoretical density. Apparent density for each powder is specified by the supplier. The flow rate of the powders

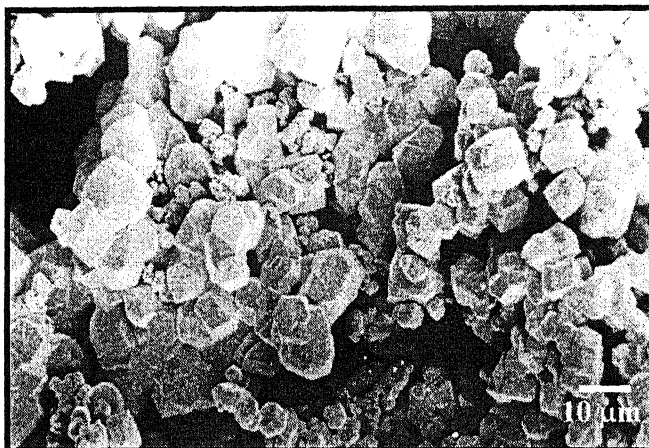


**Figure 3.1.** SEM micrograph of the as-received tungsten powder.

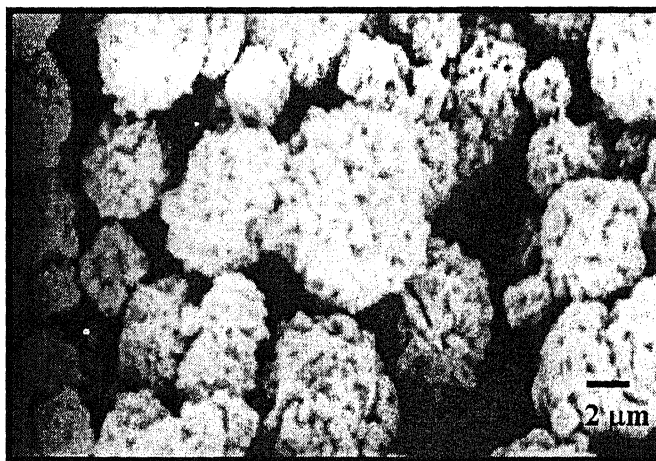


**Figure 3.2.** SEM micrograph the as-received of nickel

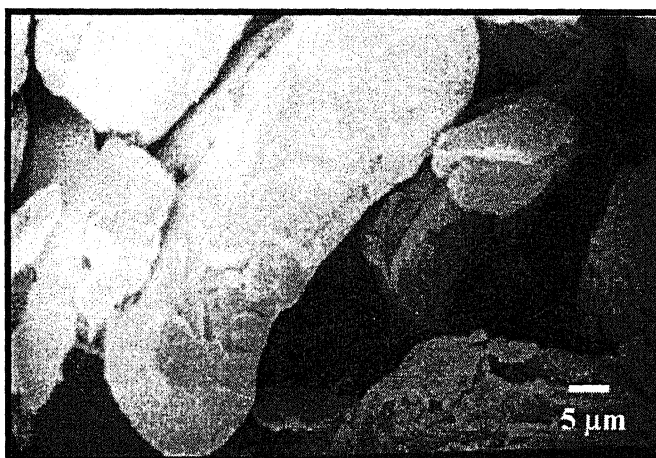


**Figure 3.3.** SEM micrograph of the as-received iron powder.

measured by the Hall flowmeter having an orifice of 2.54 mm in diameter. The technique is based on the MPIF standard 3 [63]. The flow rate is defined as the time taken 50 g of powder to flow through the Hall flowmeter funnel of specific orifice.

### **Powder Preparation**

For the present study, two different compositions, namely, 92.5W-6.4Ni-1.1Fe and V-7Ni-3Fe (all wt%) prepared using both fine as well as coarse tungsten powders. The densification behavior of heavy alloy systems is greatly sensitive to the powder preparation technique. Greater initial homogeneity improves the sintering behavior. If the elemental powders are blended together and the binder (Ni or Fe) particle size is much larger than the size of W powder, then the chances of liquid pool formation are more. So, this method is not effective for densification [64]. A more effective method for producing a homogeneous mixture is milling i.e. ball milling and attritor milling. As the former composition is prepared for microwave sintering, so milling is done only for the latter composition.

#### **3.1. Powder Mixing**

A simple method of preparing a powder mixture is to blend elemental powders. Elemental powders taken in the desired weight fraction were mixed in Turbula Mixer (type: C, supplier: Bachofen AG, Switzerland). Mixing was done for 30 min for both the compositions with different powder sizes. Mixing ensures complete homogeneity in the mixture. To prevent agglomeration, adequate care should be taken that the powders were not shaken after mixing.

The densities of the W-Ni-Fe alloys were determined using the inverse rule of mixture. The theoretical density can be expressed as:

$$\frac{1}{\rho_{th}} = \frac{w_w}{\rho_w} + \frac{w_{Ni}}{\rho_{Ni}} + \frac{w_{Fe}}{\rho_{Fe}} \quad \dots\dots\dots (3.1)$$

here  $w_w$ ,  $w_{Ni}$ , and  $w_{Fe}$  are the weight fractions of the different powders to be mixed and  $\rho_w$ ,  $\rho_{Ni}$ , and  $\rho_{Fe}$  are the densities of individual components.  $\rho_{th}$  is the theoretical density of the mixture. This simple formula however assumes that the individual components do not interact with each other.

for 90W-7Ni-3Fe composition:

$$\frac{1}{\rho_{th}} = \frac{0.9}{19.3} + \frac{0.07}{8.9} + \frac{.03}{7.8}$$

$$\rho_{th} = 17.6 \text{ g/cm}^3$$

similarly, the theoretical density of 92.5W-6.3Ni-1.1Fe:

$$\rho_{th} = 17.7 \text{ g/cm}^3$$

### 3.2.2. Ball Milling

The powders were planetary ball milled in a hardened stainless steel container using tungsten carbide balls. Figure 3.4 shows the ball mill used for the present study. The ball to powder ratio (by weight) were taken 10:1 and  $2/3^{\text{rd}}$  of container was filled with acetone, the milling media. Active addition of acetone removes the heat generated during the milling process and prevents oxidation of powders during milling. Milling was done for three hours. After milling the mixture was decanted to remove acetone as much as possible. The mixture was then passed through a 20 mesh sieve to separate the balls from the powder. The powder was then heated at approximately 60°C for complete evaporation of acetone in an oven.



### 2.3. Attritor Milling

Attritor milling is a mechanical alloying process in which ductile particles are deformed around harder, less ductile particles. The particles work harden, fracture and cold weld again. This continual process produces a fine, homogeneous composite powder. The particle size and distribution depend on several milling parameters, including speed, time and powder loading. In this study, attritor milling was performed for 3 h at a speed of 250 rpm using Union process 1-S Batch Attritor with mild steel arm, tank and balls as shown in figure 3.5. Acetone was added to reduce oxidation. The relatively short attritor milling time and low speed result in minimal mechanical alloying while still producing a homogeneous powder mixture.

### 3. Compaction

Sintering studies were conducted on cylindrical specimens. The mixed and milled powders were compacted at 200 MPa into cylinders of 12.75 mm in diameter and approximately 5 mm high using a semi-automatic hydraulic press (Model: CTM 50, supplier: FIE Pvt. Ltd., Ichalkaranji, India) of 50T capacity. The dies were made of high chromium high carbon steel for making all the cylindrical compacts. The dies were cleaned with acetone before compaction to remove any traces of dirt or grease. Zinc-stearate was used as die wall lubricant in powder and spray form during compaction, which facilitated compaction and subsequent removal of compacted samples. Die wall lubricants usually do not work satisfactorily and resulted in delamination of milled powders. Therefore solid lubricants are being admixed to the metal powder [65]. For consolidation of milled powders 2 wt% acrawax was used as lubricant for cylindrical samples.

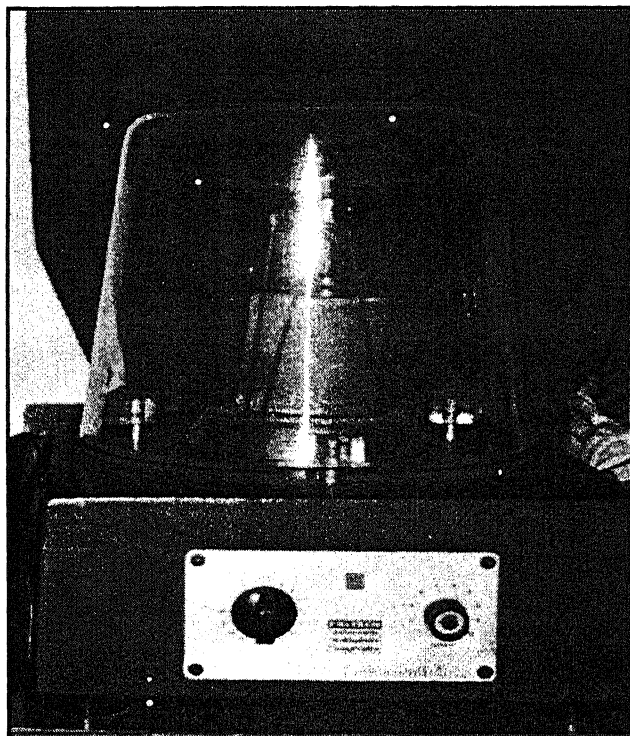


**Figure 3.4.** Ball mill used for the present study.

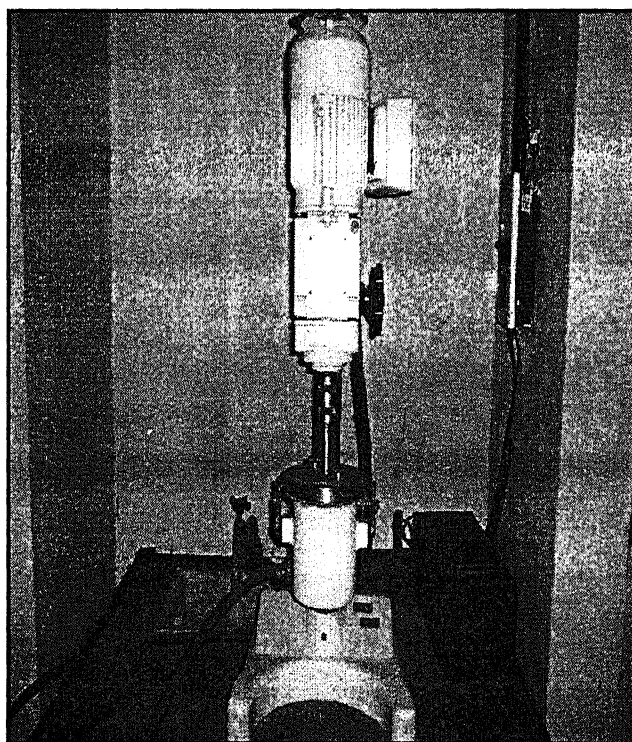


**Figure 3.5.** Attritor mill used for the present study.

## Sintering

### 1. Debinding/Pre-sintering

Debinding/Pre-sintering of green compacts having acrawax was carried out in a similar type, SiC-heated horizontal furnace (rating 1.5 kVA). The tube of the furnace was made up of doubly recrystallized alumina with an inner diameter of 38 mm and length of 1170 mm. The furnace possessed a heating zone approximately 105 mm, with a capacity to operate in 1500°C with an accuracy of  $\pm 3^\circ\text{C}$ . The atmosphere used for debinding was reducing (hydrogen, dew point  $-35^\circ\text{C}$ ), to prevent the samples from oxidation. The debinding was carried out at 450°C for 1 h. The green samples were placed inside the furnace by means of an alumina boat. The alumina boat was used because it possesses higher melting point and does not contaminate samples. It also prevents sticking of samples after sintering. Both the ends of the alumina tube were sealed using adhesive/sealant to prevent leakage of hydrogen during sintering. The heating rate was maintained at 5°C/min for all the samples. An automatic temperature controller was used to monitor the temperature. After soaking for 1 h at desired temperatures, all the samples were furnace cooled. Hydrogen atmosphere was maintained up to 200°C during cooling to prevent oxidation.

### 2. Conventional Sintering

Sintering of green/debound samples was carried out in a MoSi<sub>2</sub> heated, automatic programmable tubular furnace (Model: OKAY 70T4, Supplier: Bysakh & Co., Kolkata, India). The photograph and schematic diagram of the tubular furnace is shown in Figure 1. The tube of this furnace was also made of doubly recrystallized alumina with inner diameter of 90 mm and length 1170 mm. This furnace possessed a heating zone

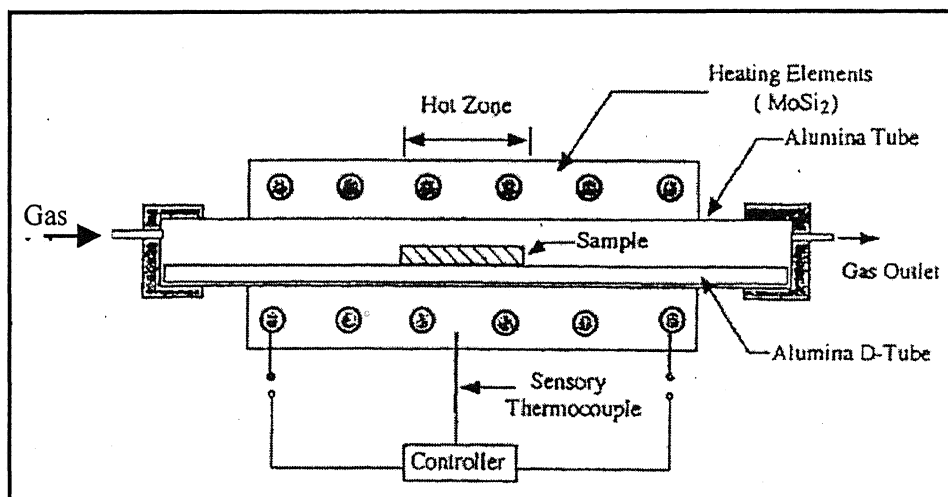
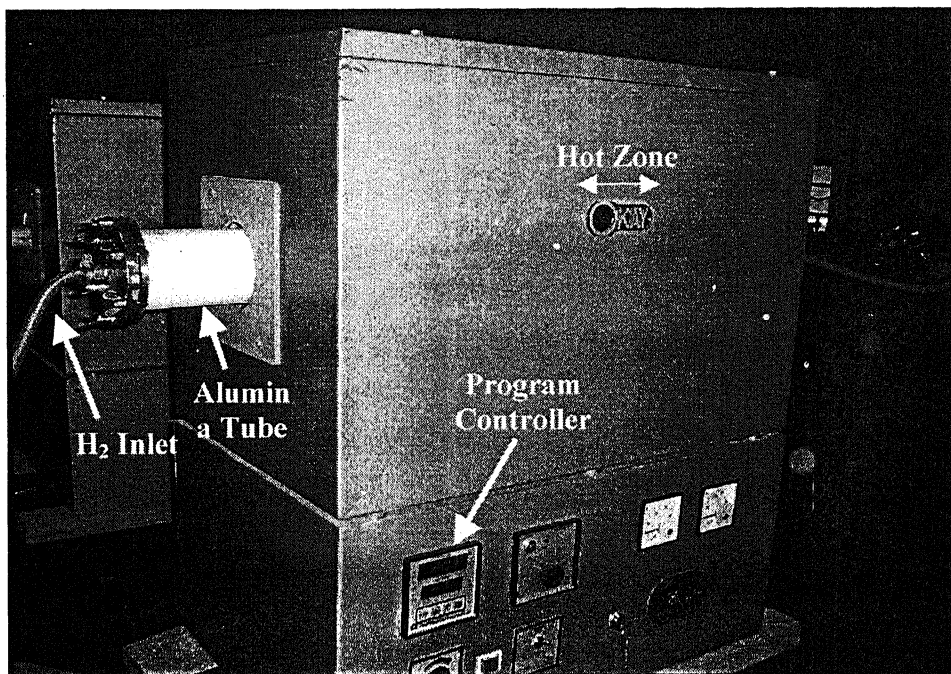


**Figure 3.6.** MoSi<sub>2</sub> heated horizontal tubular furnace with Schematic diagram.

proximately 300 mm, with a capacity to attain 1700°C with an accuracy of  $\pm 3^\circ\text{C}$ . Sintering was carried out at two different temperatures, namely 1400°C and 1500°C corresponding to solid state and liquid phase sintering, respectively. Reducing atmosphere is maintained with the help of commercially pure dry hydrogen (dew point,  $-35^\circ\text{C}$ ). The gas was passed through a catalytic dryer (silica gel) to remove any traces of moisture present in the gas. Figure 3.7 shows the sintering cycle followed for solid-state and liquid phase sintering. Samples were heated to required temperature after holding at 1000°C for 1 hour. This soaking was done to attain temperature homogenization in the sample and to provide enough time for reduction of oxide layer formed on the powder particles. The samples were allowed to cool in the furnace itself and the hydrogen atmosphere was maintained up to 200°C to prevent oxidation during cooling.

#### 4.3. Microwave Sintering

In another set of experiment a 1.1 kW commercial microwave furnace (Model: Interwave, Supplier: BHEL, Corporate R&D, Hyderabad, India) with a 2.45 GHz multi-mode cavity was used to sinter the 92.5W-6.4Ni-1.1Fe as pressed sample in  $\text{H}_2$  atmosphere. Figure 3.8 shows the photograph and schematic diagram of the microwave furnace used for the present study. The soaking time given at the sintering temperature was 20 min. A high density alumina tube of 71 mm in diameter and 670 mm in length was positioned at the centre of the furnace by drilling holes on side faces, projecting outward on both the sides. The compacts were placed in insulating fiberboard caskets. In order to improve the heat transfer at low temperature susceptor of SiC is introduced; its relatively high losses facilitate good coupling of matter with the microwave field. Three mechanisms are

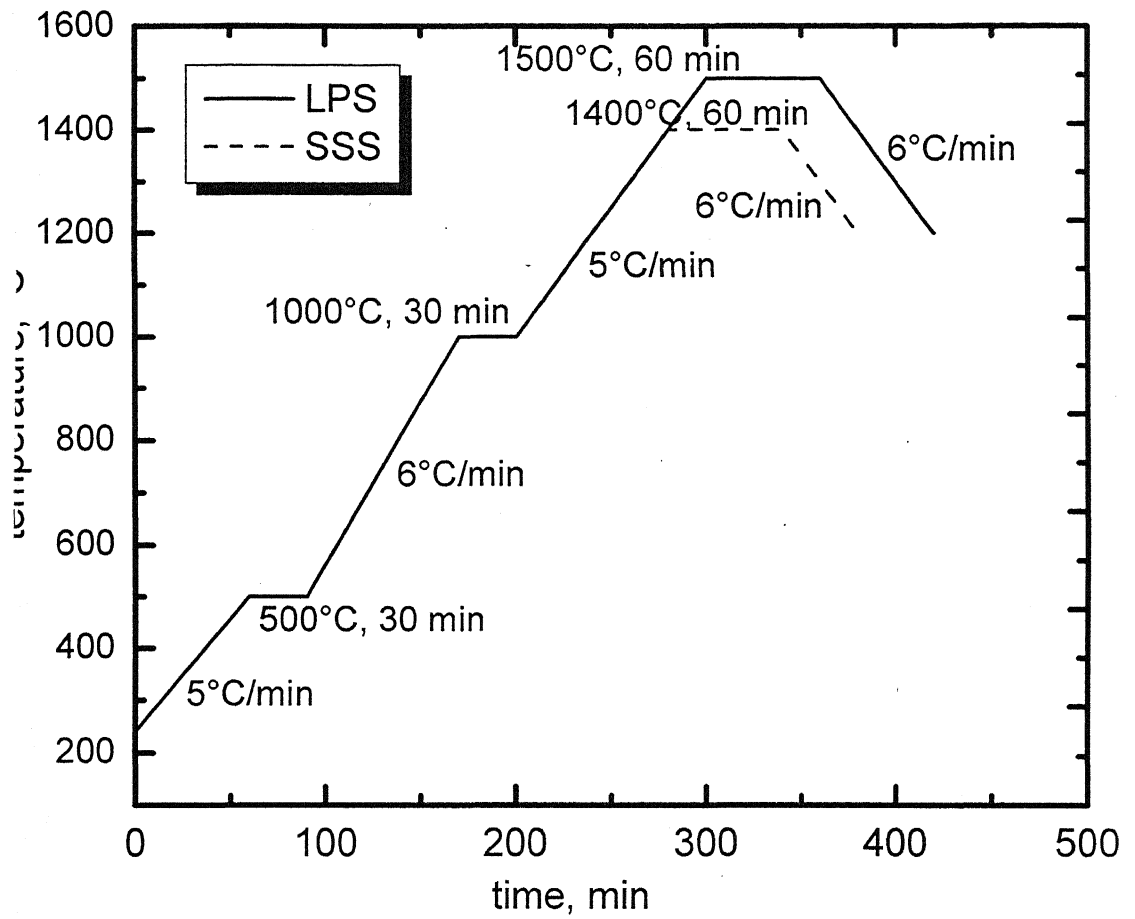


**Figure 3.7.** Sintering cycles followed for solid-state and liquid phase sintering.

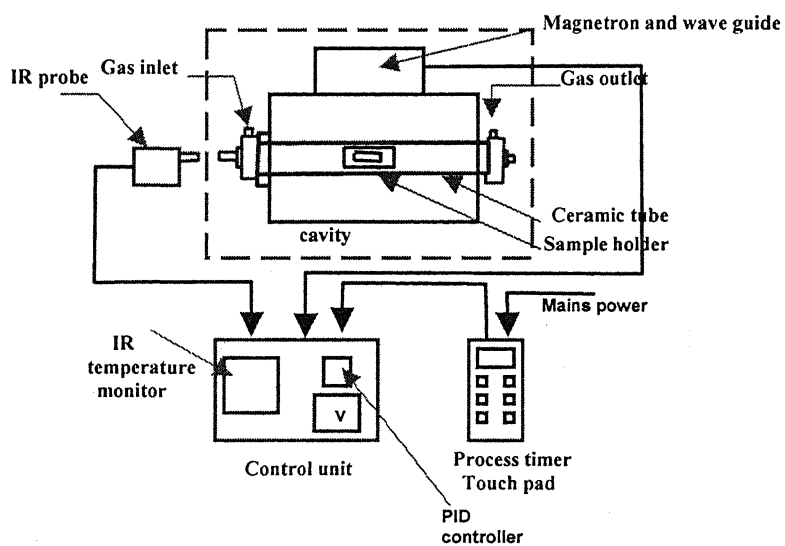
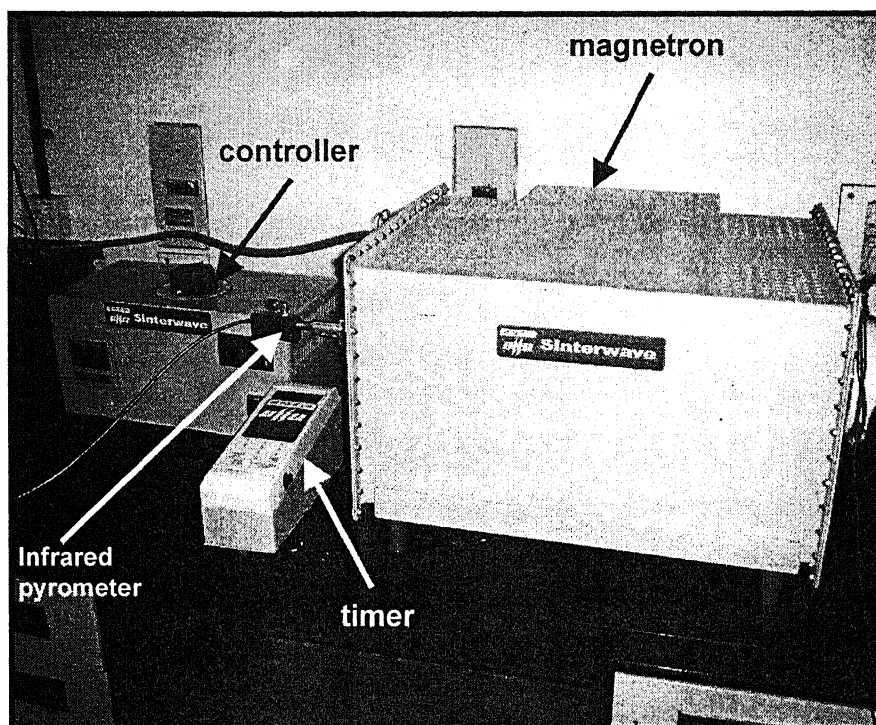


**Figure 3.8.** Microwave furnace with schematic diagram

considered in energy flow process: microwave absorption due to losses, black body radiation and heat convection. An insulation package made of Fibrefrax™ boards was used to surround the tube at the centre of cavity to prevent heat dissipation. Unlike conventional sintering thermocouple cannot be used to measure temperatures in microwave furnaces; instead we use infrared pyrometer (Mikron M680) to monitor the sample temperature. The infrared pyrometer was coupled with data acquisition and display software on a personal computer.

In the microwave furnace an electronic tube called magnetron is used to produce the microwaves. The magnetron, basically, converts 60 Hz power line electric current to an electromagnetic radiation of 2450 MHz. The high voltage (typically 3000 to 4000 volts) which powers the magnetron tube is produced by a step-up transformer rectifier and filter which converts 120 V AC to 4 kV DC. The microwave then passes through a wave guide into the metal cavity where they are reflected around the oven walls. Uneven reflections may cause localized hot and cold spots in the material. This is minimized by the use of a mode stirring fan and rotating carousel. The microwaves penetrate material and cause molecules within the material to vibrate at a frequency of the microwaves (2450 MHz). The vibration causes considerable molecular friction which produces heat and results in a rapid rise in temperature. The rate of heating depends on moisture content, shape, volume and mass of material present. A typical thermal profile followed for microwave sintering of 90W-7Ni-3Fe is shown in Figure 3.9. Microwaves do not directly heat the furnace walls and sample holders because they do not absorb microwave energy. However, they frequently get very warm from direct contact with the hot specimen.



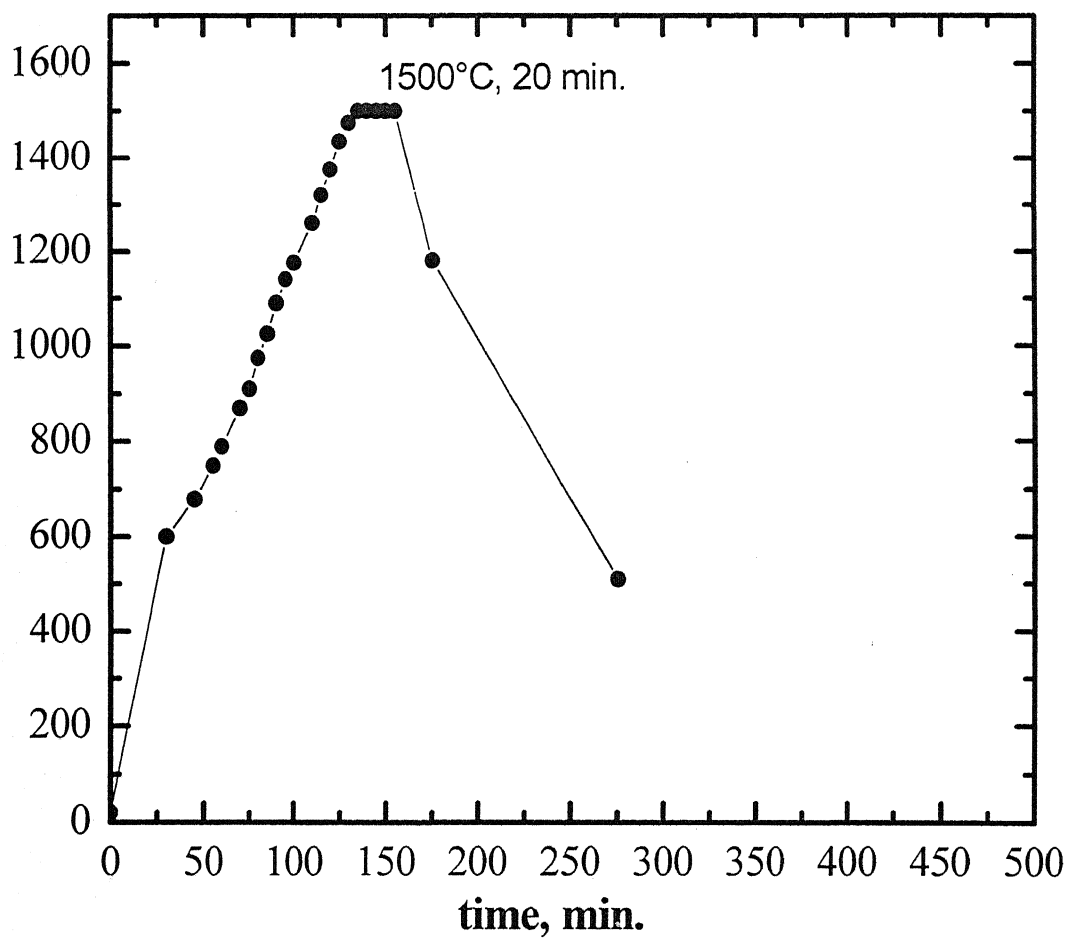


**Figure 3.9.** Sintering cycles followed for microwave sintering of WHA. The compacts were sintered at 1500°C for 20 min.

### 3.5. Densification Behavior (Sintered Density and Densification Parameter)

The densities of cylindrical green compacts and sintered compacts were quantified by weighing and dimensional measurements. Generally, green densities of the compacts were calculated using physical dimensions and their masses. An analytical balance (Model: AG245, Supplier: Mettler Toledo, Switzerland) and a digital caliper were used for all the measurements.

Densification parameter ( $\Psi$ ) was also calculated for both samples, to normalize the densification behavior, by the equation given below

$$\Psi = \frac{\rho_s - \rho_g}{\rho_{th} - \rho_g} \dots\dots\dots (3.2)$$

where,  $\rho_g$ ,  $\rho_s$ , and  $\rho_{th}$  are green density, sintered density and theoretical density, respectively.

## 3.6. Quantitative Metallography

### 3.6.1. Sample Preparation

Standard metallographic practices were employed for preparing samples for microstructural examinations [66]. All sintered samples were sectioned longitudinally and mounted. Utmost care was taken while mounting in order to maintain good gripping of the samples within the mount and flatness. Grinding was next step to further flatten the surface and making polishing easier. All samples were then polished manually on a polisher (Model: Lunn Major, Supplier: Struers, Denmark) having four grades of emery papers 1/0, 0, 3/0 and 4/0 in order, followed by fine wheel polishing with 0.05  $\mu\text{m}$  size alumina

suspended in distilled water. This is attributed to the fact that the emery paper quickly grinds away the soft Ni-Fe matrix phase but the hard tungsten particles.

### 3.6.2. Microstructural Studies

Since tungsten heavy alloys have enough contrast in micrographs without etching, so all the optical micrographs were taken in unetched condition. The average tungsten spheroid size, volume fraction of the matrix, dihedral angle, contiguity and connectivity were characterized by microstructural analysis by an image analyzer (Model: Laborlux12MES, Supplier: Lietz, Germany).

#### 3.6.2.1. Volume Fraction of Matrix

Systematic point count method was used to evaluate the volume fraction of the matrix of the samples [67] as per the ASTM standard. In point count analysis, a square grid with 25 grid points as shown in Figure 3.10, was superimposed on the microstructure. By finding the ratio of intersections falling on a particular phase with total number of intersections, volume fraction of that particular phase can be calculated. If total number of grid points falling on the phase of interest is  $P_i$  and total number of grid points is  $P_a$ , then the point fraction  $P_p$  is given by

$$P_p = \frac{P_i}{P_a} \dots\dots\dots (3.3)$$

To ensure the reproducibility of the result, the same procedure was repeated in 30 different fields of views of the same sample, and mean was considered as final result. The advantage of using systematic point count analysis is that the relative error is low (< 10%) as compared to other methods.

### 3.6.2.2. Contiguity ( $C_g$ ) and Connectivity ( $C_c$ )

The contiguity is a microstructural measure that quantifies the relative interface area of solid-solid contacts versus the total interface area in the liquid phase sintered material. It is expressed mathematically by the well-known formula [68]

$$C_{ww} = \frac{2N_{ww}}{2N_{ww} + N_{wm}} \dots\dots\dots (3.4)$$

where,  $N_{ww}$  is the number of tungsten-tungsten contacts per unit length of any given intercept,  $N_{wm}$  is the number of tungsten-matrix contacts per unit length of given intercept (Figure 3.11). The same calculation was done on 30 fields of view of a particular alloy of interest, and mean was taken as contiguity of that particular alloy. Contiguity varies between 0 and 1. A value '0' indicates that there is no W-W contact and a value '1' implies 100% contiguous structure.

Connectivity ( $C_c$ ) is the two-dimensional grain co-ordination number in a liquid phase microstructure (Figure 3.12) and is measured by counting the number of nearest touching grains for 200 chosen central grains in a micrograph; and mean was taken as connectivity [69]. It is a measure of rigidity of the microstructure and has a positive correlation with the contiguity.

### 3.6.2.3. Dihedral Angle, ( $\phi$ )

The angle formed by the two contacting solid-solid grains in liquid phase sintered microstructure is termed as dihedral angle. A dihedral angle is shown in Figure 3.12. It provides the balance between solid-solid and solid-liquid interfacial energy. Absolute measurement of interfacial energy is quite difficult. The true dihedral angle cannot be measured by the 2-D microstructures. However, Riegger and Dehoff [70] showed that the

mean dihedral angle measured on a 2-D micrograph is the best estimate of true dihedral angle. Dihedral angle calculation was done manually by measuring the angle between two connecting grains using a protractor on a micrograph. The same procedure is repeated for approximately 200 grains.

#### 3.6.2.4. Surface Area per unit Volume ( $S_v$ )

Surface area per unit volume of the W-W and W-Matrix interfaces was calculated using a series of lines of equal length. The total number of intersection points with the solid-solid (W-W) contact and solid-liquid (W-Matrix) was calculated for 30 fields of view shown in Figure 3.10. Finally, this produced the points per unit length ( $P_L$ ). then  $S_v$  was calculated as

$$S_v = 2P_L \dots\dots\dots (3.5)$$

where,  $L$  = Length of line in terms of  $\mu\text{m}$  varies depending upon the magnification.

#### 3.6.2.5. Mean Grain Size

Grain size calculation was done by equation 3.6 [71].

$$G = \frac{4V_W}{S_{WW} + S_{WM}} \dots\dots\dots (3.6)$$

Where,  $G$  is the grain size,  $V_W$  is volume fraction of tungsten in observed microstructure,  $S_{WW}$  is interfacial area of tungsten/tungsten grains per unit volume, and  $S_{WM}$  is interfacial area of tungsten/matrix per unit volume (Figure 3.10).

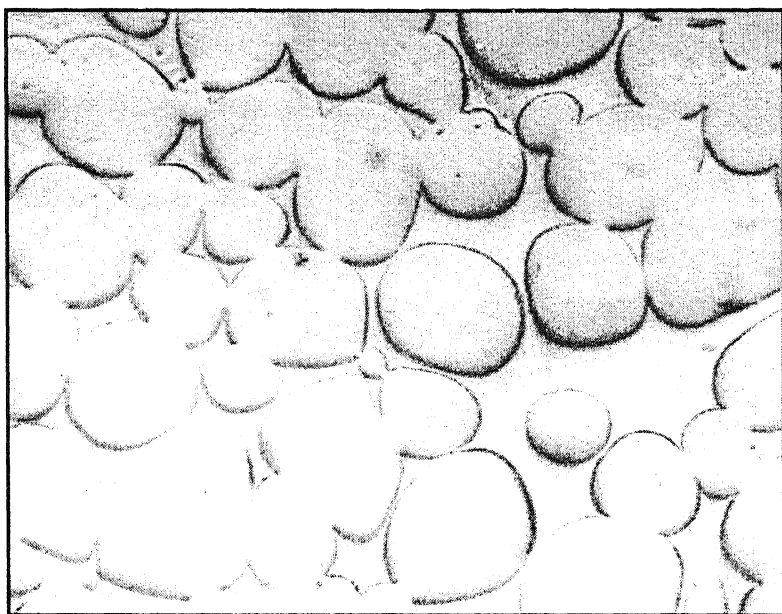


**Figure 3.10.** Superimposing grid on a micrograph for calculation of volume fraction of a particular phase of interest.

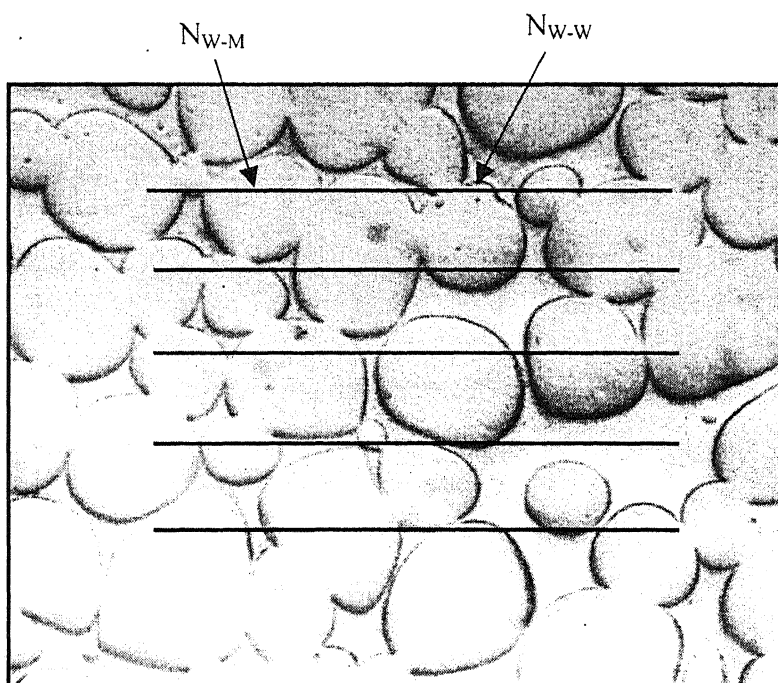


**Figure 3.11.** Contiguity measurement by superimposing parallel grid of lines on a micrograph.

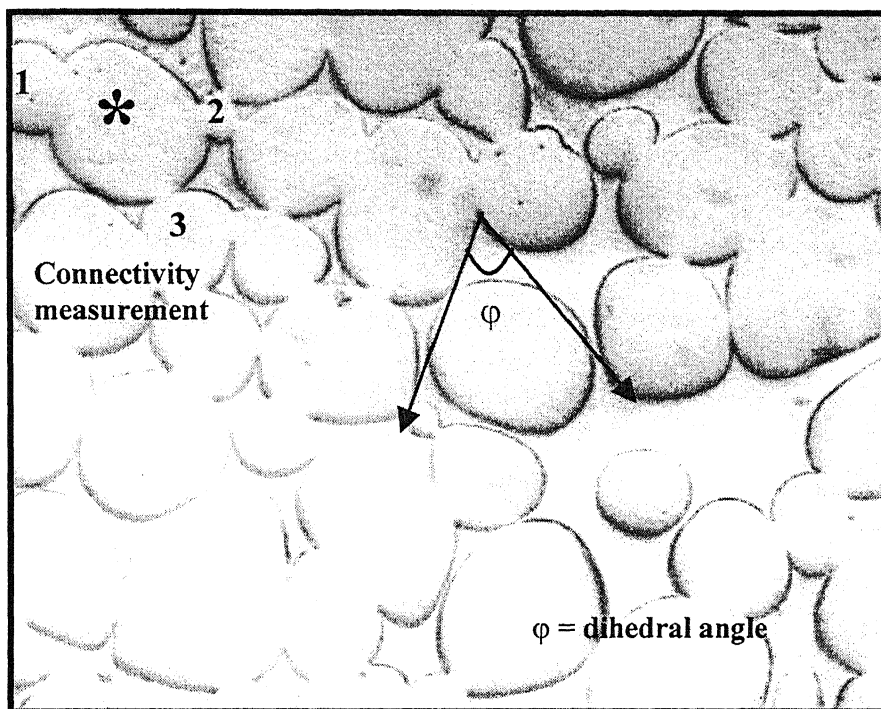


**Figure 3.12.** Connectivity and dihedral angle Measurement.

## **7. X-Ray Diffraction Analysis**

To study the elements present and formation of any intermetallic phase in the samples, XRD patterns of conventionally as well microwave sintered samples were taken with the help of X-Ray Diffractometer (Model: Rich. Seifert, GmbH, Germany). The obtained pattern is matched with the standard JCPDS files for each element and any intermetallics formed.

The experimental variables of the XRD are as follows:

scan rate -  $3^\circ/\text{min}$

target - Cu

power - 30kV x 20 mA.

range (CPM) – 20 K

time constant (s) - 3

## **8. Elemental analysis by EPMA**

The elemental analysis was performed using EPMA (JEOL JXA-8600SX Superprobe, Japan) equipped with WDS. The operating conditions for EPMA such as magnification (1000x), spot size (2  $\mu\text{m}$ ), probe current ( $5 \times 10^{-8}$  A) working distance, tilting angle and take off angle were all kept constant for all samples.

## **9. Mechanical Properties**

Bulk hardness, micro hardness and compressive strength measurements were done in the present study for conventionally sintered (mixed, ball milled and attritor milled) as well as microwave sintered samples.



### 3.9.1. Bulkhardness

Bulkhardness values of sintered compacts were measured by Vickers hardness tester (Model: LECO V-100-C1, Supplier: Akashi Corp., Japan) at 2 kg load. The load was applied for 15 s to get a square shaped indentation using a diamond pyramid indenter. The indentation observed under attached microscope and the length of diagonals of the square indentation was measured. The tester itself calibrated the Vickers Hardness (VHN) by using the value taken of diagonals. 5 indentations were made for each compact and the average value has been reported.

### 3.9.2. Microhardness

The microhardness tests were performed using a micro-hardness tester (Model: Leitz 8299, Supplier: Leitz Wetzlar, Germany). The test was performed on the tungsten grains and matrix phase. The load used for indentation was 5 g and 50 g for matrix and tungsten spheroid respectively. The load was applied for 15 s to get square shaped indentation. Diagonal length of square was measured by scale attached to the microscope. Hardness was obtained, directly from the chart given in manual for corresponding load and diagonal length.

### 3.9.3. Compression Test

The deformation behaviour of the samples was studied during compression testing as per ASTM E9 specification at a nominal strain rate of  $4.5 \times 10^{-3} \text{ s}^{-1}$  using compression test machine (model: 810, supplier: MTS, UK), which had a maximum load capacity of 200 kN. None of the samples show fracture during compaction. For the latter, the initial and

ial dimensions were measured with the help of calliper and the % change in dimensions is calculated for each sample. The microstructures of the samples deformed were studied know the effect of deformation load on the grains as well as matrix phase.

## Chapter 4

### RESULTS AND DISCUSSIONS

The present chapter is divided into four sections. The first section describes the effect of sintering temperature and milling on densification behavior and microstructural evolution of tungsten heavy alloys. The second section aims at investigating the densification response, microstructural evolution and mechanical properties of microwave sintered WHA and compare those obtained via conventional sintering.

#### 4.1. Particle Size and Size Distribution

The results of particle size and size distribution analysis of mixed, ball milled and attritor milled powders are summarized in Table 4.1. It is clear from the Table 4.1 that average particle size is reduced due to milling. In case of attritor milling average particle size was least. In case of mixed powder the range of particle size was very wide, but after milling range became narrower. XRD analysis confirms that the milling reduces the average particle size. Figure 4.1 shows the XRD pattern of the mixed and milled tungsten powder samples. Attritor milled sample is showing the maximum line broadening for both coarse and fine tungsten powders which indicates the highest amount of effective milling. There is a little shifting of approximately  $2^\circ$  (corresponding lattice parameter change  $\sim 0.18 \text{ \AA}$ ) in case of ball milled sample. Cullity [72] has reported that up to a shift of  $0.02 \text{ \AA}$  in lattice parameter ( $d$ ) can be discarded.

**Table 4.1.** Particle size analysis of mixed, ball milled and attritor milled powders.

Compositions		Average Particle Size ( $\mu\text{m}$ )		
		Mixed	Ball Milled	Attritor Milled
<b>90W (fine)-7Ni-3Fe</b>	D <sub>10</sub>	3.7	2.4	1.8
	D <sub>50</sub>	7.9	7.1	6.3
	D <sub>90</sub>	16	11.3	8.8
<b>90W (coarse)-7Ni-3Fe</b>	D <sub>10</sub>	8.5	6.7	4.1
	D <sub>50</sub>	24.2	16.1	10.8
	D <sub>90</sub>	29.9	21.7	12.9

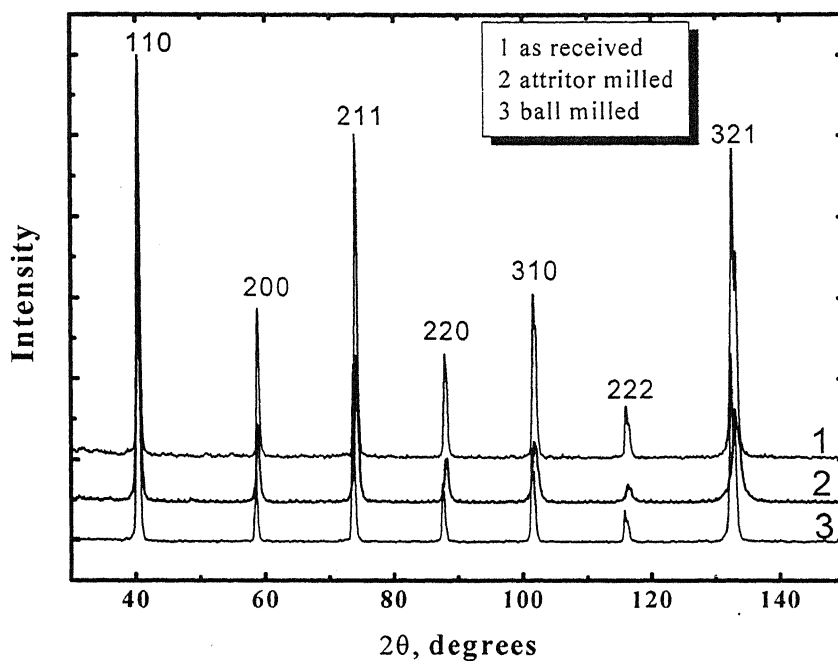


Figure 4.1a. XRD patterns of fine tungsten powder.

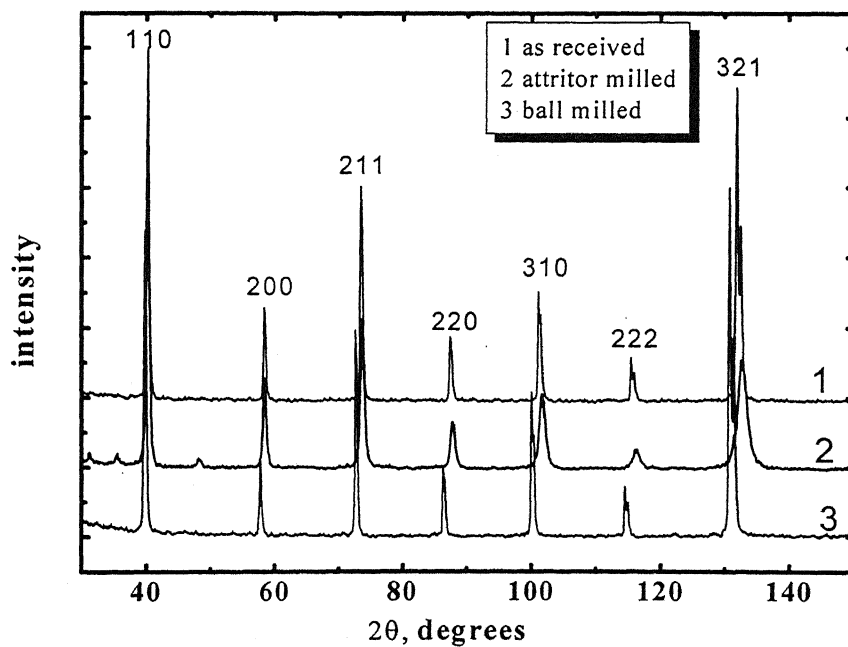


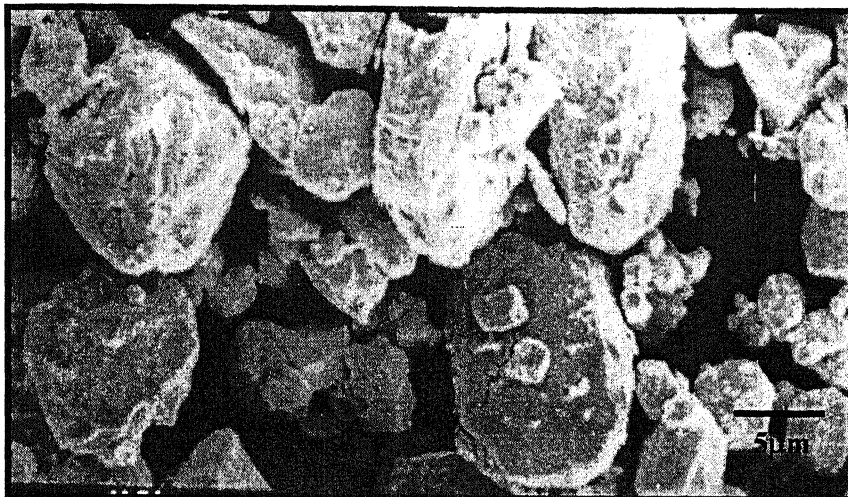
Figure 4.1b. XRD patterns of coarse tungsten powder.

Milled tungsten powder in both types of mill is shown in Figure 4.2. In case of planetary ball mill, the bowl fasteners attached to a supporting disc. During the grinding process, the grinding bowl and supporting disc rotate in opposite directions, so that two different centrifugal forces act simultaneously on the powder, alternating between similar and opposite with respect to the rotation direction. Hence, the powder size is reduced as a result of both attrition and impact (Figure 4.2a) [32]. Attritor milling is high energy milling process and it is clear from Figure 4.2b that in this type of milling the degree of deformation is higher than ball milling.

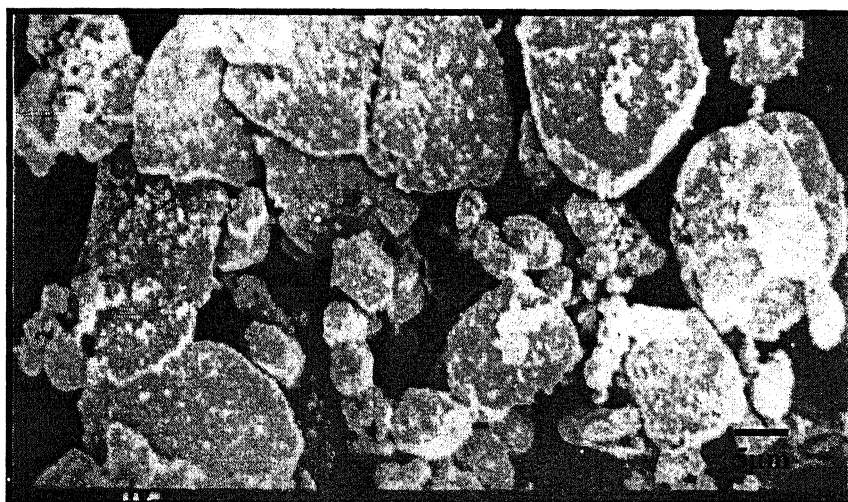
Milling results in a narrow particle size distribution, because the particles larger than average size are reduced at the same rate as that of the fragments smaller than average grow through accretion of smaller particles and wear debris produced by attrition. As it is clear from Figures 3.1 to 3.3 that elemental powders used for present study have their distinct morphology. In the mixed form the all three powders retained their morphology as shown in Figure 4.3a. It was observed that due to milling fragmentation and proper mixing of these powders occurred, and it was difficult to distinguish them on the basis of their distinct morphology. Figures 4.3b and 4.3c show the scanning electron micrographs of ball milled and attritor milled powders, respectively.

In the initial micro-forging stage particles are deformed in the absence of agglomeration by welding and fracture. Eventually, particles becomes so severely deformed and embrittled by cold work that they enter in secondary stage, during which the particles fracture by a fatigue failure mechanism and/or by the fragmentation of fragile flakes [73].

As the particle size becomes finer, agglomerating forces tend to become greater, and the agglomerates become stronger. In the later stage, milling forces that deagglomerate the particles reach equilibrium with agglomerating forces present. After this, tendency to



(a)



(b)

**Figure 4.2.** Scanning electron micrograph of (a) ball milled and (b) attritor milled tungsten powder

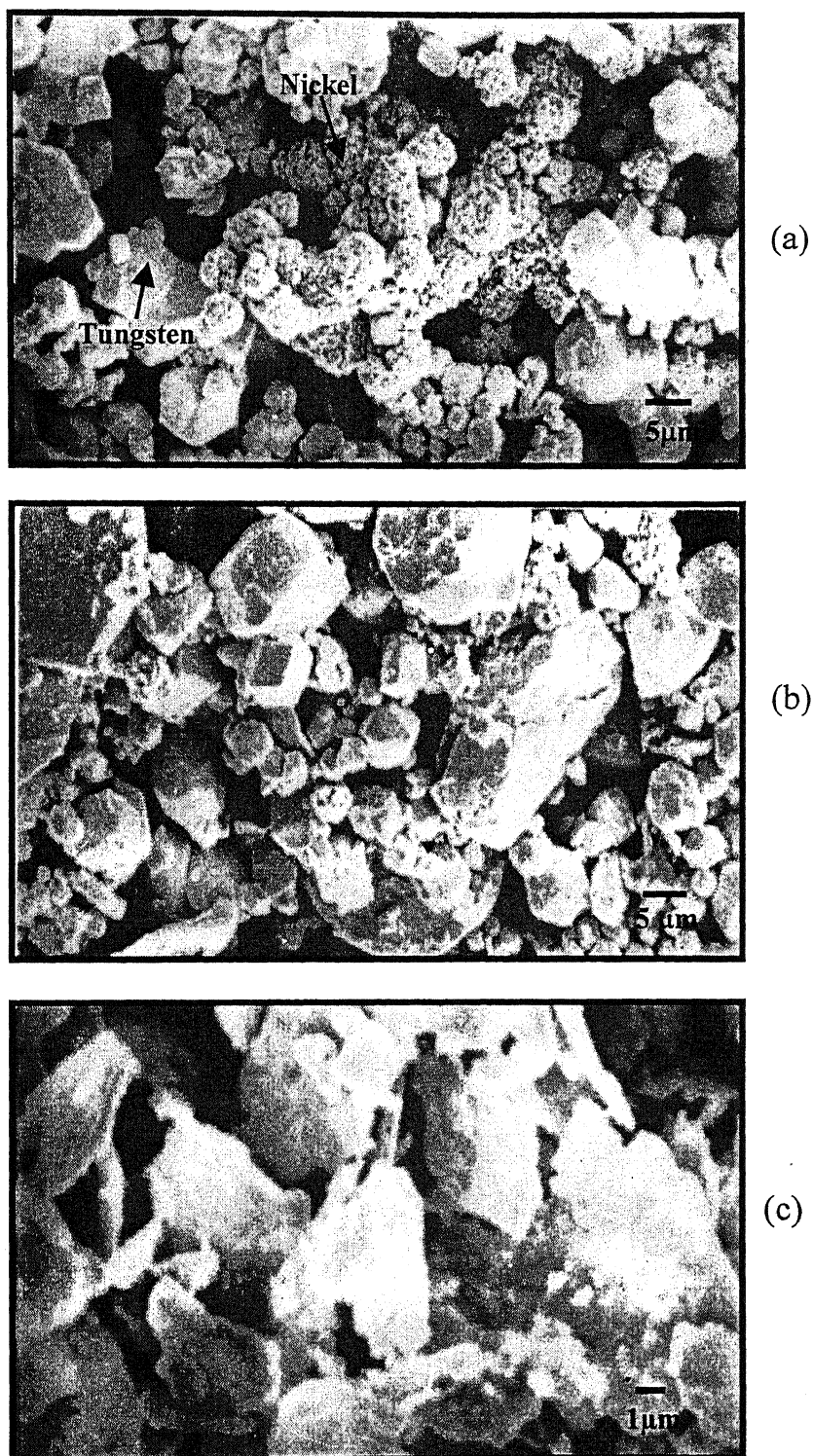


**Figure 4.3:** Micrographs of 90W (coarse)-7Ni-3Fe alloy in (a) mixed (b) ball milled and (c) attritor milled condition.



agglomerate increases and excessive milling may cause increase in particle size. That's why excessive milling should be avoided or surface active agents or lubricants should be used to nullify the forces of welding and thereby inhibit the agglomeration. For the present study, milling was done for 3 hours only, so no lubricants were used.

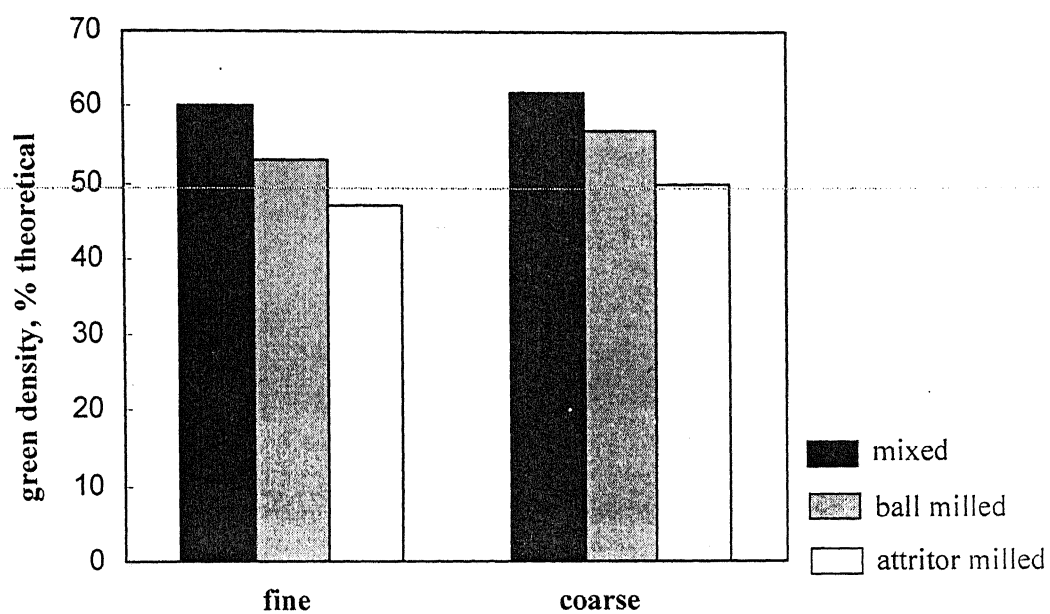
#### **4.2. Effect of Milling on Green Density**

Figure 4.4 shows the results of density calculations of green cylindrical samples prepared by mixed, ball milled and attritor milled powders. It was observed that samples prepared by finer powders, possess lower percentage theoretical density. It was also observed that the samples prepared by milled powders possess lower green density in comparison to samples prepared by mixed powders. In case of attritor milled powder, green density was observed the lowest.

With finer particle size, compaction becomes more difficult and the green density of samples reduces because, as the particle size decreases surface area increases. This cause an increase in inter-particle friction force during compaction and resists compaction. Milling causes narrower particle size distribution, due to which interstitial voids do not get filled up and compressibility of powders reduce.

#### **4.3. Density and Densification Parameter**

Figure 4.5 shows the comparison of sintered density achieved by solid-state sintering of mixed, ball milled and attritor milled powder compacts. Figure 4.6 shows the comparison of densification parameters of the same. It was observed that sintered density and densification parameter of solid-state sintered compacts was higher in case of milled



**Figure 4.4.** Effect of milling on green density of 90W-7Ni-3Fe alloy.

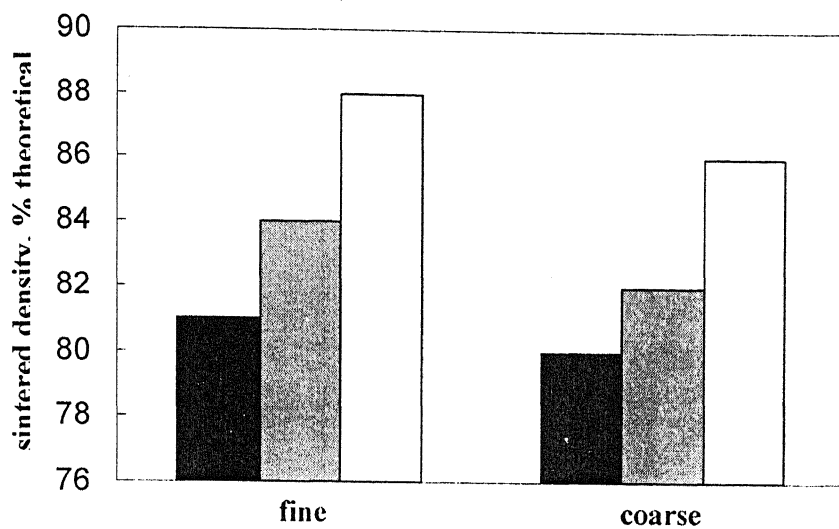


**Figure 4.5.** Comparison of percentage sintered density of solid state sintered mixed and milled powders.

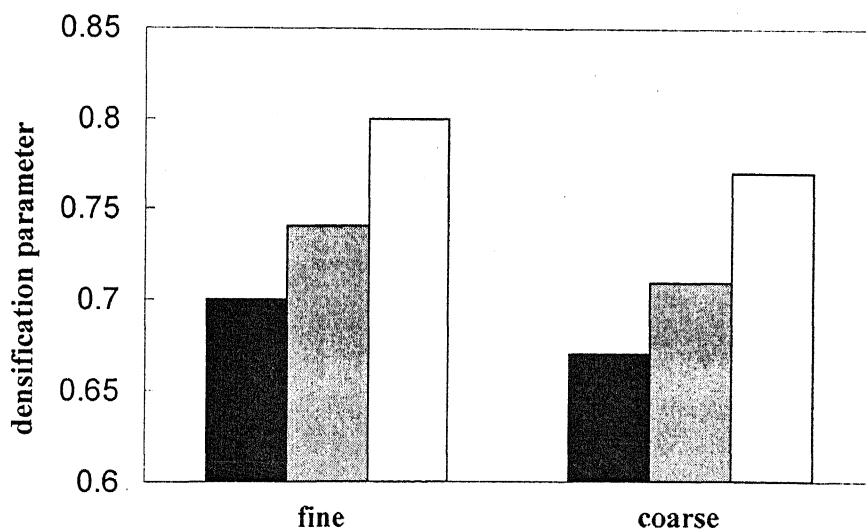
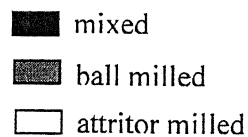


**Figure 4.6.** Comparison of densification parameter of solid state sintered mixed, and milled powders.



powders. Sintered density and densification parameter were highest in case of compacts prepared by attritor milled powders.

Figures 4.7 and 4.8 show the comparison of sintered density and densification parameters respectively, of liquid phase sintered compacts, prepared by mixed, ball milled and attritor milled powders. The result pattern was same, as it was in case of solid-state sintering but higher densification was achieved in case of liquid phase sintering.

In the solid-state sintering densification occurs mainly due to grain boundary diffusion. As the particle size decreases surface area per unit volume increases which results higher diffusion, so rate of sintering increases and higher densification can be achieved In case of milled powders. Milling causes high dislocation density, improved homogeneity, finer structure (laminar structure; initially brittle and ductile particles weld up and form laminar structure which further fragmented due to work hardening) and change in shape (flaky powders provide higher surface area per unit volume) which result in higher dislocation and surface diffusion, hence higher densification in solid state-sintering of milled powder.

The liquid phase sintering mechanism for W-Ni-Fe heavy alloys is through particle fragmentation, particle rearrangement and solution-reprecipitation. Liquid phase penetration along the interface boundaries is ensured because of the low dihedral angle between the binders and tungsten phase. Such penetration of liquid helps in enhanced solution-reprecipitation mechanism. The capillary pressure imposed by liquid phase, which pulls the solid particles towards each other is also responsible for initial densification by rearrangement. German [74] expressed the capillary pressure as:

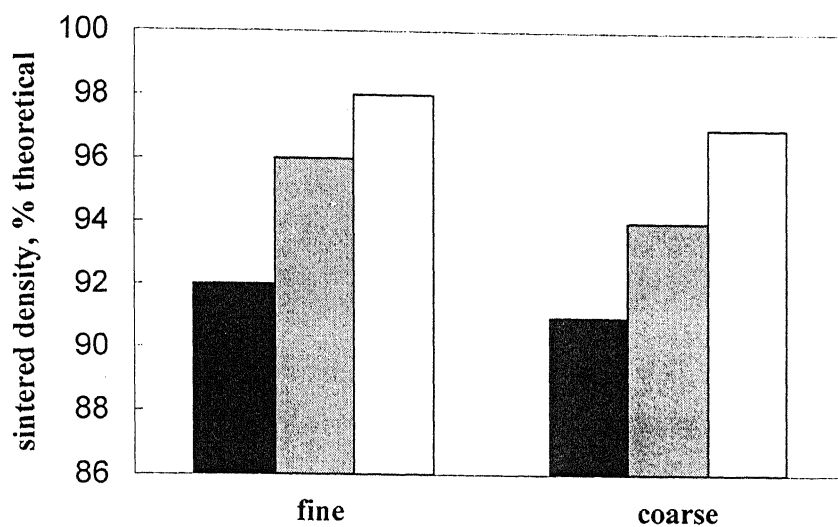


**Figure 4.7.** Comparison of sintered density of liquid phase sintered mixed, and milled powders.

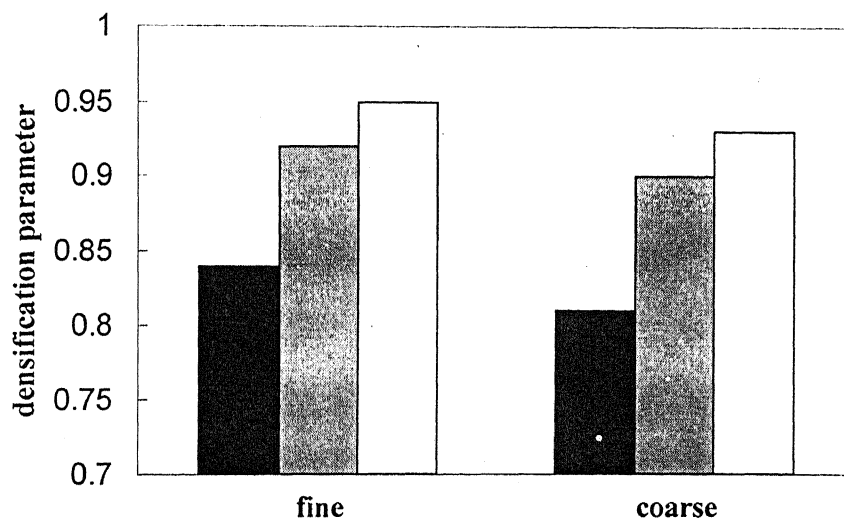
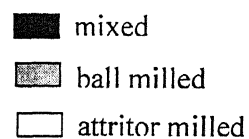


**Figure 4.8.** Comparison of densification parameter of liquid phase sintered mixed, and milled powders.



$$P_n = \frac{5.2\gamma_{LV}\cos\theta}{D(\Delta L/L_0)} \dots\dots\dots (4.1)$$

where  $P_n$  is the capillary pressure,  $D$  is the diameter of solid particles,  $\gamma_{LV}$  is the liquid/vapour surface energy,  $\theta$  is the solid/liquid/vapour wetting angle, and  $(\Delta L/L_0)$  is the linear sintering shrinkage given by the compact length change ( $\Delta L$ ) divided by the initial length ( $L_0$ ). As the  $(\Delta L/L_0)$  increases in the latter stage of sintering, capillary pressure decreases. Typical initial values for  $P_n$  are the order of a few MPa (for a  $\gamma_{LV}$  of  $2 \text{ Jm}^{-2}$  and particle size of  $100 \text{ }\mu\text{m}$ , the estimated capillary pressure goes from 10 to 1 MPa as the linear shrinkage goes from 0.01 to 0.1). For the finer particles capillary pressure will be higher. Since capillary pressure is inversely proportional to particle size reduction in particle size by 50% doubles the capillary pressure. Grain sliding and rearrangement occur rapidly in the very beginning of sintering, which enhance densification. During sintering dislocation density increases considerably in the contact region of particles. Capillary force is helpful to induce dislocations in the earlier stage at the contact region [75].

#### 4.4. Microstructural Evolution

Figures 4.9 and 4.10 shows the microstructures of solid state and liquid phase sintered 90W-7Ni-3Fe alloys respectively in different mixing and milling conditions. For milled samples, more homogeneous microstructure was observed than the mixed ones. It is clear from Figure 4.9 that pores are bigger in case of compacts prepared by mixed powders with compared to those, which are prepared by milled powders. In case of coarser particles, interstitial voids will be bigger. Since in solid-state sintering void removal occurs through

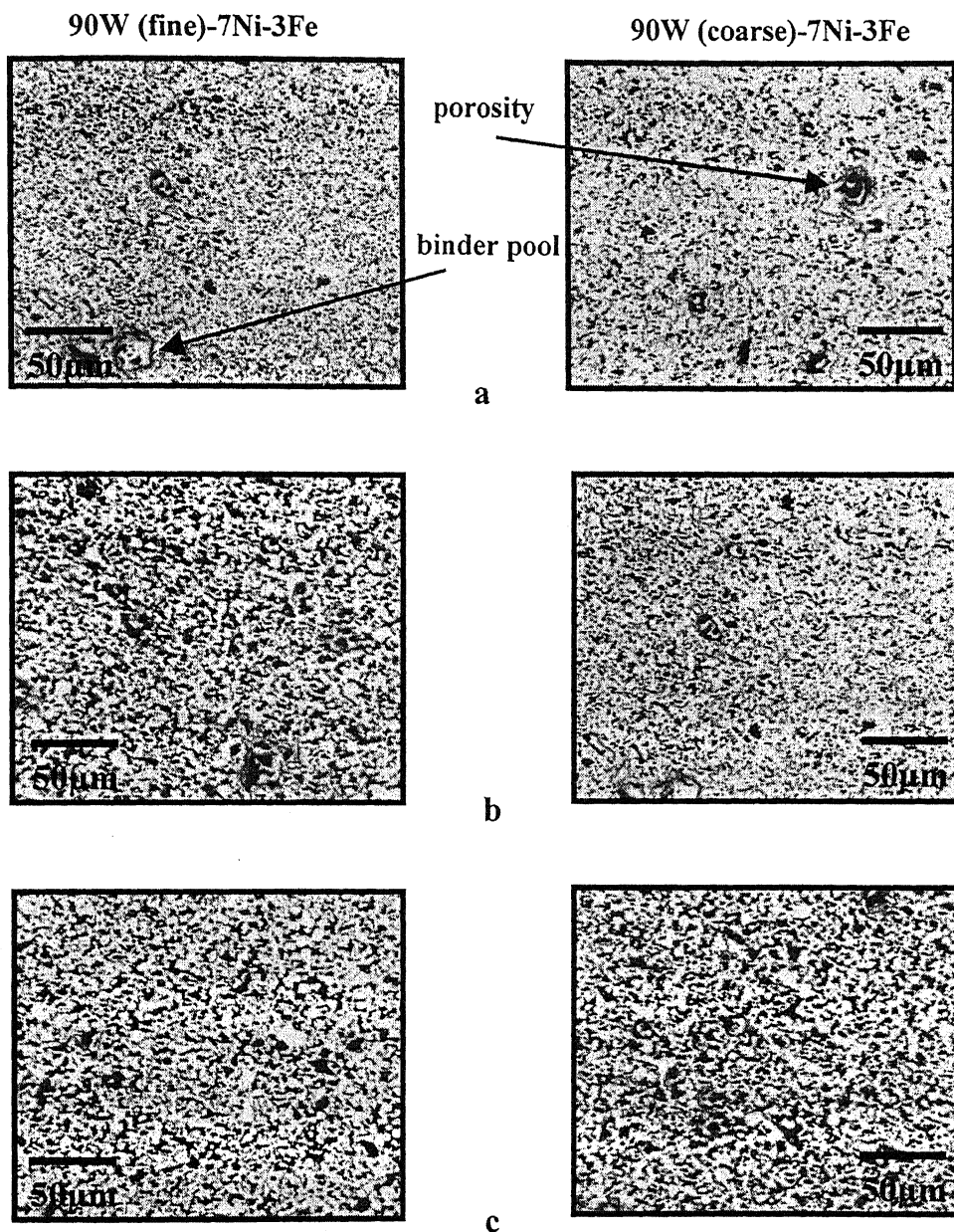


**Figure 4.9.** Microstructures of solid state sintered 90W-7Ni-3Fe alloy prepared by (a) mixed (b) ball milled and (c) attritor milled powders.

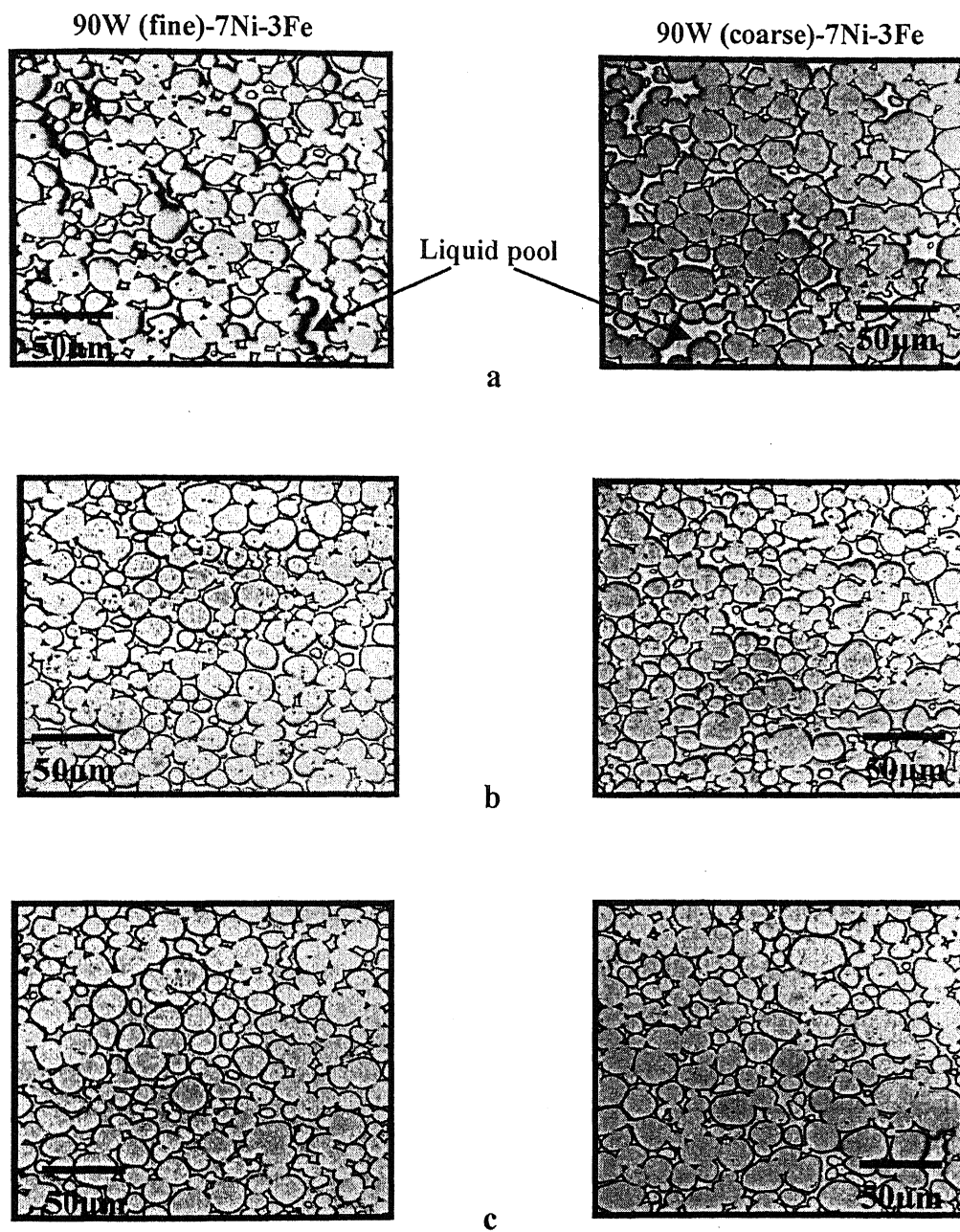


**Figure 4.10.** Microstructures of liquid phase sintered 90W-7Ni-3Fe alloy prepared by (a) mixed (b) ball milled and (c) attritor milled powders.



volume diffusion, which is very difficult. Hence bigger pores remain in case of compacts prepared by coarser powder.

Also, there was less liquid pool formation in liquid phase sintered samples prepared with milled powders as milling causes the well distribution of the powder components. Microstructure reveals that in case of mixed powder sample there is too much tungsten spheroid coalescence but milling results in better separation of tungsten spheroids.

## **4.5. Quantitative Metallographic Studies**

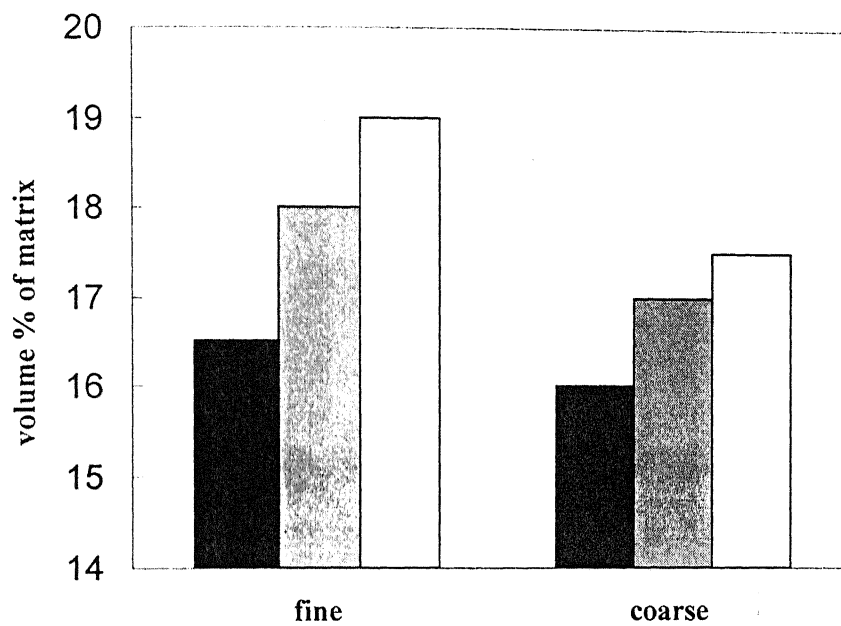
### **4.5.1. Volume Fraction of Matrix**

Figure 4.11 shows the comparison of volume fractions of matrix in sintered compacts prepared by mixed, ball and attritor milled powders. For finer tungsten particles, higher volume fraction of matrix was observed.

For tungsten heavy alloys, matrix is mainly a solid solution of tungsten in binding elements (Ni and Fe). Some intermetallics may also form depending on the interaction of binders with tungsten. Maximum solubility of tungsten in the binder metal falls in the sequence Ni (40%)-Fe (33%) [76]. As the particle size decreases, surface area per unit volume increases. Hence better dissolution of tungsten in liquid occurs. As the extent of milling increases, particle size decreases and stored energy increases which results in the higher dissolution of tungsten and henceforth, volume fraction of matrix increases. That's why highest volume fraction of matrix observed in attritor milled powder compacts.

### **4.5.2. Contiguity and Connectivity**

Figures 4.12 and 4.13 show the effect of powder size and milling condition on contiguity and connectivity respectively. It was observed that both contiguity and



**Figure 4.11.** Effect of particle size and milling on volume fraction of matrix.

■ mixed  
▨ ball milled  
□ attritor milled

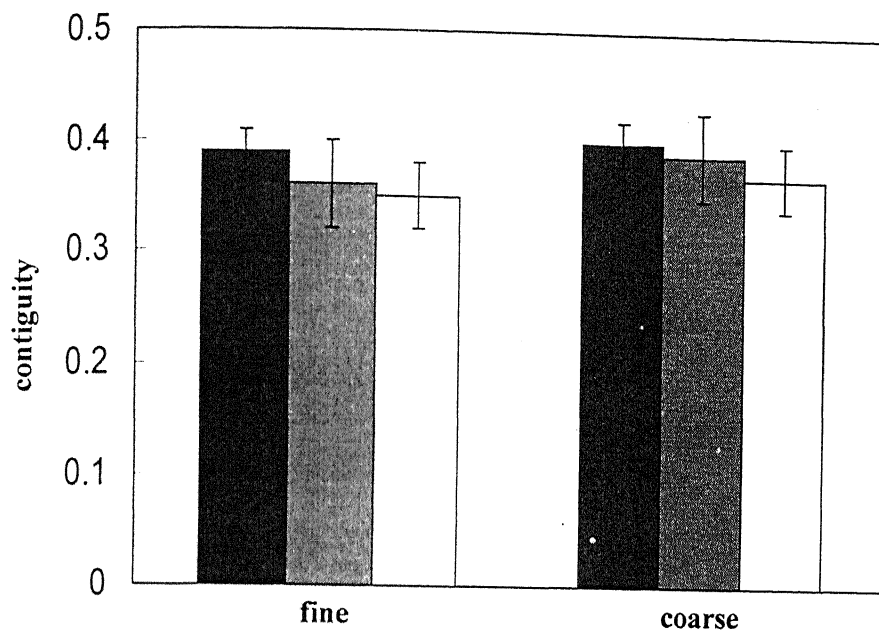


Figure 4.12. Effect of particle size and milling on contiguity.

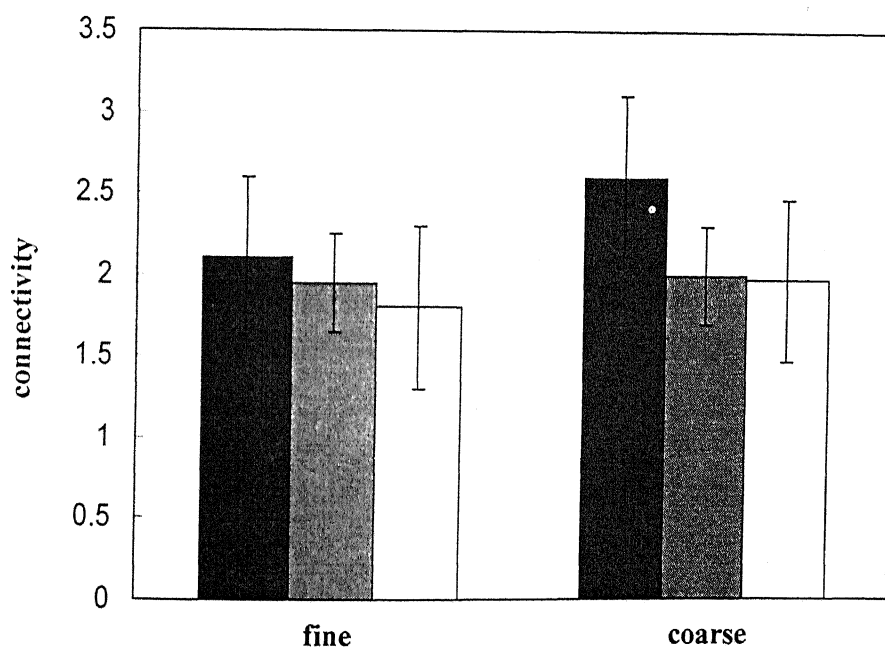


Figure 4.13. Effect of particle size and milling on connectivity.

■ mixed  
■ ball milled  
□ attritor milled

connectivity reduces with decrease in powders size. Milling caused a significant decrease in both contiguity and connectivity.

For smaller particles capillary pressure will be higher according to equation 4.1 which results in better melt penetration across the interface. This causes a decrease in contiguity. Milling increases homogeneity that's why chances of liquid pool formation reduces. During milling, binder phase get welded on the surface of the tungsten particles, which forms melt during sintering, so chances of tungsten/tungsten contact reduces.

The two-dimensional grain co-ordination number is called connectivity and it depends on dihedral angle and solid content. With the decrease in tungsten content and milling, connectivity also decreases due to a reduction in tungsten-tungsten contact.

#### 4.5.3. Dihedral Angle

Figures 4.14 shows the results of dihedral angle measurement of sintered samples prepared by mixed, ball and attritor milled powders respectively. The figure shows the variation in dihedral angle with powder size and type of milling. It was observed that milling reduced dihedral angle. Dihedral angle is lowest in case of attritor milled powder compact. During sintering binder melts down and after exposure to liquid, a stabilized solid-liquid structure emerges as shown by the two-particle configuration in Figure 4.15. The equilibrium condition occurs when the solid grains form stable necks with a surrounding liquid. The stable neck size  $X$  is given by the grain size  $G$  and dihedral angle  $\phi$ ,

$$X = G \sin (\phi/2) \dots\dots\dots (4.2)$$

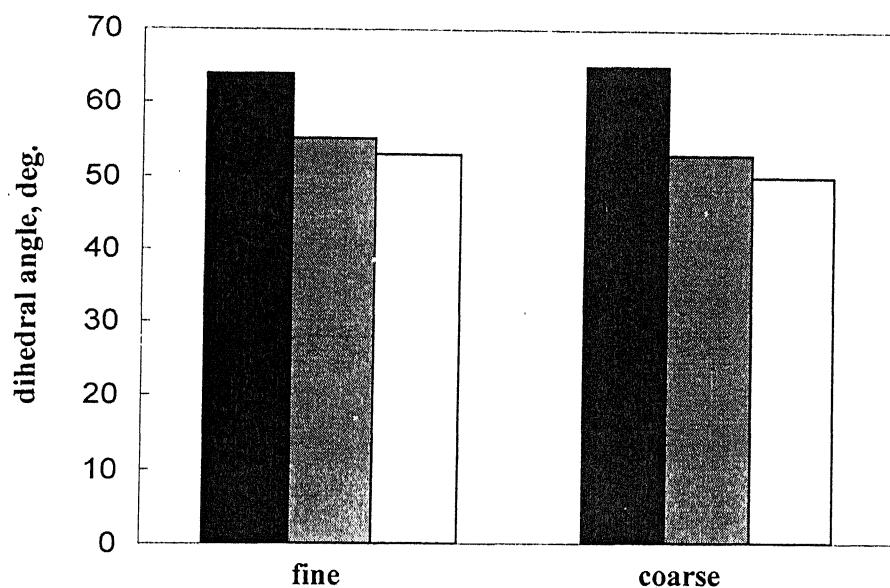


Figure 4.14. Effect of particle size and milling on dihedral angle.

■ mixed  
 ■ ball milled  
 □ attritor milled

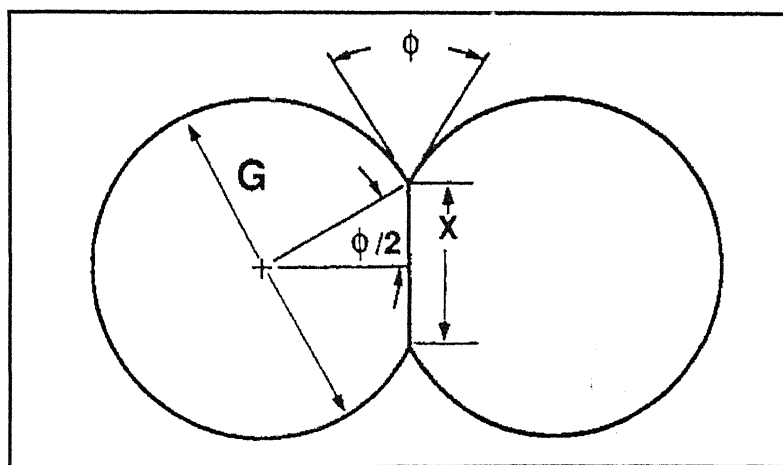


Figure 4.15. Two-particle configuration in equilibrium state.

Due to milling ductile binders cover up hard tungsten powders. During sintering layer of binders melt down and penetrates between grains and thus tungsten/tungsten contact (contiguity) reduces and smaller neck forms [12]. Due to milling better dissolution of tungsten occurred and composition of matrix changed, which resulted the reduction in dihedral angle.

#### **4.5.4. Grain Size**

Figure 4.16 shows the effect of particle size and milling on the average grain size of liquid phase sintered WHA sample. It was observed that milling reduced the average tungsten grain size. In liquid phase sintering binder melts down during sintering. Tungsten has sufficient solubility in Ni-Fe melt, so it starts solution re-precipitation in the second stage of sintering and finally grain coarsening occurs. Milling reduces powder size so in case of milled powder compacts; initial powder size is lower than that for mixed powder compacts. This results in smaller spheroids form in the same sintering temperature and time.

#### **4.6. Electron Micro-Probe Analysis (EPMA)**

Table 4.2 to 4.5 show the element contents in matrix phase as well as in tungsten grain of solid state as well as liquid phase sintered WHA respectively. Figures 4.17 to 4.22 display the X-Ray mapping results taken during the EPMA. It is quite obvious that milled samples give more uniform distribution of the elements. During milling the binder elements welded with tungsten grain which while sintering melt and penetrate through grain boundaries effectively and avoid any formation of binder pool.

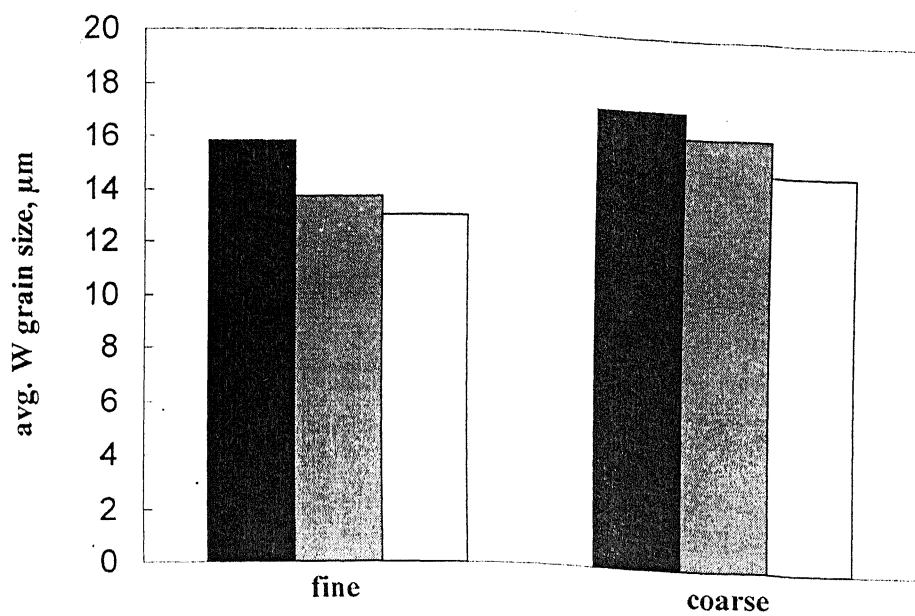


**Figure 4.16.** Effect of powder size and milling on the average tungsten spheroid size.

■ mixed  
▨ ball milled  
□ attritor milled

**Table 4.2.** Element contents in matrix phase of solid state sintered samples.

	<b>W</b>	<b>Ni</b>	<b>Fe</b>
<b>mixed</b>	$33.80 \pm 3$	$55.12 \pm 2.5$	$11.02 \pm 1$
<b>ball milled</b>	$25.35 \pm 3$	$53.28 \pm 1$	$21.37 \pm 2.5$
<b>attritor milled</b>	$64.80 \pm 16$	$28.96 \pm 1$	$26.28 \pm 4$

**Table 4.3.** Element contents in tungsten grain of solid state sintered samples.

	<b>W</b>	<b>Ni</b>	<b>Fe</b>
<b>mixed</b>	$99.03 \pm 0.1$	$0.10 \pm 0.1$	$0.06 \pm .02$
<b>ball milled</b>	$97.71 \pm 0.1$	$1.64 \pm 0.3$	$0.64 \pm 0.1$
<b>attritor milled</b>	$99.89 \pm 3$	$0.05 \pm 2.5$	$0.04 \pm 0.8$



**Table 4.4.** Element contents in matrix phase of liquid phase sintered samples.

	<b>W</b>	<b>Ni</b>	<b>Fe</b>
<b>mixed</b>	$27.5 \pm 4$	$49.8 \pm 4$	$9.6 \pm 2$
<b>ball milled</b>	$68.1 \pm 16$	$16 \pm 7$	$2 \pm 6$
<b>attritor milled</b>	$77.8 \pm 3$	$12.5 \pm 3$	$1.8 \pm 3$

**Table 4.5.** Element contents in tungsten grain of liquid phase sintered samples.

	<b>W</b>	<b>Ni</b>	<b>Fe</b>
<b>mixed</b>	$98.9 \pm 0.3$	$0.1 \pm 0.4$	$0.08 \pm 0.3$
<b>ball milled</b>	$68.1 \pm 16$	$16 \pm 7$	$2 \pm 6$
<b>attritor milled</b>	$97.8 \pm 05$	$0.1 \pm 0.3$	$0.09 \pm 0.3$

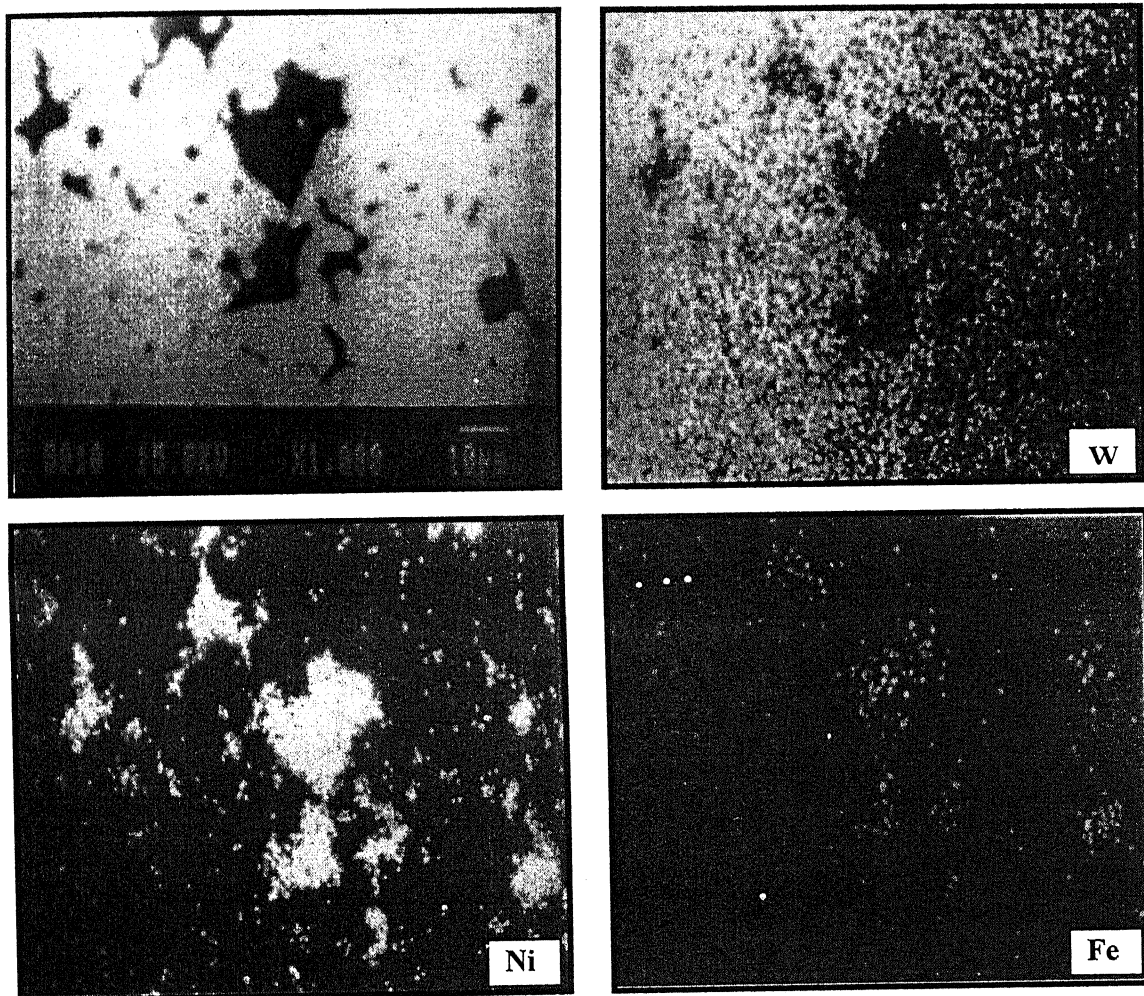


**Figure 4.17.** X-ray mapping showing the elemental distributions of solid state sintered 90W-7Ni-3Fe alloy consolidated with mixed powders.

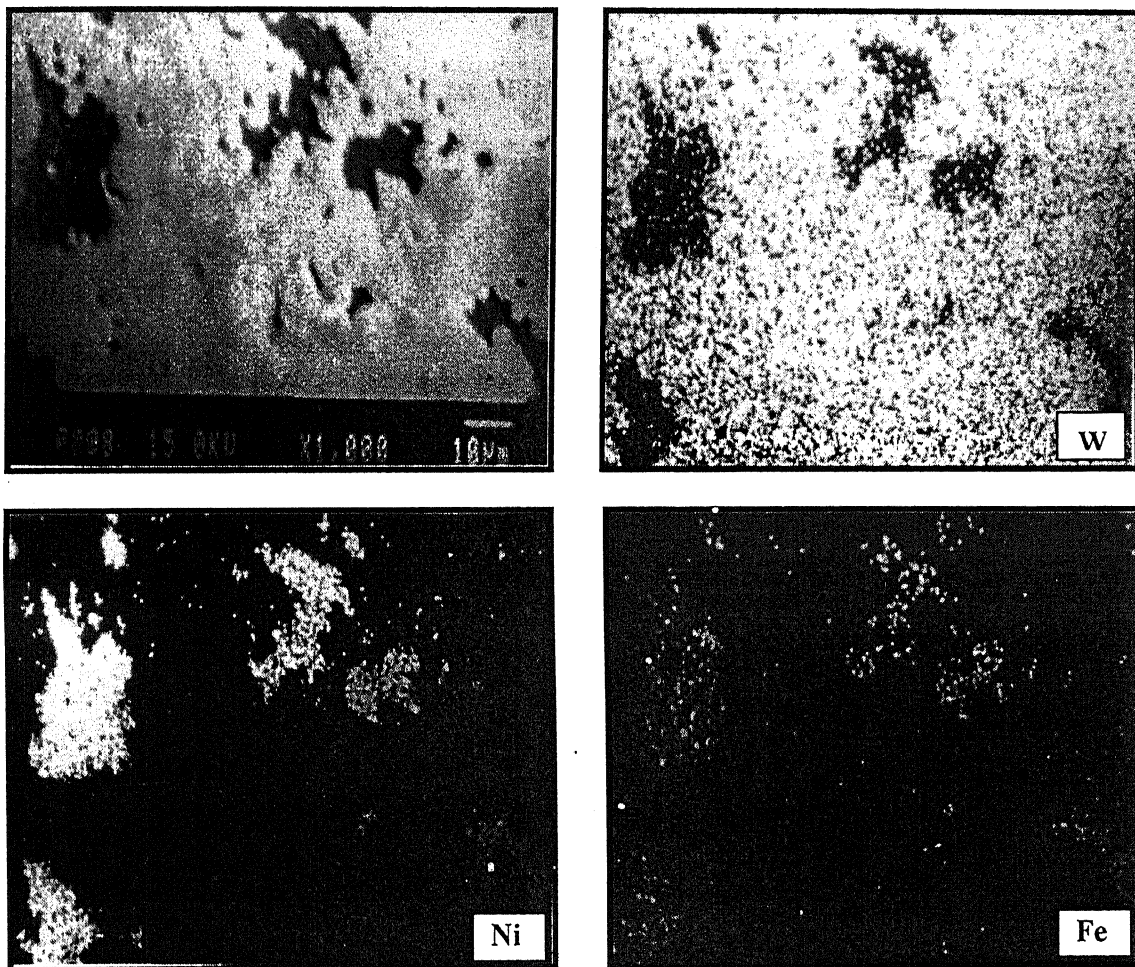


**Figure 4.18.** X-ray mapping showing the elemental distributions of solid state sintered 90W-7Ni-3Fe alloy consolidated with ball milled powders.

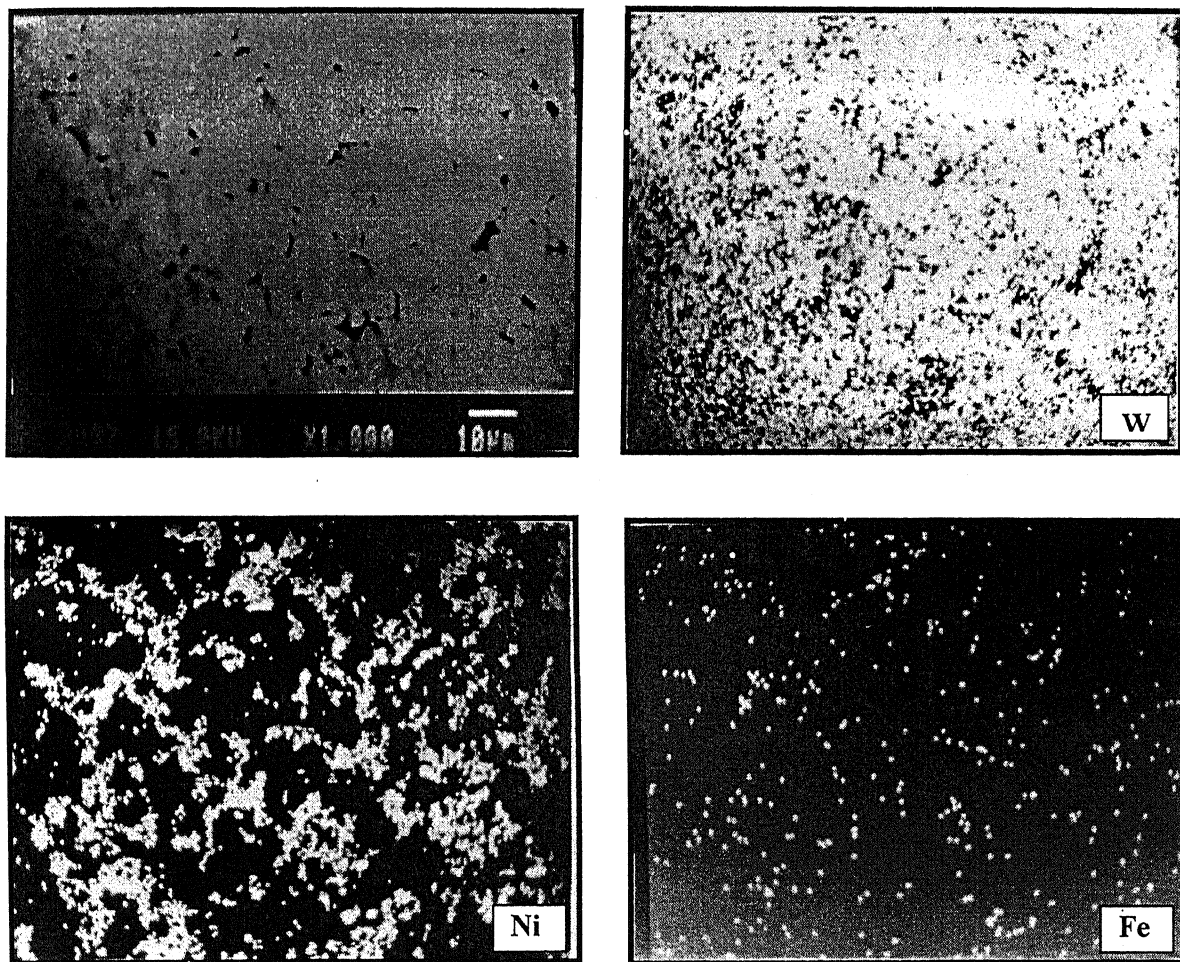


**Figure 4.19.** X-ray mapping showing the elemental distributions of solid state sintered 90W-7Ni-3Fe alloy consolidated with attritor milled powders.

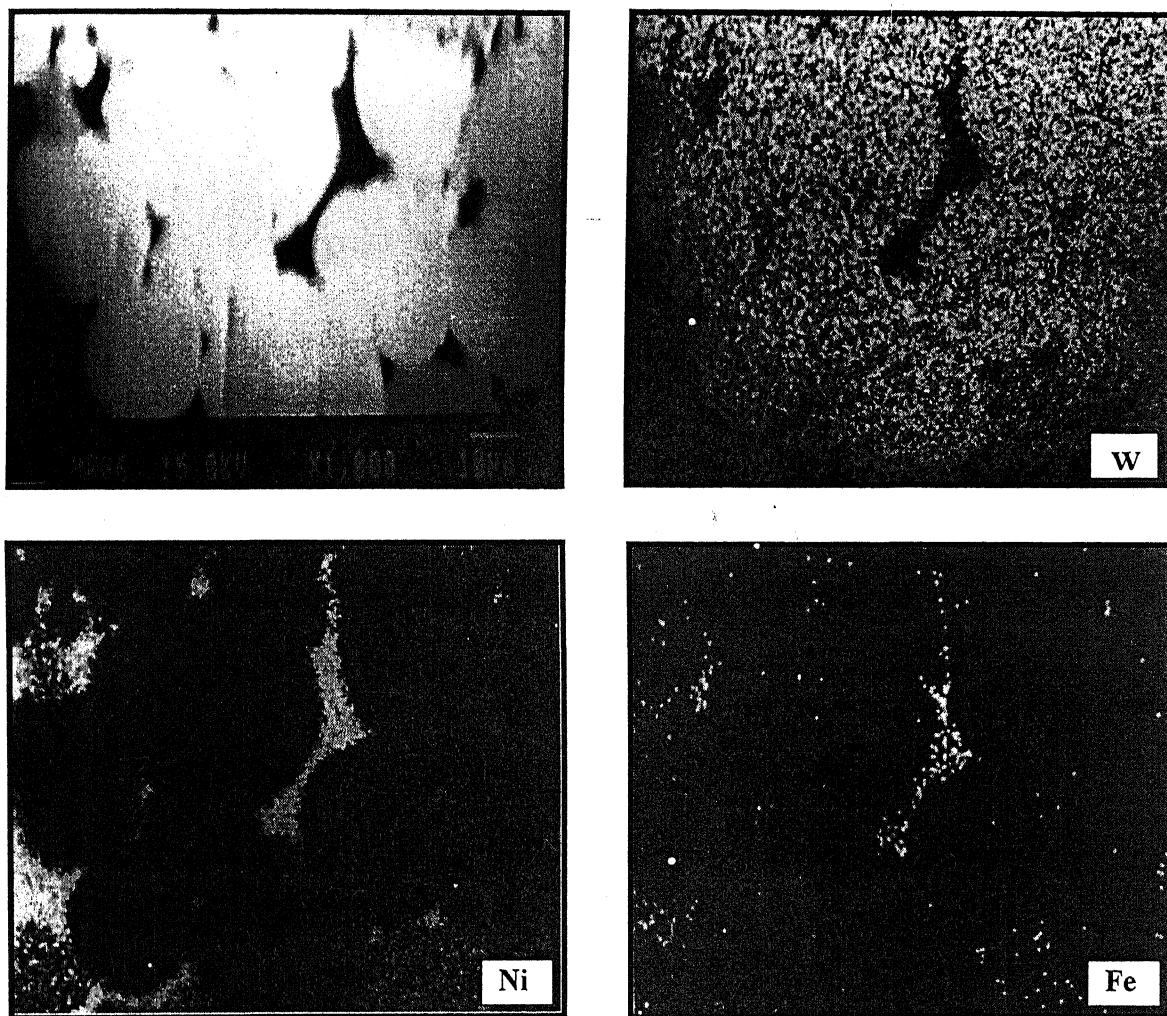


**Figure 4.20.** X-ray mapping showing the elemental distributions of liquid phase sintered 90W-7Ni-3Fe alloy consolidated with mixed powders.

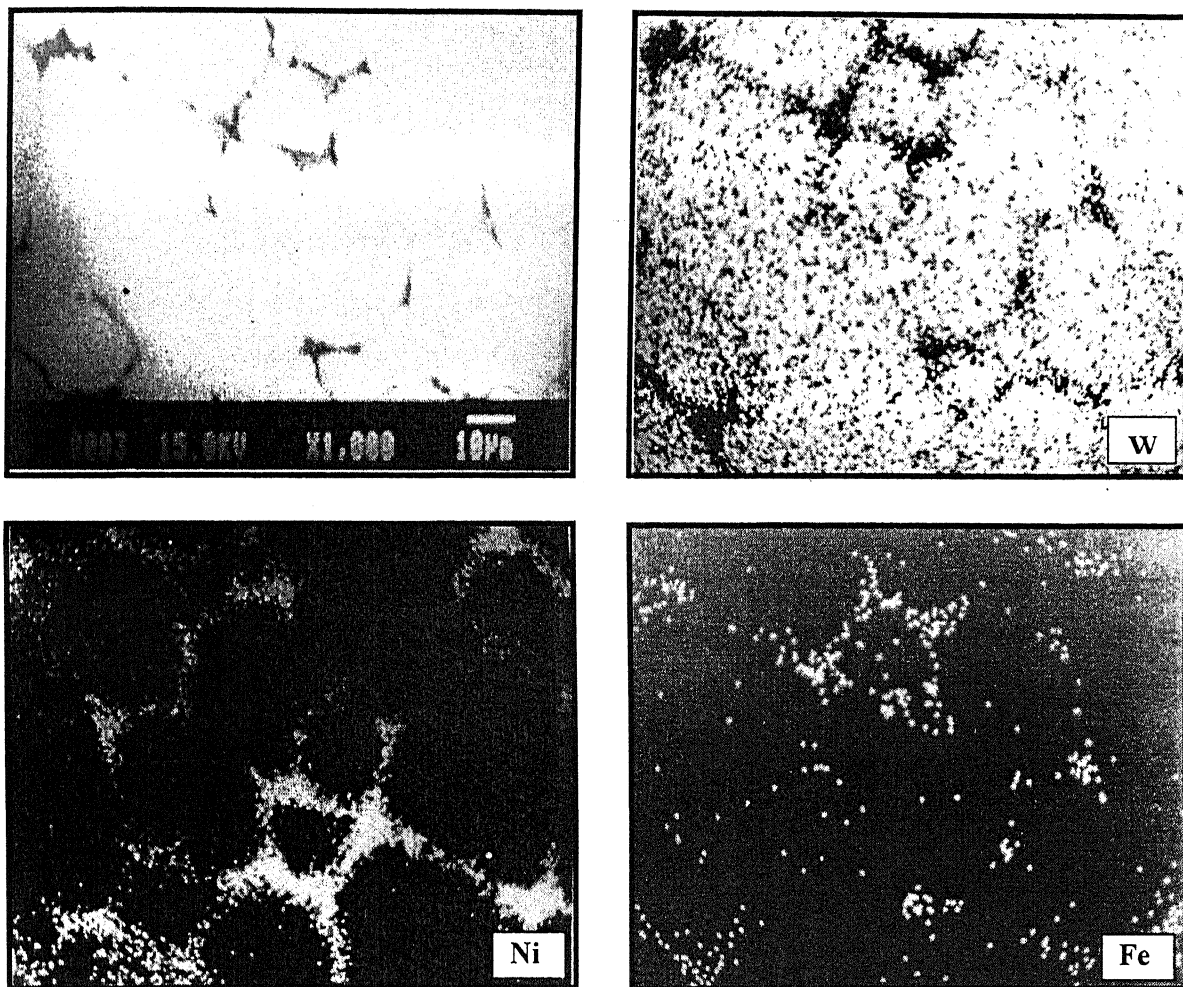


**Figure 4.21.** X-ray mapping showing the elemental distributions of liquid phase sintered 90W-7Ni-3Fe alloy consolidated with ball milled powders.



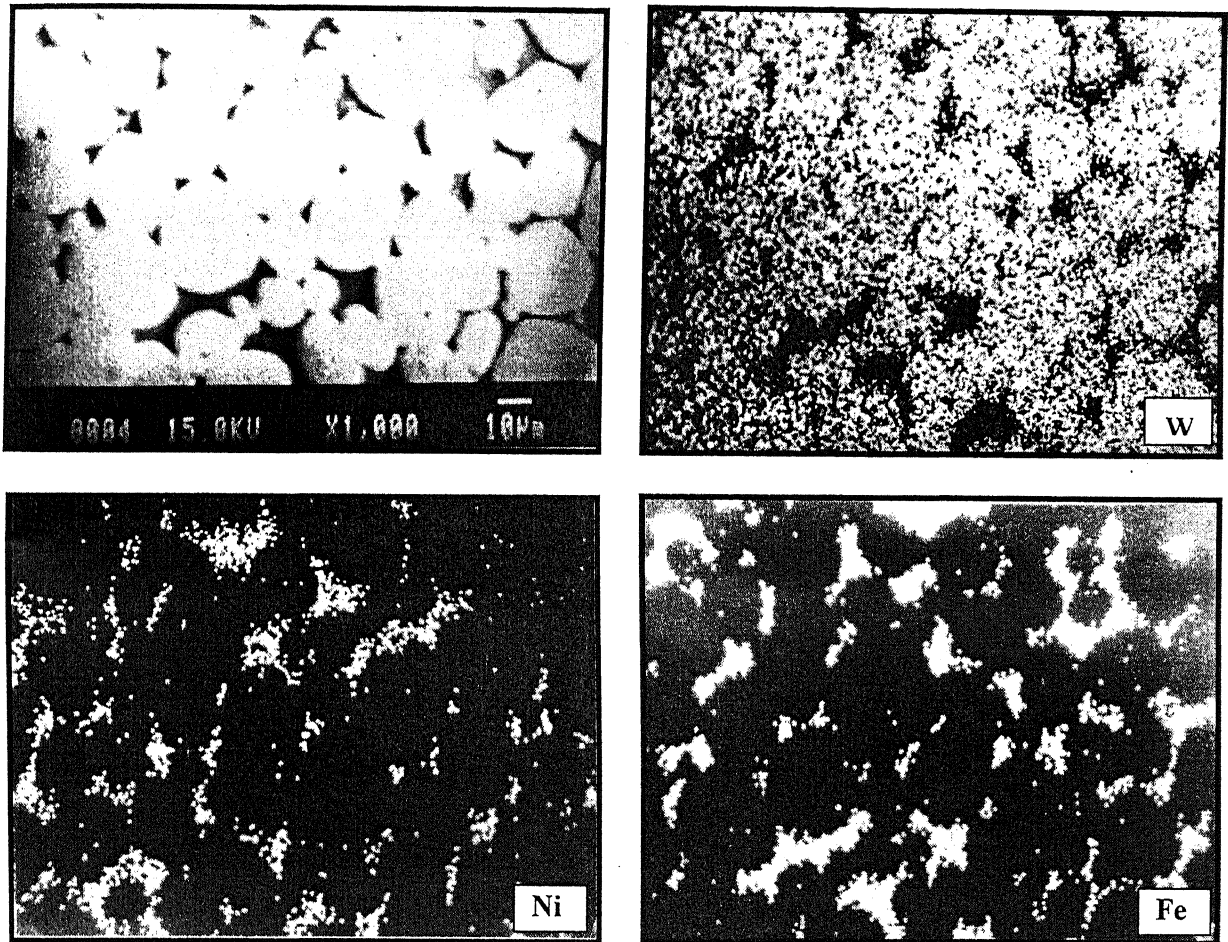


**Figure 4.22.** X-ray mapping showing the elemental distributions of liquid phase sintered 90W-7Ni-3Fe alloy consolidated with attritor milled powders.

## **4.7. Mechanical Properties**

### **4.7.1. Bulkhardness**

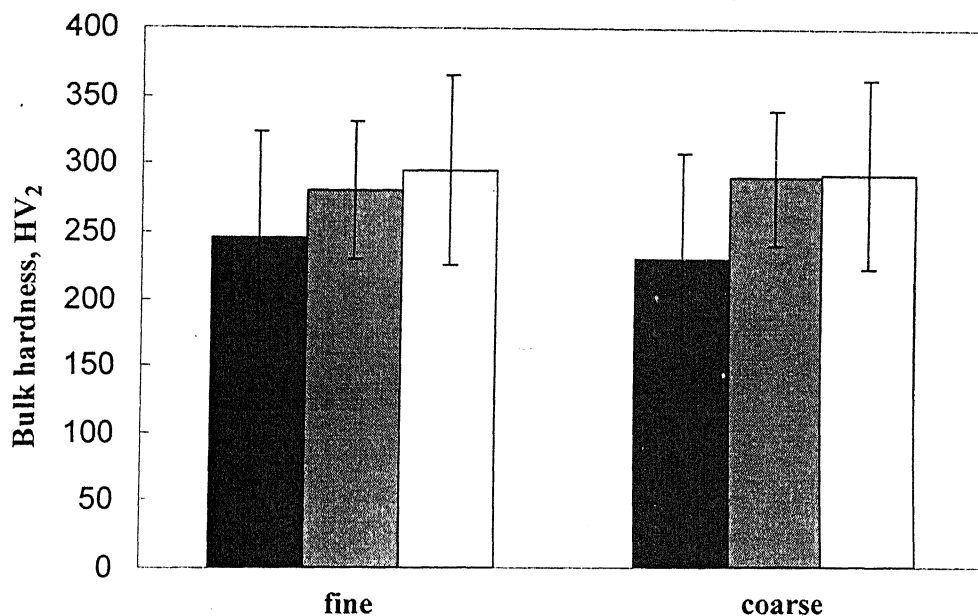
Figure 4.23 shows the variation in bulkhardness values (VHN) of solid-state sintered compacts prepared by mixed, ball and attritor milled powder, with change in particle size and type of milling. It was observed that hardness values increased with milling and reduction in particle size. Figure 4.24 shows the same for liquid phase sintered samples. It was observed that hardness slightly increased with decrease in average particle size and powder milling.

As the particle size reduces higher percentage theoretical sintered density can be achieved. Since higher sintered density can be achieved with milled powder; volume fraction of pore will be lower in case of milled powder. Due to lower volume fraction and average size of pore in compacts prepared by milled powder, hardness will be higher. The effect of milling on hardness was not very clear, as only a slight increase in hardness values were found. With smaller powder better solutionizing of tungsten in matrix and hence better densification occurs. Milling increases amount of tungsten, which is a harder phase, in matrix because better solutionizing occurs due to proper mixing, which results in increased bulk hardness values.

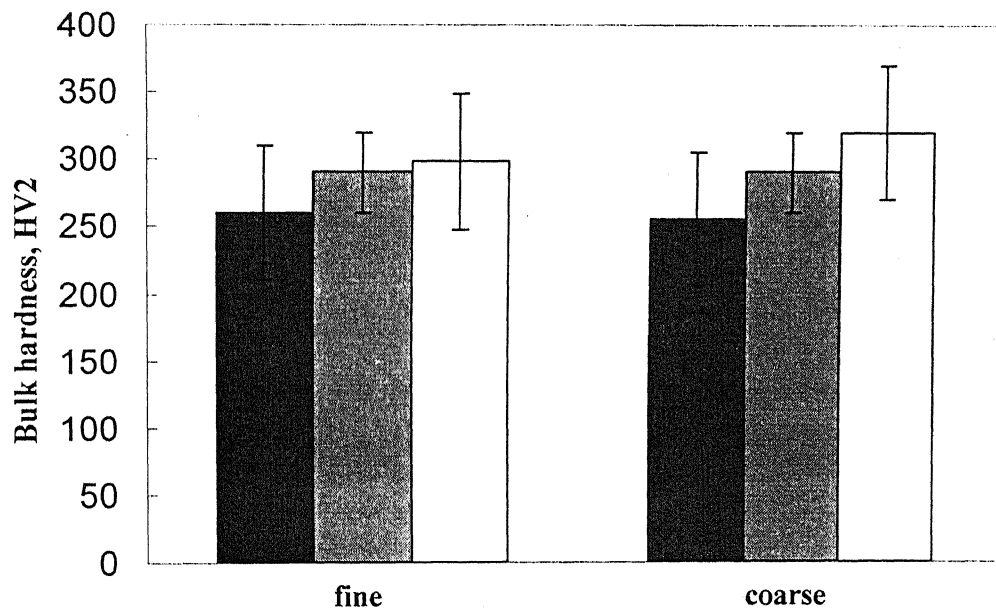
### **4.7.2. Microhardness**

Figure 4.25 shows the effect of average particle size and milling on microhardness of matrix phase. It was found that micro-hardness of matrix phase increases with milling and reduction in average particle size. In case of sintered compacts prepared by attritor milling hardness of matrix was highest.





**Figure 4.23.** Effect of milling and particle size on bulk hardness of solid state sintered 90W-7Ni-3Fe alloy.



**Figure 4.24.** Effect of milling and particle size on bulk hardness of liquid phase sintered 90W-7Ni-3Fe alloy.

■ mixed  
▨ ball milled  
□ attritor milled

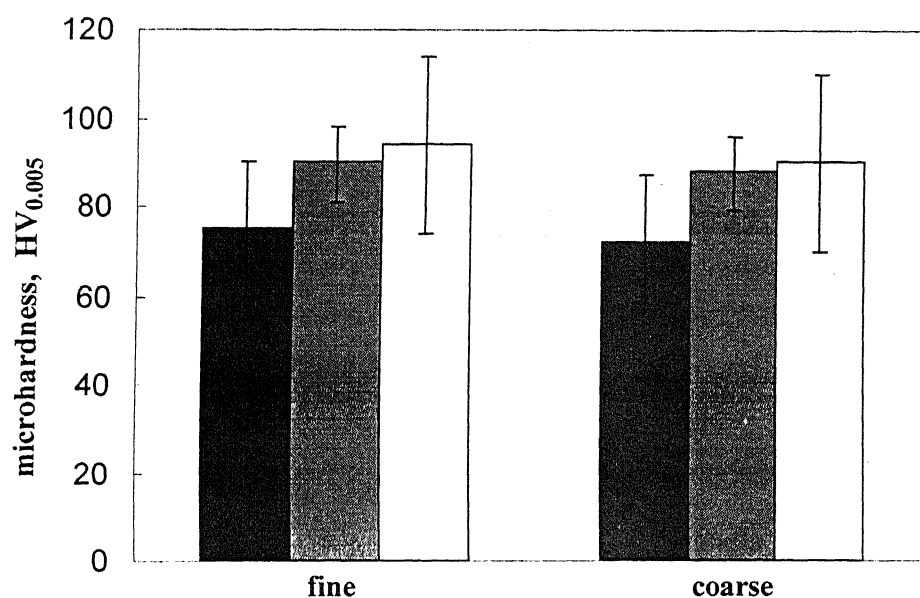


**Figure 4.25.** Effect of milling and particle size on microhardness of matrix Phase of liquid phase sintered 90W-7Ni-3Fe alloy.

■ mixed  
▨ ball milled  
□ attritor milled

In tungsten heavy alloys tungsten is harder phase and matrix is softer phase. Matrix formed by nickel and iron having some amount of dissolved tungsten. Due to milling homogeneity increases and particle size decreases, responsible for better dissolution of tungsten in matrix. It is also confirmed by the measurement of volume fraction of matrix that higher amount of tungsten gets dissolved in the matrix phase for milled samples. Since the amount of harder phase (tungsten) increases in matrix microhardness of matrix phase increases due to milling.

#### 4.7.3. Compression Test Studies at Room Temperature

Figure 4.26 shows the pictorial view of the room temperature compression test samples of liquid phase sintered WHA compacts. All compacts were tested in compression at a nominal strain rate of  $4.5 \times 10^{-3} \text{ s}^{-1}$ . None of the compacts fractured during compression. The complete set of results of compression test i.e. axial and radial deformation along with hardness is presented in Tables 4.6 and 4.7. The compacts exhibit significant plastic deformation without fracture upto 3 GPa applied stress.

Figure 4.27 compares the SEM micrographs of WHA alloys in as-sintered ( $1400^\circ\text{C}$ , 1h and  $1500^\circ\text{C}$ , 1h) and compressed condition. The alloys achieved sintered densities of 87% and 95% of the theoretical density, respectively. Figures 4.27a and 4.27b show the SEM micrograph of solid-state and liquid-phase sintered 90W-7Ni-3Fe alloys. Subsequently, both the sintered compacts were pressed up to 200 kN and the microstructure was evaluated. The deformed tungsten grains are very distinctly shown in case of liquid phase sintered 90W alloy (Figure 5.27d).

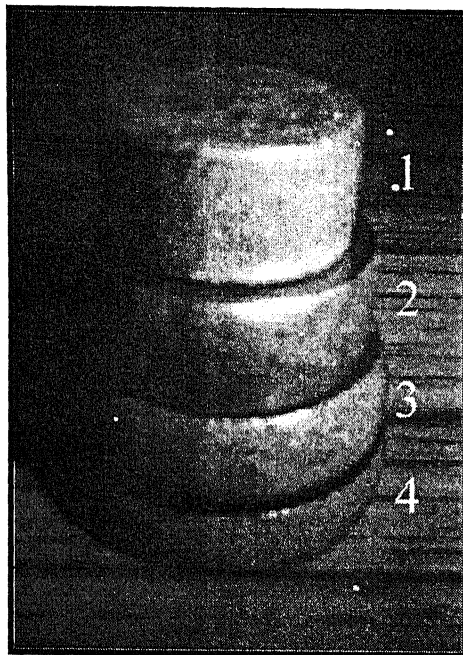


**Figure 4.26.** Pictorial view of liquid phase sintered 90W-7Ni-3Fe alloy (1) as-sintered (2) compressed at 200 kN (3) compressed at 300 kN and (4) 350 kN.

**Table 4.6.** Properties of 90W-7Ni-3Fe alloy in as sintered condition.

Sintering condition	Sintered density (g/cm <sup>3</sup> , % theor.)	Densification parameter	Bulk hardness HV <sub>2</sub>	
			L	T
Solid state 1400°C, 1h	14.9 (87%)	0.6	192 ± 11	183 ± 18
Liquid phase 1500°C, 1h	16.6 (95%)	0.9	338 ± 16	351 ± 21

**Table 4.7.** Properties of 90W-7Ni-3Fe alloy after compression test.

System	Load, kN	% reduction in height	% increase in diameter	Bulk hardness HV <sub>2</sub>	
				L	T
Solid state 1400°C, 1h	200	34	23	341 ± 22	418 ± 14
Liquid phase 1500°C, 1h	200	35	34	487 ± 10	521 ± 16

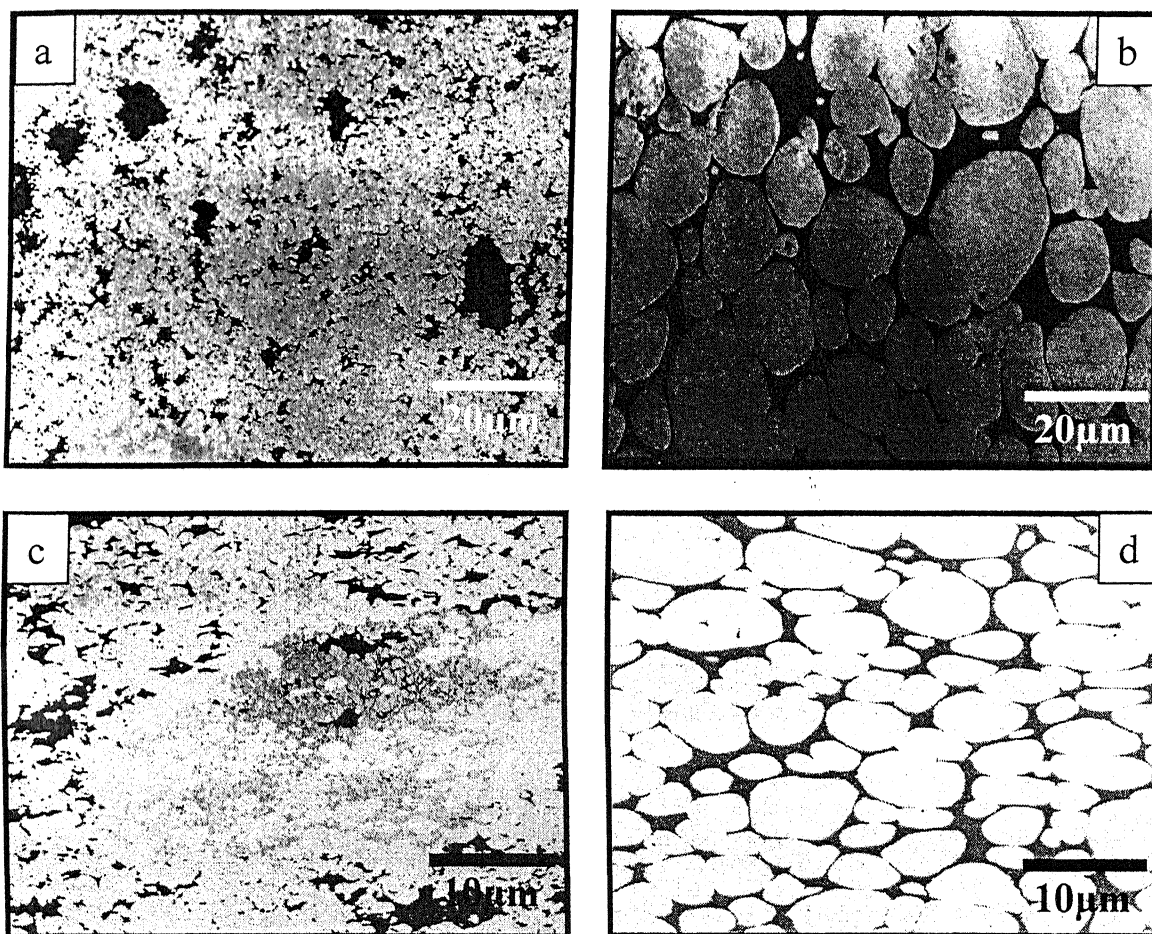


**Figure 4.27.** SEM micrographs of 90W-7Ni-3Fe alloy (a) as solid state sintered (b) as liquid phase sintered (c) solid state sintered sample compressed at 200 kN and (d) liquid phase sintered sample compressed at 200 kN.

Note that the as-sintered alloy exhibits rounded tungsten grains along with intergranular porosity. However, when the same compact was pressed at 200 kN, all the porosity has been eliminated due to deformation of tungsten grains (Figure 4.27d). Solid state sintered samples show the deformation of binder pool which depicts that the deformation stress is absorbed by the tungsten grain as well as the matrix phase but in liquid phase sintered samples no sign of matrix phase deformation is observed. The stress is sustained by only the tungsten grains.

## **4.8. Microwave Sintering**

### **4.8.1. Heating Profile**

Figure 4.28 compares the heating profiles and power consumption of 92.5W-6.4Ni-1.1Fe compacts during microwave and conventional sintering. In case of microwave heating, the sintering time reduces by 45% as compared to the conventional sintering. As depicted by figure, the microwave sintering is more efficient and cuts about 45% power consumption.

### **4.8.2 Sintered Density and Densification Parameter**

The sintered density and densification parameter values for tungsten heavy alloy are compiled in Table 4.8. Both microwave and conventional sintered WHAs show similar densification parameter, though processing time for microwave sintering is quite low with compared to the conventional one. This could be attributed to both having similar sintered density and underscores the efficacy of microwave furnace in consolidating these alloys. As shown in Figure 4.29, the W grain size in microwave sintered condition is smaller (W-grain size-9.4 $\mu\text{m}$ ) as compared to its conventional counterpart (W-grain size-17.3 $\mu\text{m}$ ).

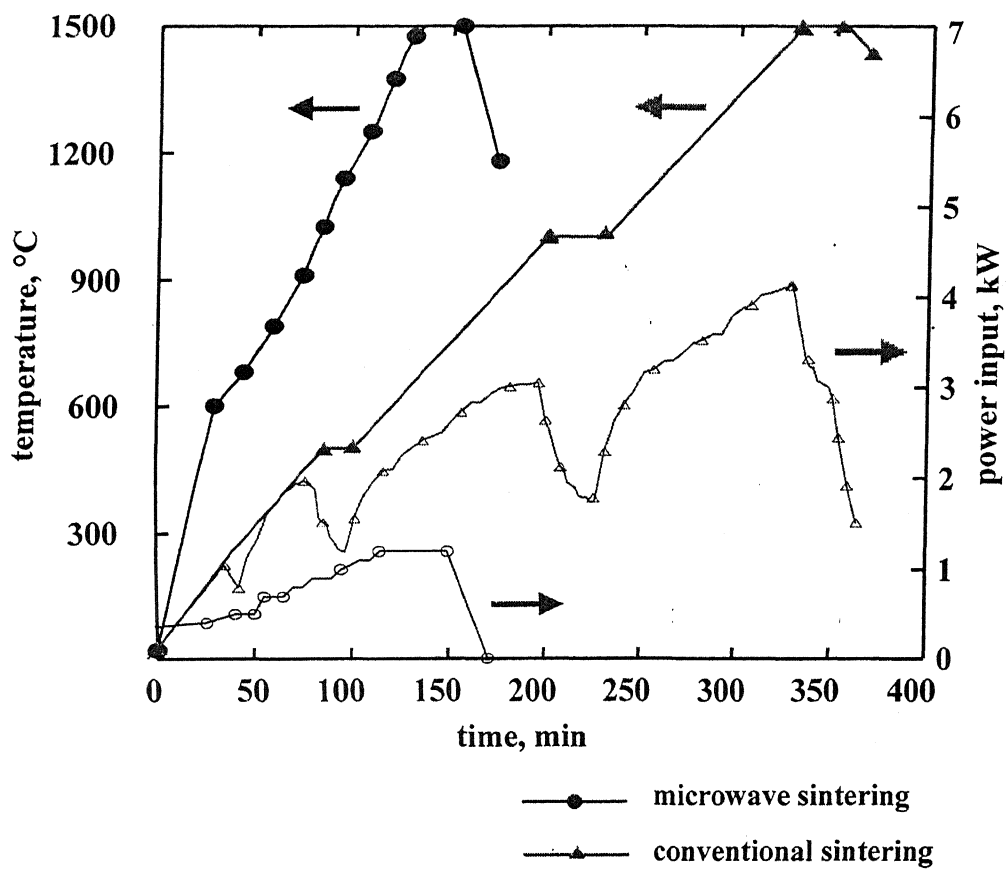


**Figure 4.28.** Comparison of heating profile and power consumption of microwave and conventionally sintered 92.5W-6.4Ni-1.1Fe alloy.



**Table 4.8.** Sintered densities of microwave and conventionally sintered 92.5W-6.4Ni-1.1Fe alloy samples.

<b>Sample</b>	<b>Green density g/cm<sup>3</sup> (% theoretical)</b>	<b>Sintered density g/cm<sup>3</sup> (% theoretical)</b>	<b>Densification parameter</b>
<b>Microwave</b>	10.7 (60.7)	17.2 (97.1)	0.93
<b>Conventional</b>	10.8 (61.2)	17.3 (97.8)	0.94

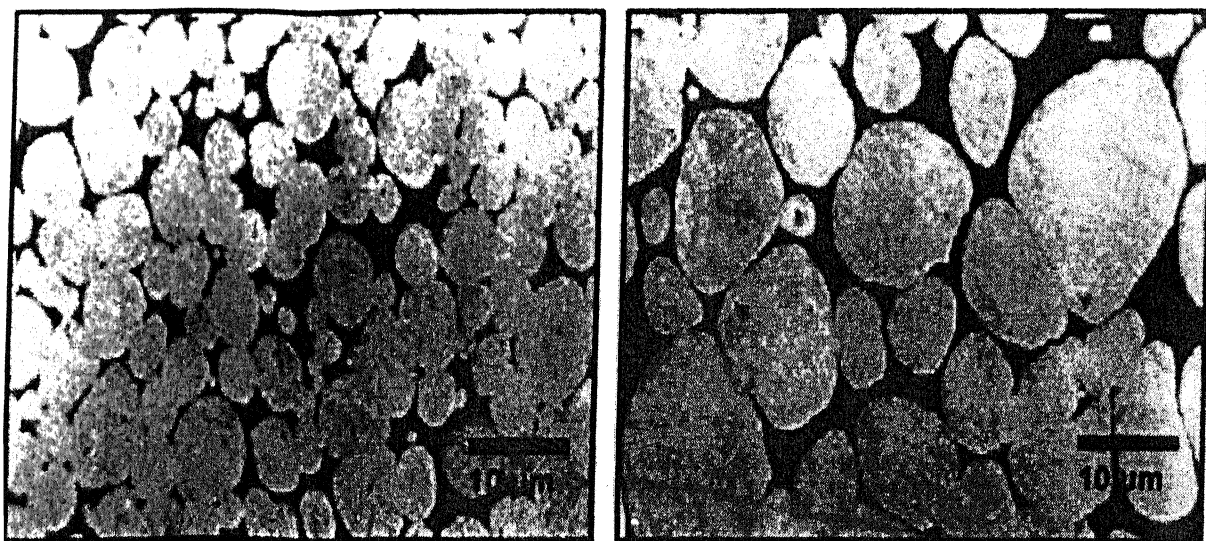


**Figure 4.29.** Scanning electron micrographs (a) microwave (b) conventionally sintered 92.5W-6.4Ni-1.1Fe alloy. The alloys were sintered at 1500°C.

Though processing time for microwave sintering is quite low, densification parameter of both samples is almost same i.e. 0.93 and 0.94 for microwave and conventionally sintered samples respectively. This is possibly due to the higher heating rate in microwave sintering which leads to faster densification. One of the implications of faster sintering is reduced microstructural coarsening [5]. At present, the issue of microwave effects is quite contentious. Many of the expected results from microwave processing such as rapid and uniform heating, inverse temperature profile, more uniform microstructure and selective heating are included in the category of microwave effects. However, this anomaly cannot be easily explained on the basis of our present understanding. Enhancement in the rates of activated process involving material transport is considered microwave effect because they require lower activation energy [77].

Freeman *et al.* [78] has suggested that the rectified potential, generated due to the microwave fields, causes the enhanced reaction and sintering rates. They used single-crystal NaCl and imposed a variable external bias voltage. Currents were measured during exposure to microwave fields. They found the increase in current applying the microwave fields. The additional driving force is attributed to the asymmetry in the defect density on surface of the crystal. The uneven distribution of surface charge introduces a space charge polarization that couples with the microwave field and produces a rectified potential. They suggested that this phenomenon could be the reason for the enhanced reaction and sintering rates observed by several other investigators.

#### 4.8.3. Stereological Quantification

All stereological parameters are summarized in Table 4.9. The corresponding values of solid volume percentage ( $V_s$ ), connectivity ( $C_c$ ), Contiguity ( $C_g$ ) and interfacial surface

**Table 4.9.** Comparison of stereological parameters of microwave and conventionally sintered 92.5W-6.4Ni-1.1Fe alloy samples.

Characteristics	Microwave Sintered (wt%)	Conventionally sintered (wt%)
Tungsten content (vol. %)	$86.7 \pm 4.7$	$78.0 \pm 1.8$
Grain Size ( $\mu\text{m}$ )	$9.40 \pm 0.5$	$17.3 \pm 0.8$
$S_v$ ( $\mu\text{m}^{-1}$ )	$0.31 \pm 0.02$	$0.19 \pm 0.02$
Connectivity ( $C_c$ )	$1.92 \pm 0.7$	$1.78 \pm 0.8$
Contiguity ( $C_g$ )	$0.42 \pm 0.1$	$0.32 \pm 0.1$
Dihedral Angle ( $\Phi_{50}$ )	$63 \pm 8$	$53.5 \pm 7$

area per unit volume ( $S_v$ ) for both samples are plotted in Figure 4.30. Microwave sintered alloy has lower value of mean grain size ( $9.4\mu\text{m}$ ) as compared to conventionally sintered alloy ( $17.3\mu\text{m}$ ) as it can be seen from Figure 4.31. In case of microwave sintering, values of  $C_g$ ,  $C_c$  and  $V_s$  are relatively higher. Grain boundary surface area per unit volume was calculated for both tungsten-tungsten ( $S_{ww}$ ) and tungsten-matrix ( $S_{wm}$ ). It was found that tungsten-matrix interface area is slightly more in case of conventional sintering, whilst there is large difference between tungsten-tungsten interfacial areas of both samples. Figure 4.32 shows the curve of percentage cumulative dihedral angle distribution. The conventionally sintered sample has lower value of mean dihedral angle ( $\Phi_{50}$ ).

It is evident from microstructures that volume fraction of solid (tungsten grains) is higher for microwave sintered alloy. In microwave sintering, short processing time also leads to less diffusion of W into the matrix and thus higher volume percentage of W grains as we know that the diffusion is proportional to the time. The liquid penetration studied by Fredriksson *et al* [79] shows that the penetration is proportional to the square root of time. The driving force for outward diffusion of tungsten is estimated from the capillary inflow creating a pressure gradient along penetrated grain boundaries and thus resulting in a concentration gradient. So, in case of microwave sintering the gradient is not so strong due to less time available, causing higher value of  $S_{w-w}$ , solid volume fraction and contiguity. This means less diffusion of tungsten into the matrix leads to more number of tungsten-tungsten contacts remaining. Therefore, ductility and hence toughness of the specimen will be lesser in case of microwave sintering.

The microstructural parameters determined by stereological quantification, have inter-relationship with each other and the variations between them have been reported by

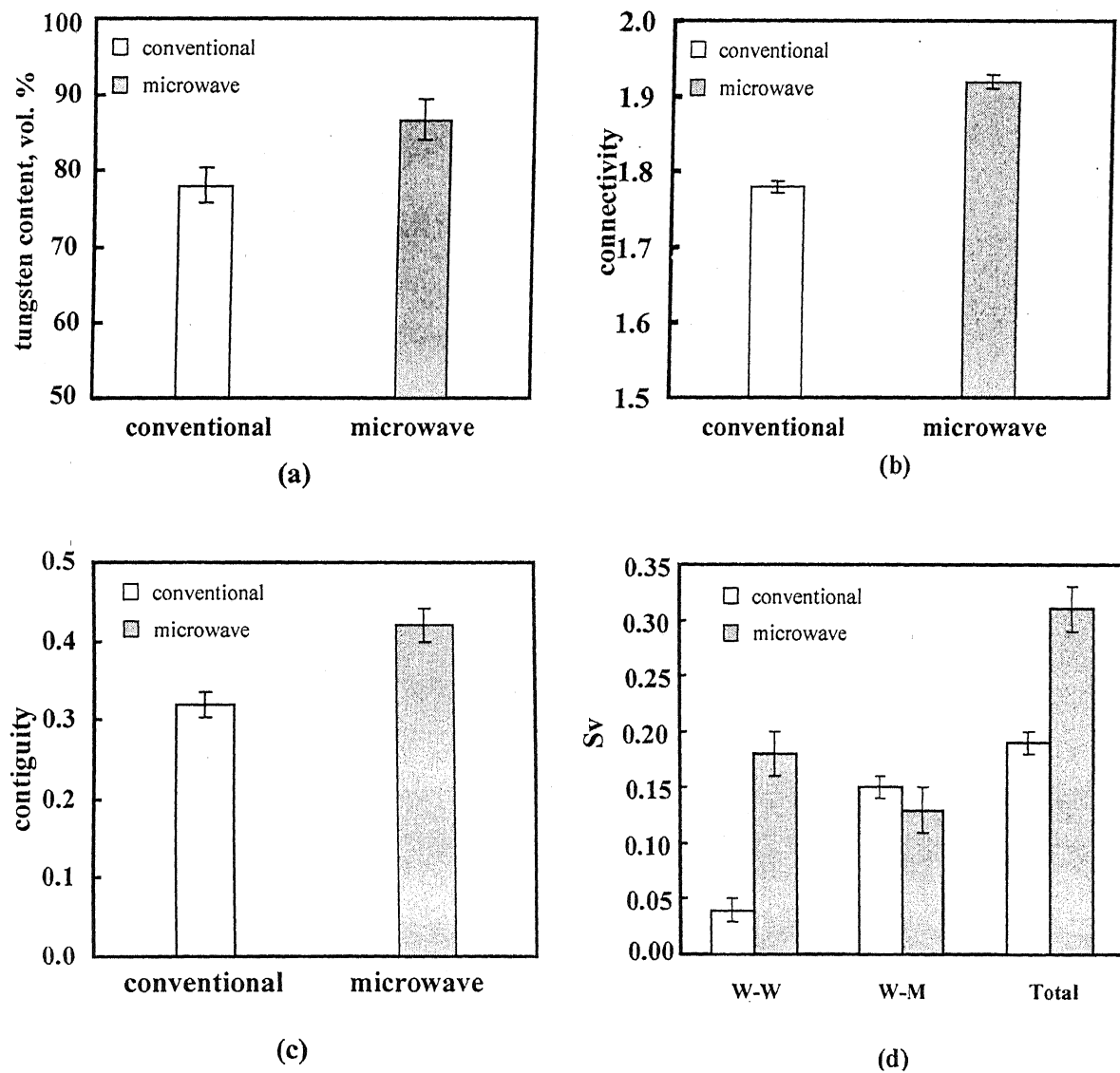


**Figure 4.30.** Comparison of stereological parameters (a) tungsten content (vol. %) (b) connectivity (c) contiguity and (d)  $S_v$  of 92.5W-6.4Ni-1.1Fe alloy sintered through conventional as well as microwave heating.

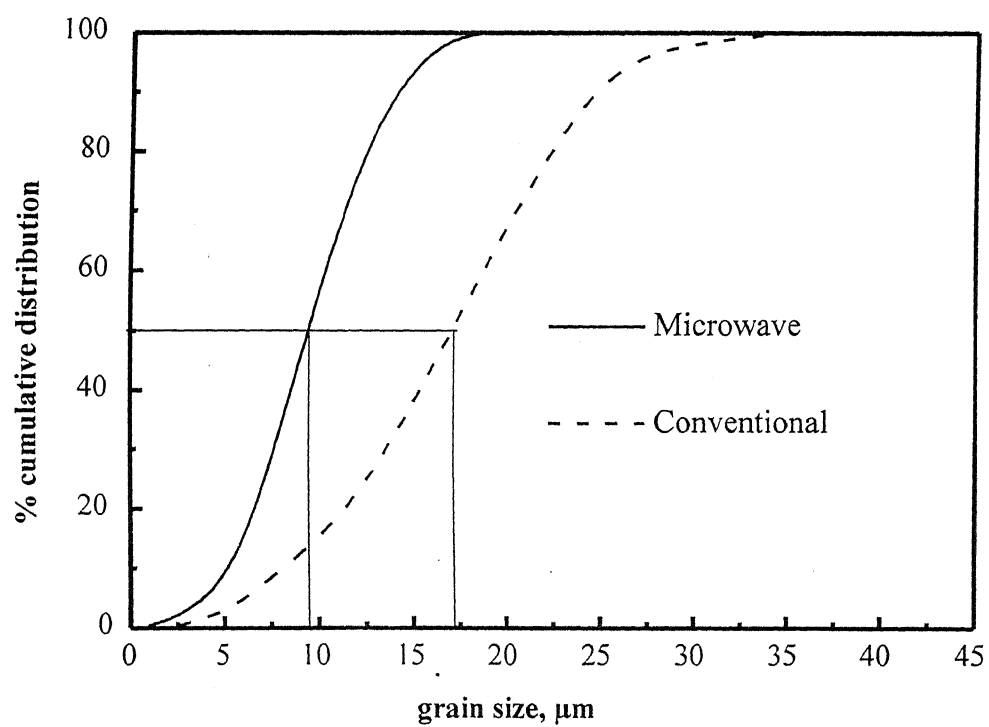


**Figure 4.31.** Grain size distribution curve of 92.5W-6.4Ni-1.1Fe alloy sintered through conventional as well as microwave heating.

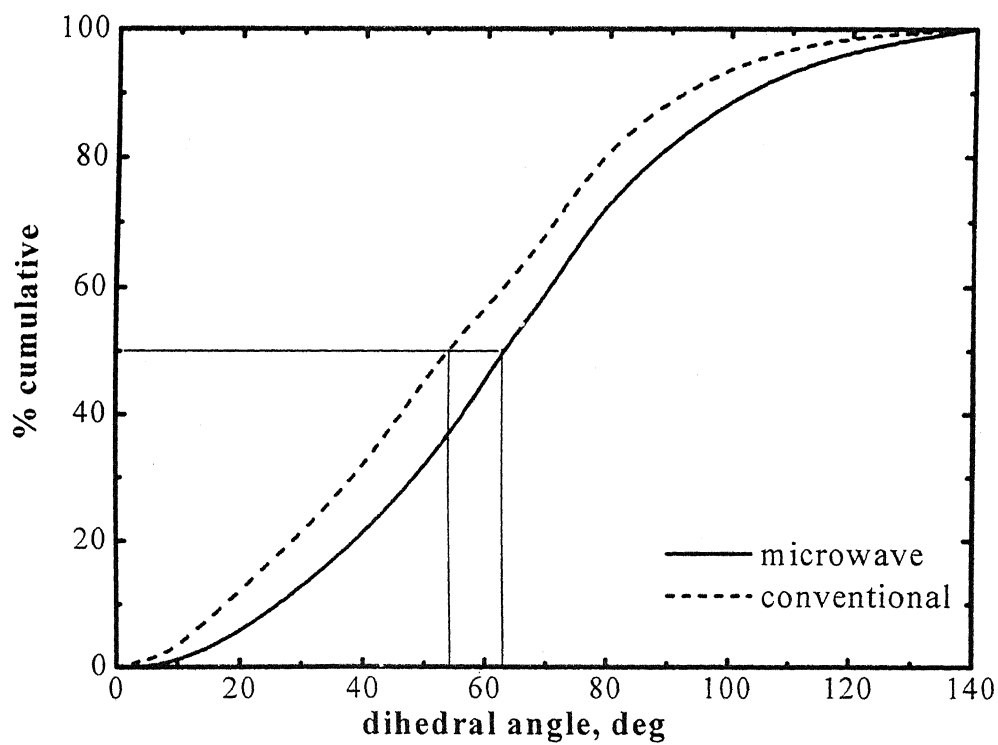


**Figure 4.32.** Comparison of dihedral angle distribution of 92.5W-6.4Ni-1.1Fe alloy sintered through conventional as well as microwave heating.



Upadhyaya [80]. German compiled the variation of contiguity ( $C_g$ ) with the volume fraction tungsten in WHAs for various dihedral angles ( $\Phi$ ) and observed that the lower the dihedral angle, the smaller is the contiguity. He also correlated the effects of various processing parameters, such as interfacial energies, grain size ratios and solid content on the contiguity. His model suggests that the contiguity increases with an increasing solid content and dihedral angle. However, the grain size ratio is of little influential. German's empirical formula relating contiguity ( $C_g$ ) with the solid content ( $V_s$ ) and the dihedral angle ( $\Phi$ ) is as follows:

$$C_g = V_s^2 (0.43 \sin \Phi + 0.35 \sin^2 \Phi) \dots\dots\dots (4.3)$$

When compared to the model provided by German, it is found that the quantified stereological parameters are in good consent with it and is illustrated in Figure 4.33.

Gurland [68] empirically expressed the grain contiguity ( $C_g$ ) as a function of the connectivity ( $C_c$ ) and dihedral angle as follows:

$$C_g = C_c \left( \frac{1 - \cos \frac{\phi}{2}}{3 - \cos \frac{\phi}{2}} \right) \dots\dots\dots (4.4)$$

Figure 4.34 represents the variation in the contiguity as a function of dihedral angle for a given range of connectivities. As predicted, a higher connectivity and a large dihedral angle result in a highly contiguous microstructure. These microstructural properties have an important role in governing mechanical properties of tungsten heavy alloys. Both tensile strength and ductility decreases with increase in contiguity [81].

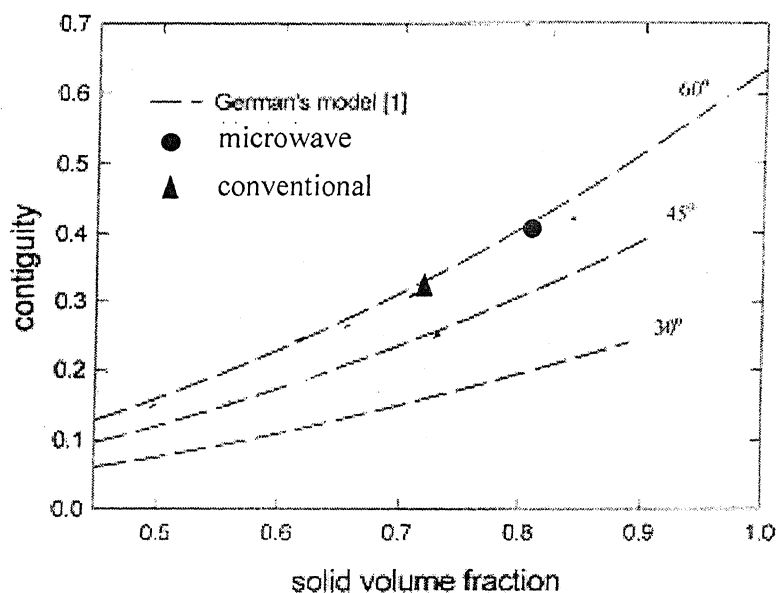


**Figure 4.33.** German's model showing the relationship between contiguity and solid volume fraction keeping dihedral angle constant.

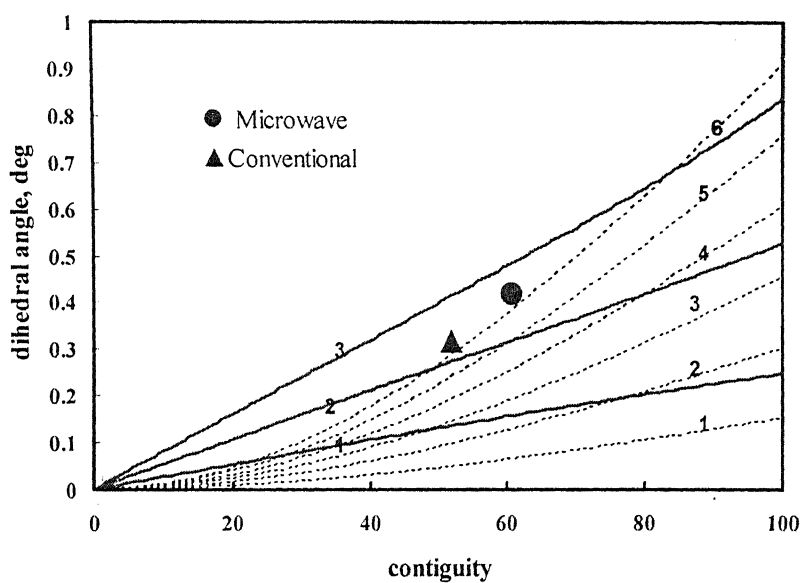


**Figure 4.34.** Gurland's model showing the relationship between dihedral angle and contiguity keeping continuity constant.

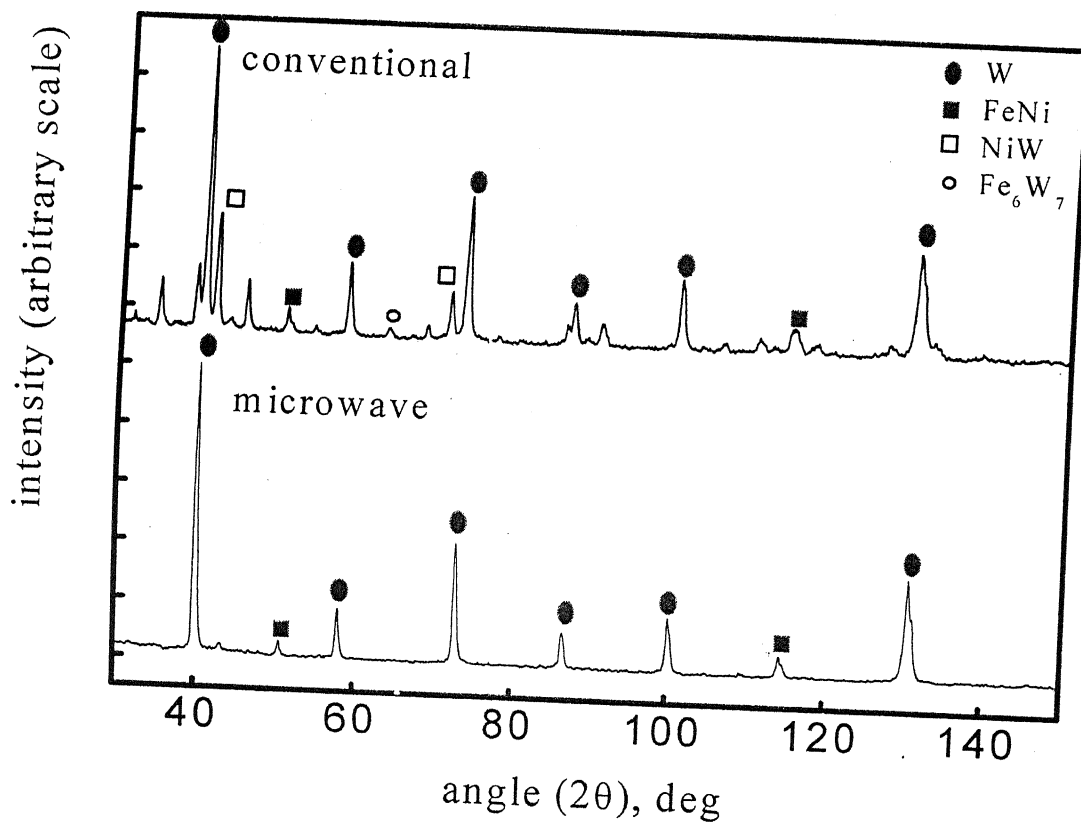
#### 4.8.4. Phase Analysis by XRD

Figure 4.35 compares the XRD patterns of the conventional and microwave sintered tungsten heavy alloy samples taken with the help of X-Ray Diffractometer. In XRD pattern of the conventionally sintered sample, there were more number of peaks observed than the microwave sintered sample. Comparing with the standard patterns of W, Ni, Fe and the intermetallics formed by them, confirmed the formation of various intermetallics in case of conventionally sintered sample (FeNi, NiW, Fe<sub>7</sub>W<sub>6</sub>).

These intermetallics impart brittleness to the alloy and are attributed to slower thermal cycle which provides sufficient time for interdiffusion to attain equilibrium configuration as per the W-Ni-Fe phase diagram. It is well-known that any deviation from Ni: Fe ratio of 7:3 results in intermetallic-phase formation [17]. The present composition had Ni: Fe ratio of 6:1 and hence the intermetallic formation was expected during conventional sintering. An implication of the result is that microwave sintering can be utilized effectively even for non-stoichiometric binder composition.

#### 4.8.5. Electron Probe Micro Analysis (EPMA)

Figures 4.36a and 4.36b show the microstructures of microwave and conventionally sintered samples at 1000x taken during the EPMA analysis along with the X-Ray mapping results which depict that in the microwave sintered sample, tungsten content of matrix as well as of grains is nearly same in both cases.(Table 5.8). Although, the solubility effect in microwave sintering condition is not quite understood, but it can be attributed to the less time available for grains to dissolve in the matrix phase.



**Figure 4.35.** XRD analysis of microwave and conventionally sintered 92.5W-6.4Ni-1.1Fe alloy.

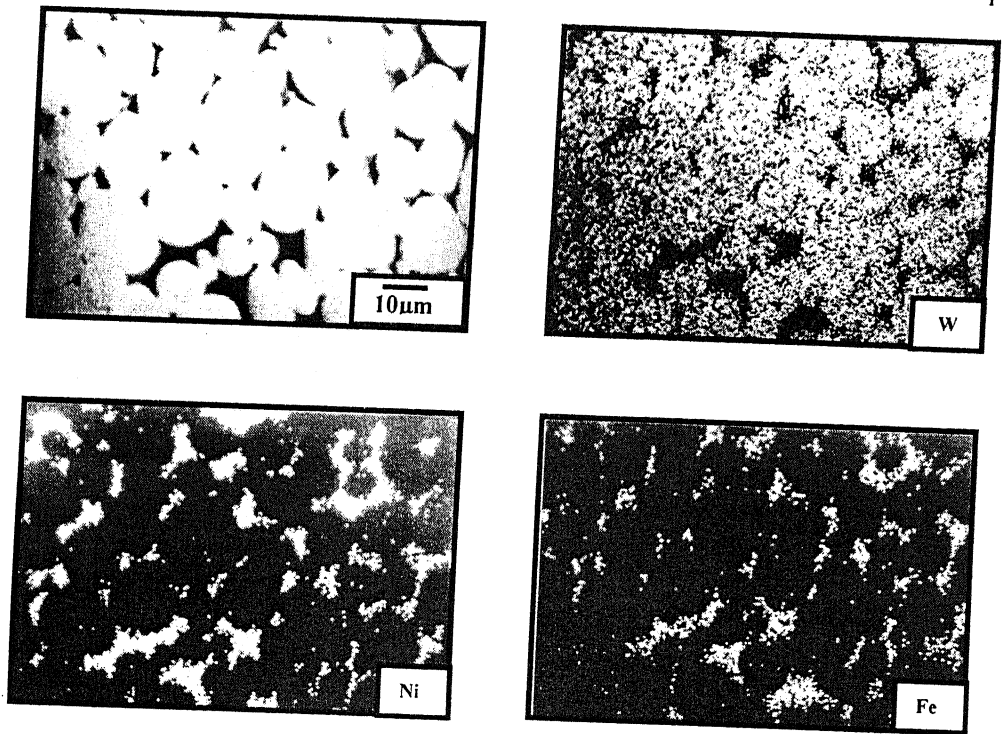


**Figure 4.36a.** Microstructure of microwave sintered 92.5W-6.4Ni-1.1Fe alloy with X-Ray mapping of the elements present in the matrix.

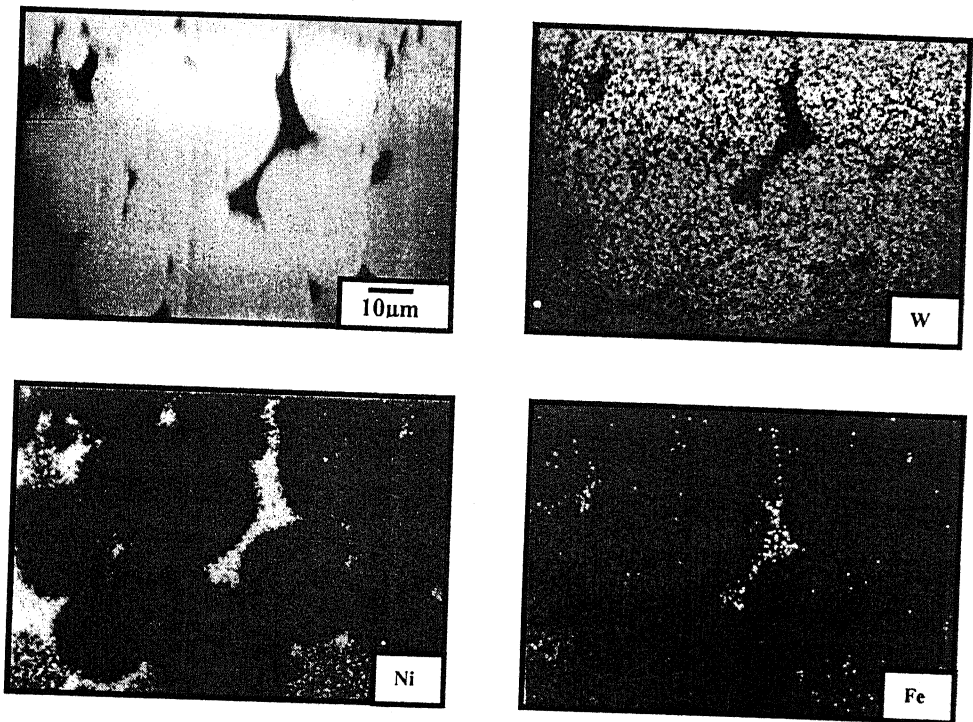


**Figure 4.36b.** Microstructure of conventionally sintered 92.5W-6.4Ni-1.1Fe alloy with and X-Ray mapping of the elements present in the matrix.

#### 4.8.6. Bulkhardness

Figure 4.37a shows the comparison of bulkhardness values (VHN) of both samples. It was observed that microwave sintered alloys has higher hardness value.

Hardness depends on the volume fraction of the harder phase and it decreases as the amount of matrix increases. Moreover the hardness decreases as the grain size increases, due to greater separation of grains. A high contiguity aids the hardness because of greater rigidity from the solid-solid contacts. It was observed that microwave sintered sample has higher hardness value, which confirms the hypothesis. The determined values of contiguity, dihedral angle, grain size and solid volume percentage also substantiate the hardness result.

#### 4.8.7. Microhardness

Figure 4.37b shows the comparison of micro-hardness values of the alloys sintered by two different heating processes. It was found that microwave sintered alloy has higher value of microhardness in the grains but lesser in the matrix phase.

Microhardness of matrix phase depends on the amount of harder phase in the matrix. It is higher for higher value of tungsten solubility in matrix. In case of microwave sintered sample, solubility of tungsten in matrix is less than that of conventionally sintered. As in conventional sintering more time is provided which causes more diffusion of tungsten in the matrix phase. So in later case, we got the higher hardness of matrix phase.

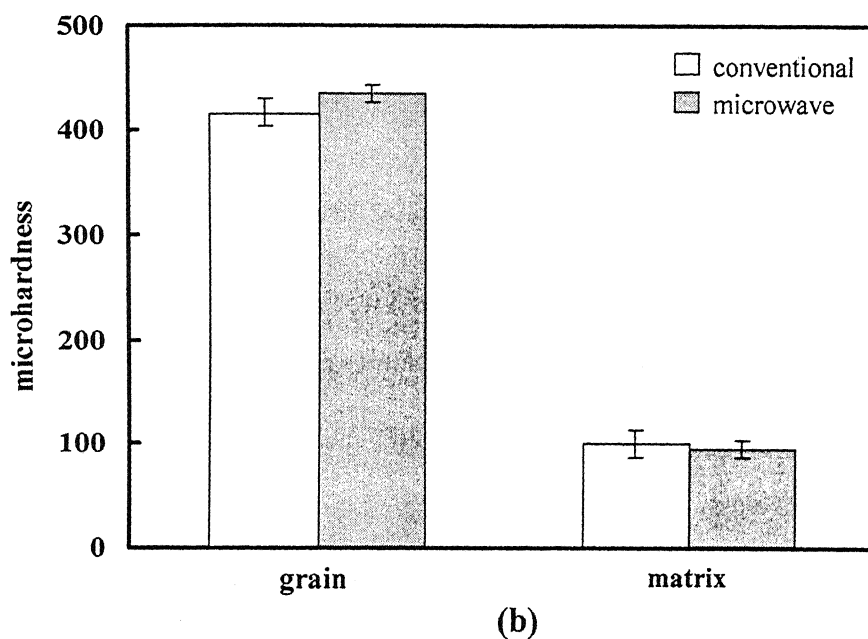
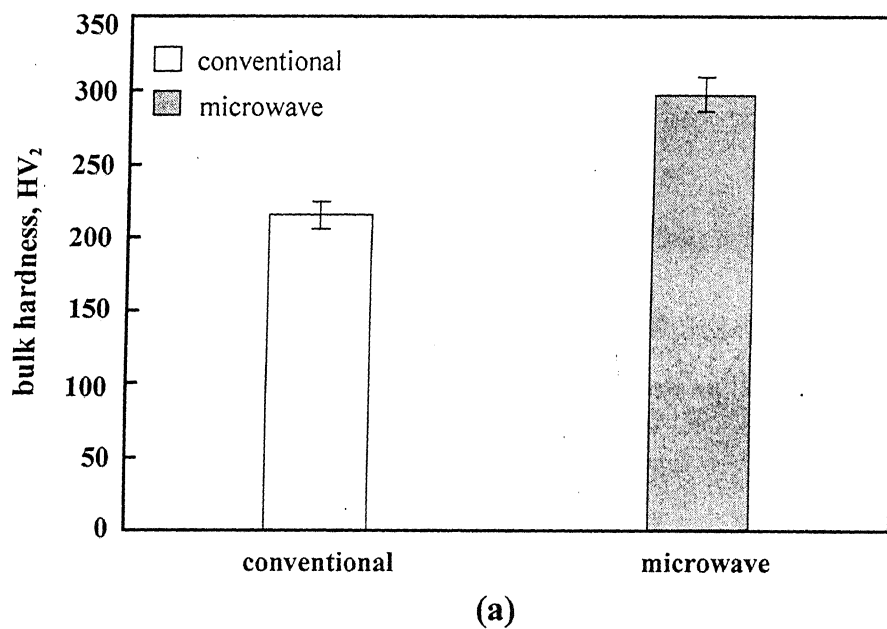


**Figure 4.37.** Hardness values of 92.5W-6.4Ni-1.1Fe alloy (a) bulk-hardness and (b) microhardness of grains as well as matrix phase.

## Chapter 5

### CONCLUSIONS

The present work was focused on the effect of milling as well as the microwave sintering on the sintering behavior and microstructural evolution of tungsten heavy alloys having compositions 90W-7Ni-3Fe and 92.5W-6.4Ni-1.1Fe. Conceiving the results and discussions of the present investigation, following conclusions are drawn:

1. Liquid phase sintering is the basic mechanism of densification of W-Ni-Fe alloys. It provides better densification than the solid state sintering.
2. Milling improves the sintering response of tungsten heavy alloy. The effects of milling can be compiled as:
  - significant reduction in initial powder size and size distribution which improves the densification response of the alloy.
  - change in powder morphology i.e. nickel and iron powders become almost flaky and welded to the tungsten powder. This improves the homogeneity of the matrix phase distribution and avoids binder pool formation.
  - milling changes all the stereological parameters towards giving positive effects on the final properties of the alloy i.e. reduces mean grain size, dihedral angle, connectivity, contiguity and increases volume fraction of matrix.
  - the mechanical properties – microhardness, bulkhardness are higher in case of milled Samples.



5. For the first time, W-Ni-Fe heavy alloys have been successfully liquid phase sintered through microwave heating. Microwave sintering results in:

- Substantial reduction ( $\sim 50\%$ ) in processing time.
- Finer grain size ( $\sim 40\%$  less than conventional).
- Improved bulkhardness ( $\sim$  increase  $> 20\%$ ).
- No intermetallic formation in microwave sintered tungsten heavy alloy although, the composition selected was non-stoichiometric.

6. The compressive test reveals that in case of liquid phase sintered samples the force is absorbed by tungsten grains only but in solid state sintered samples the matrix phase also contributes towards absorbing the deformation force.

## REFERENCES

- [1] A. Upadhyaya, "Tungsten Heavy Alloys for Ordnance and Thermal Management Applications," *Trans. Indian Inst. Met.*, Feb., 2002, vol. 55, no. 1-2, pp. 51-69.
- [2] A. Upadhaya, "Processing Strategy for Consolidating Tungsten Heavy Alloys for Ordnance Applications," *Materials Chemistry and Physics*, 2001, vol. 67, pp.102-109.
- [3] G. S. Upadhyaya, Sintered Metallic and Ceramic Materials, Johan Willey & Sons, Ltd., Baffines Lane, Chichester, England, 1999.
- [4] K. S. Churn and R. M. German, "Fracture Behavior of W-Ni-Fe Heavy Alloys," *Metallurgical Transactions A*, 1984, vol. 15, no. 2, pp. 331-338.
- [5] R. M. Anklekar, D. K. Agrawal and R. Roy, "Microwave Sintering and Mechanical Properties of P/M Copper Steel," *Powder Metall.*, v.44, n.4, 2001, pp. 355-362.
- [6] D. M. Pozar, *Microwave Engineering*, 2<sup>nd</sup> ed., John Wiley & Sons, Toronto, Canada, 2001.
- [7] C. J. Smithells, Tungsten: A Treatise on its Metallurgy, Properties, and Applications, D.Van Norstrand Company, N.Y, (1927), 1.
- [8] W. D. Coolidge, "Ductile Tungsten," *Trans Amer. Inst. Electrical Engineers*, 29 (1910), pp. 961-965.
- [9] W. D. Jones, Fundamental Principles of Powder Metallurgy, (London, Edward Arnold (Publisher), 1960), pp. 600.
- [10] C. J. Smithells, W. R. Pitkins, and J. W. Avery, "Grain Growth in Compressed Metal Powder," *J.Inst.Metal*, 38 (1927), pp. 88-102.
- [11] F. V. Lenel, Powder Metallurgy Principles and Applications, (Metal Powder Industry Federation, Princeton, NJ, 1980), pp. 337-348.
- [12] R. M. German, Liquid Phase Sintering, (Plenum Press, NY), 1985.
- [13] R. M. German, "Critical Developments in Tungsten Heavy Alloys," Metal Powder Industry Federation, Nov. 15-18, 1992, Virginia.
- [14] G. S. Upadhyaya, "Sintered Heavy Alloys-A Review," *International Journal of Refractory & Hard Metals*, March 1986, vol. 5, no. 2.

- [15] I. Massalski, "Binary Alloy Phase Diagrams," ASM International, Materials Park, Ohio, USA, 1990.
- [16] G. V. Raynor and V.G. Rivlin, "Phase Equilibria in Iron Ternary Alloys," Institute of Metals, London, no. 4, 1988.
- [17] S. G. Caldwell, "Tungsten Heavy Alloys," ASM Hand Book, P.W. Lee and R. Lacocca (eds.), *Powder Metal Technologies and Applications*, Materials Park, Ohio, USA, 1998, v. 7, pp. 914-921.
- [18] S. G. Caldwell, "Variation of Ni to Fe Ratio in W-Ni-Fe Alloys: A current Perspective," Tungsten and Tungsten Alloys -1992, A. Bose and R.J. Dowding (eds.), Metal Powder Industries Federation, NJ, USA, 1992, pp. 89-96.
- [19] R. M. German, Sintering Theory and Practice, John Wiley & Sons, Inc., New York, 1996.
- [20] W.A. Kaysser and G. Petzow, "Present state of Liquid Phase Sintering," *Powder Metall.*, 1985, vol. 28, pp. 145-150.
- [21] R. M. German, Powder Metallurgy Science, 2<sup>nd</sup> edition, Metal Powder Industries Federation, Princeton, NJ, USA, 1994.
- [22] W.D. Kingery and M.D. Narashimhan, "Densification During Sintering in the Presence of a Liquid Phase. 2. Experimental," *Journal of Applied Physics*, 1959, v. 30, pp. 307-310.
- [23] H.S. Canon and F.V. Lenel, "Some Observations on the Mechanism of Liquid Phase Sintering," Plansee Proceedings, F. Benesovsky (ed.) Plansee Metalwerk, Reutte, Austria, 1953, pp. 106-122.
- [24] R. M. German, P. Lu and B. M. Marx "Liquid Phase Sintering of Tungsten Heavy Alloys," *The International Journal of Powder Metallurgy*, 2001, vol. 37, no. 6, pp. 45-56.
- [25] D. N. Yoon and W. J. Huppmann, "Grain Growth and Densification During Liquid Phase Sintering of W-Ni," *Acta Metallurgica*, 1979, vol. 27, pp. 693-698.
- [26] V. Smolej, S. Pejounik, and W.A. Kaysser, "Rearrangement During Liquid Phase Sintering of Large Particles," *Powder Metallurgy International*, 1981, v. 14, pp. 126-128.
- [27] D. N. Yoon and W. J. Huppmann, "Chemically Driven Growth of Tungsten Grains During Sintering in Liquid Nickel," *Acta Metallurgica*, 1979, vol. 27, pp. 973-977.

- [28] R. M. German, P. Lu and B. M. Marx "Liquid Phase Sintering of Tungsten Heavy Alloys," *The International Journal of Powder Metallurgy*, 2001, vol. 37, no. 6, pp.45-56.
- [29] G. S. Upadhyaya and V. Srikanth, "Effect of Tungsten Particle Size and Binder Composition on Sintered Properties of Heavy Alloys," *Modern Developments in Powder Metallurgy*, 1985, vol.15-17, pp. 51-75.
- [30] A. Belhadjhamida and R. M. German, "Tungsten and Tungsten Alloys by Powder Metallurgy – A Status Review," *The Minerals: Metals and Materials Society*, 1991, pp. 3-17.
- [31] S. Eroglu and T. Baykara, "Effect of Powder Mixing Technique and Tungsten Powder Size on the Properties of Tungsten Heavy Alloys," *Journal of Materials Processing Technology*, 2000, vol. 103, pp.288-292.
- [32] A. Asthana and G. S. Upadhyaya, "Effect of Different Ball Millings on Size Distribution of Tungsten Powder," *International Journal of Refractory and Hard Metals*, Sep. 1985, vol. 4, no. 3.
- [33] C. Suryanarayana, M. L. Ovecoglu and B. Ozkal, "A Comparison of Sintering Characteristics of Ball and Attritor Milled W-Ni-Fe Heavy Alloys," *Journal of Mat. Res.*, Jul 1996, vol. 11, no. 7, pp. 1673-1682.
- [34] H. J. Ryu, S. H. Hong and W. H. Baek, "Microstructure and Mechanical Properties of Mechanically Alloyed and Solid-state Sintered Tungsten Heavy Alloys," *Materials Science and Engineering A*, 2000, vol.291, pp. 91-96.
- [35] S.G. Caldwell, "Tungsten Heavy Alloys," ASM Hand Book, v. 7, P.W. Lee and R. Lacocca (eds.), Materials Park, OH, USA, 1998, pp. 914-921.
- [36] F.V. Lenel, Powder Metallurgy Principles and Applications, Metal Powder Industries Federation, Princeton, NJ, USA, 1980.
- [37] Yu V Bykov, K I rybakov and V E Semenov, "High-Temperature Microwave Processing of Materials," *Journal of Physics D: Applied Physics*, 34 (2001), pp. R55-R75.
- [38] A. R. Von Hippel, "Dielectric Materials and Applications," John Wiley, New York, 1954.
- [39] R. Roy, D. Agrawal, J. P. Cheng, and M. Mathis, "Microwave Processing: Triumph of Applications - Driven Science in WC-Composites and Ferroic Titanates," in Microwave: Theory and Application in Materials Processing IV, Eds. D.E. Clark, W.H. Sutton and D.A. Lewis, Ceramic Trans. Vol. 80, ACS Publ. (1997), pp 3-26.

- [40] D. E. Clark, W. H. Sutton, "Microwave Processing of Materials," *Ann. Rev. mater. Sci.*, vol. 26, 1996, pp. 299-331.
- [41] V. K. Varadan "Microwave Processing of Materials," *NMAB-473, National Academy Press*, Washington, D.C.1994.
- [42] R. E. Newnham, S. J. Jang, Ming Xu, and Frederick Jones, "Fundamental Interaction Mechanisms between Microwaves and Matter," *Material Research Laboratory, The Pennsylvania State University*, pp. 51-67.
- [43] Clark Gellings, "Dielectric Heating: EPRI's Perspective on the Market and Technology," *Microwaves: Theory and application in Material Processing IV*, Cera. Trans., vol. 80, pp. 27-41.
- [44] M. A. Janney and H. D. Kimrey, "Microwave Processing of Materials II," *Materials Research Society Symp. Proc.*, vol. 189, pp. 215-227.
- [45] Yu V Bykov, Microwave Processing of Materials II," *Materials Research Society Symp. Proc.*, vol. 189, pp. 41-42
- [46] D. Agrawal, "Microwave Sintering of Ceramics, Composites, Metals, and Transparent Materials: Recent developments at MRL/PSU," *7<sup>th</sup> International Conf. On Microwave and High Frequency Heating*, 1999, pp. 263-267.
- [47] T. Gerdes, M. Willert-Porada and K. Rodiger, "Microwave Sintering of Tungsten-Cobalt hard metals," *Mater. Res. Soc. Symp. Proc.*, v.430, 1996, pp. 45-50.
- [48] A Birman *et al.*, "Microwaves: Theory and Applications in Materials Processing III, Cera. Trans., vol. 59, OH, pp. 175-180.
- [49] T Saji, Microwave Processing of Materials V, *Materials Research Society Symp. Proc.*, vol. 430, pp. 15-20.
- [50] B H Rabin and I Shiota, 1995MRS Bull, pp. 14-15.
- [51] E. T. Thostenson, T. W. Chou, "Microwave Processing: Fundamentals and Applications," *Composites: Part A* 30 (1999), pp. 1055-1071.
- [52] Yuri Korniyushin, "Influence of External Fields on Sintering," *Advanced Science and Technology of Sintering*, N.Y., 1999, pp. 3-18.
- [53] H. Park, W. Baik, S. L. Kang and D. Yoon, "The Effect of Molybdenum addition on the liquid phase sintering of W Heavy Alloys," *Metallurgical and Materials Transactions A*, Oct. 1996, vol. 27A, no. 10, pp. 3120-3125.

- [54] H. S. Song, J. W. Noh, W. H. Baek, S. Joong, L. Kang, and B. S. Chun, "Undulation of W/Matrix Interface by Resintering of Cyclically Heat Treated W-Ni-Fe Heavy Alloys," *Metallurgical and Materials Transactions A*, Feb. 1997, vol. 28, no. 2, pp. 485-489.
- [55] A. Bose and R. M. German, "Microstructural Refinement of W-Ni-Fe Heavy Alloys by Alloying Additions," *Metallurgical Transactions A*, Dec. 1988, vol. 19, no. 12, pp. 3103.
- [56] T. Antonsson and L. Ekbom, "Initial Stage of Liquid Phase Sintering: Liquid Reaction and Particle Growth in W-Ni-Fe- (Co)," *Powder Metallurgy*, 2001, vol. 44, no. 4, pp. 325-332.
- [57] S. H. Hong, S. L. Kang, D. N. Yoon, and W. H. Baek, "The Reduction of the Interfacial Segregation of Phosphorus and Its Embrittlement Effect by Lanthanum Addition in a W-Ni-Fe Heavy Alloy," *Metallurgical and Materials Transactions A*, Dec. 1991, vol. 22, no.12, pp. 2969-2974.
- [58] H. K. Yoon, S. H. Lee, and D. N. Yoon, "Effect of Vacuum Treatment on Mechanical Properties of W-Ni-Fe Heavy Alloy," *Journal of Materials Science*, 1983, vol. 18, no. 4, pp. 1374-1380.
- [59] T. Kohno and O. Mayama, "Effect of Sintering and Post-Sintering Heat Treatment on the Mechanical Properties of the W-Ni-Fe Heavy Alloys," International Conference on Powder Metallurgy, The Institute of Metals, London, U.K., 2-6 July 1990, vol. 1, pp. 324-331.
- [60] J. W. Noh, M. H. Hong, G. Kim, S. L. Kang, and D. Y. Yoon, "The Cause of Matrix Penetration of W/W Grain Boundaries During Heat Treatment of W-Ni-Fe Heavy Alloys," *Metallurgical and Materials Transactions A*, Dec. 1994 vol.25, no. 12, pp. 2828-2831.
- [61] H. S. Song, J. W. Noh, W. H. Baek and K. S. Churn, "Ageing Treatment on the Heavy Alloy," International Conference on Powder Metallurgy, The Institute of Metals, London, U.K., 2-6 July 1990, vol. 3, pp. 231-234.
- [62] M. H. Hong, S. Lee, J. W. Noh and Y. W. Kim, "The Effect of Thermo-Mechanical Treatment on the Microstructure and Failure Behavior of Sintered W heavy Alloys," International Conference and Exhibition on Powder Metallurgy and Particulate Materials, Metal Powder Industries Federation and APMI International, Toronto, Canada, May 8-11, 1994, vol. 5, pp.279-288
- [63] "MPIF Standard 03: Determination of Flow Rate of Free-Flowing Metal Powders using the Hall Apparatus," Standard Test Methods for Metal Powders and Powder Metallurgy Products, Metal Powder Industry Federation, Princeton, NJ, 1991.

- [64] J. S. Lee, W. A. Kaysser, and G. Petzow, "Microstructural changes in W-Cu and W-Ni-Cu compacts during Hetaing up for Liquid Phase Sintering," *Modern Developments in Powder Metallurgy*, E.n. Aqua and C.I. Whitman (eds.) MPIF-APMI, Princeton, NJ, 1984, vol. 15, pp. 489-506.
- [65] E. Ernst, F. Thummler, P. Beiss, R. Wahling and V. Arnhold, "Friction Measurements during Powder Compaction," *Powder Metallurgy International*, 1991, vol. 23, no. 2, pp. 77-84.
- [66] D. K. Patrick. "A Guide to metallographic Preparation of Materials- Part I," *Industrial Heating*, 1997, vol. 64, pp. 37-43.
- [67] R. T. Howard and M. Cohen, "Quantitative Metallography by Point Counting and Lineal Analysis," *Transactions AIME*, 1947, vol. 172, pp. 413-426.
- [68] J. Gurland, "The Measurement of Grain Contiguity in Two Phase Alloys," *Transactions TMS-AIME*, 1958, vol. 212, pp. 452-455.
- [69] J. Gurland, "An Estimate of Contact and Continuity of Dispersions in Opaque samples," *Transactions TMS-AIME*, 1966, vol. 236, pp. 642-646.
- [70] R. T. DeHoff, "Estimation of Dihedral Angle from Stereological Counting Methods," *Metallography*, 1986, vol. 19, pp. 209-217.
- [71] G. F. Vander Voort, "Grain Size Measurement," *Practical Applications of Quantitative Metallography*, ASTM, Philadelphia, PA, 1984, pp. 85-130.
- [72] B. D. Cullity, S.R. Stock, Stuart Stock, "Elements of X-Ray Diffraction," 3<sup>rd</sup> edition, Addison-Wesley Series, 1956.
- [73] Zhong-Wu Zhang, Guang Ran, Sheng-Qi Xi, and Wen-Xing Zhang, "Formation of Crystalline and Amorphous Solid Solutions of W-Ni-Fe Powder during Mechanical Alloying," *Journal of Alloys and Compounds*, vol. 370 (2004), pp. 186-191.
- [74] J. Liu, A. L. Cardamone and R. M. German, "Estimation of Capillary Pressure in Liquid Phase Sintering," *Powder Metallurgy*, 2001, vol. 44, no. 4, pp. 317-324.
- [75] W. Schatt and E. Friedrich, "Dislocation Activated Sintering Processes," *Powder Metall.*, vol. 128, no. 3, 1985, pp. 140-144.
- [76] G. S. Upadhyaya, "Electronic Mechanism of Sintering: Some Case Studies on Real System," *Bulletin of Material Science*, 1994, vol.17, no. 6, pp. 921-934
- [77] David E. Clark, "Microwave Processing of Materials ," *Annu. Rev. mater Sci.* 1996. 26, pp. 21-31.

- [78] S. A. Freeman, J. H. Booske, R.F. Cooper, "Microwaves: Theory and application in material processing III," *Ceram. Trans. Weastville*, 1995, pp. 2042-45.
- [79] H. Fredriksson, A. Eliasson, I. Ekbom, "Penetration of Tungsten Grain Boundaries by Liquid W-Ni-Fe Matrix," *International Journal of Refractory Metals & Hard Materials*, No.4, 1995, pp. 173-179.
- [80] A. Upadhyaya, "A microstructure-based model for shape distortion during liquid phase sintering," A thesis in Engineering Science and Mechanics, The Pennsylvania State University, May 1998.
- [81] K. M. Ramkrishnan and G.S. Upadhyaya, "Effect of Composition and Sintering on Densification and Microstructure of Tungsten Heavy Alloys Containing Copper and Nickel," *Journal of Mater. Sci. Letter*, 1990, v.9, pp. 456-459.



## Appendix I

Cylindrical compacts prepared by mixed powders, solid state sintered at 1400°C, 1h  
H<sub>2</sub> (compaction pressure-200MPa)

Parameters measured		Compositions	
		90W-7Ni-3Fe (fine)	90W-7Ni-3Fe (coars
Weight, g	Green	10.1329	10.0635
	Sintered	10.0132	10.0274
Height, mm	Green	7.68	7.16
	Sintered	6.72	6.84
Diameter, mm	Green	12.75	12.75
	Sintered	11.83	11.06
Density, g/cm <sup>3</sup>	Green	10.51	10.82
	Sintered	15.3589	15.1867
% Theoretical density	Green	59.00	60.27
	Sintered	84	82.6
Weight loss, %		0.30	0.28
Densification parameter		0.71	0.68

**Cylindrical compacts prepared by ball milled powders, sintered at 1400°C, 1h, H<sub>2</sub>  
(compaction pressure-200MPa)**

Parameters measured		Compositions	
		90W-7Ni-3Fe (fine)	90W-7Ni-3Fe (coarse)
Weight, g	Green	10.0245	10.135
	Sintered	9.8970	10.0134
Height, mm	Green	7.23	7.16
	Sintered	6.67	6.74
Diameter, mm	Green	12.75	12.75
	Sintered	11.48	11.76
Density, g/cm <sup>3</sup>	Green	10.1	10.52
	Sintered	15.2289	15.2067
% Theoretical density	Green	58.20	58.97
	Sintered	84.9	83.1
Weight loss, %		0.24	0.32
Densification parameter		0.73	0.69

Cylindrical compacts prepared by attritor milled powders, sintered at 1400°C, 1h, H<sub>2</sub>.  
(compaction pressure-200MPa)

Parameters measured		Compositions	
		90W-7Ni-3Fe (fine)	90W-7Ni-3Fe (coarse)
Weight, g	Green	10.3210	10.1358
	Sintered	10.1789	10.0130
Height, mm	Green	7.20	7.16
	Sintered	6.67	6.73
Diameter, mm	Green	12.75	12.75
	Sintered	11.08	11.46
Density, g/cm <sup>3</sup>	Green	10.1	10.52
	Sintered	15.5499	15.2471
% Theoretical density	Green	58.20	58.97
	Sintered	86	83.4
Weight loss, %		0.24	0.32
Densification parameter		0.75	0.7

## Appendix II

**Cylindrical compacts prepared by mixed powders, sintered at 1500°C, 1h, H<sub>2</sub>  
(compaction pressure-200MPa)**

Parameters measured		Compositions	
		90W-7Ni-3Fe (fine)	90W-7Ni-3Fe (coarse)
Weight, g	Green	10.1169	10.1029
	Sintered	10.0930	9.9581
Height, mm	Green	7.84	7.52
	Sintered	6.90	6.81
Diameter, mm	Green	12.75	12.75
	Sintered	10.88	10.94
Density, g/cm <sup>3</sup>	Green	10.4558	11.0661
	Sintered	16.8863	16.5186
% Theoretical density	Green	60.1	62.5
	Sintered	92.83	90.79
Weight loss, %		0.29	0.28
Densification parameter		0.81	0.79

**Cylindrical compacts prepared by ball milled powders, sintered at 1500°C, 1h, H<sub>2</sub>  
(compaction pressure-200MPa)**

Parameters measured		Compositions	
		90W-7Ni-3Fe (fine)	90W-7Ni-3Fe (coarse)
Weight, g	Green	10.1019	10.1218
	Sintered	10.0789	10.1020
Height, mm	Green	7.19	7.16
	Sintered	6.57	6.79
Diameter, mm	Green	12.75	12.75
	Sintered	11.04	11.31
Density, g/cm <sup>3</sup>	Green	9.94	10.32
	Sintered	16.9487	16.8471
% Theoretical density	Green	58.97	59.14
	Sintered	94.1	92
Weight loss, %		0.36	0.32
Densification parameter		0.88	0.85

Cylindrical compacts prepared by attritor milled powders, sintered at 1500°C, 1h, H<sub>2</sub>,  
(compaction pressure-200MPa)

Parameters measured		Compositions	
		90W-7Ni-3Fe (fine)	90W-7Ni-3Fe (coarse)
Weight, g	Green	10.1623	10.1076
	Sintered	10.0671	10.0972
Height, mm	Green	7.26	7.3
	Sintered	6.51	6.65
Diameter, mm	Green	12.75	12.75
	Sintered	10.94	11.01
Density, g/cm <sup>3</sup>	Green	9.94	10.32
	Sintered	17.3210	17.1243
% Theoretical density	Green	57.92	58.12
	Sintered	97.1	95
Weight loss, %		0.3	0.32
Densification parameter		0.92	0.91

Samples prepared by mixed powders, sintered at 1500°C, 1h, H<sub>2</sub>, through microwave as well as conventional furnace heating. (compaction pressure-200MPa)

Parameters measured		92.5W-6.4Ni-1.1Fe	
		microwave heating	conventional heating
Weight, g	Green	10.1254	10.1065
	Sintered	10.0539	10.0152
Height, mm	Green	7.13	7.27
	Sintered	6.21	6.35
Diameter, mm	Green	12.75	12.75
	Sintered	10.96	11.01
Density, g/cm <sup>3</sup>	Green	10.27	10.32
	Sintered	17.1216	17.2243
% Theoretical density	Green	57.97	58.16
	Sintered	97.1	97.8
Weight loss, %		0.29	0.31
Densification parameter		0.93	0.94